University of Alberta

Integrated Nanoplasmonic Waveguides and Devices for All-Optical Nanocircuitry

by

Michael Patrick Nielsen

A thesis submitted to the Faculty of Graduate Studies and Research
in partial fulfillment of the requirements for the degree of

Master of Science

in

Photonics and Plasmas

Department of Electrical and Computer Engineering

Fall 2013
Edmonton, Alberta

To my family and friends for their love and support.

Abstract

This thesis focuses on the development of integrated silicon-based nanoplasmonic waveguides and devices for use in all-optical plasmonic circuitry. To this end, metal-insulator-semiconductor-insulator-metal (MISIM) and metal-insulator-semiconductor (MIS) hybrid nanoplasmonic waveguides were designed, fabricated and characterized along with resonant devices developed on the same platform such as waveguide ring resonators, disk resonators and Bragg reflector resonators. These hybrid nanoplasmonic waveguides and devices were integrated with conventional silicon photonic waveguides and incorporated on the complimentary metal-oxide-semiconductor (CMOS) silicon-on-insulator (SOI) platform. Next, the possibility of overcoming losses in plasmonic circuitry is investigated through an integrated electrically-pumped InGaAs nanoplasmonic amplifier. The possibility of all-optical modulation is studied through resonant switching in a silicon-based nanoplasmonic ring resonator using two-photon absorption (TPA) generated free carriers as the nonlinear switching mechanism. The final study is on incorporating 3-D routing capabilities into plasmonic nanocircuitry through vertically coupled plasmonic ring resonators.

Acknowledgements

This thesis work would not have been possible without the support of a great many people. First and foremost, my heartfelt thanks to my supervisor Prof. Abdulhakem Y. Elezzabi for his guidance, advice and, most of all, his patience with me. When I needed it most, he was always there to coax me to the next idea when the work looked its bleakest. His boundless passion for science and endless encouragement help mold me into the researcher I am today.

To my colleagues at the Ultrafast Optics and Nanophotonics Laboratory, Shawn Sederberg, Nir Katchinskiy, Shawn Greig and Brett Carnio, I am grateful for your camaraderie. I would especially like to thank Shawn Sederberg for his mentorship and advice throughout this start to my career. Without his help, I am not sure any of my fabrication processes would have worked out.

I give thanks to all the others who helped with the fabrication process. I thank Prof. Ken Cadien and Amir Ashfar for helping me with atomic layer deposition and Sam Maloney for the atomic force microscopy measurements. Further thanks to the support staff at the University of Alberta Nanofab, especially Les Schowalter, Scott Munro and Stephanie Bozic for training me on the equipment.

Finally, I need to thank my family and friends for their continued support throughout my studies.

Table of Contents

List of Tables

List of Figures

List of Symbols and Abbreviations

Fundamental Constants

$\varepsilon_o = 8.854187817 \times 10^{-12}$ F/m	electric permittivity of vacuum
$c = 2.99792458 \times 10^{8}$ m/s	speed of light in vacuum
$h = 6.62606957 \times 10^{34}$ J·s	Planck's constant
$\hbar = 1.054571726 \times 10^{34}$ J·s	reduced Planck's constant
$q = 1.60217657 \times 10^{-19}$ C	elementary electron charge

Symbols

$\boldsymbol{E}$	electric field
$\boldsymbol{H}$	magnetic field
$\boldsymbol{D}$	electric displacement field
$\hat{n}$	normal unit vector
∇	del operator
ε	electric permittivity
α	spatial decay rate
ω	angular frequency
x	propagation spatial component
y	lateral spatial component
z	vertical spatial component
θ_x	roll angle

θ_y	pitch angle
θ_z	yaw angle
k_{SPP}	surface plasmon polariton wavevector
L_p	propagation length
T	coupling efficiency
$\tilde{n}$	complex refractive index
n	real part of the refractive index
A	area
λ	wavelength
L	length
W	width
H	height
R	rate
τ	lifetime
i	index
Δ	bandwidth
g	energy level degeneracy
P	polarization
N	carrier concentration
t	time
g_m	gain constant
m	mass
f	probability

E	energy level
k	momentum
μ	mobility
V	voltage
T	temperature
S	overlap integral
C_{aug}	Auger coefficient
I	intensity
β_{TPA}	TPA coefficient
χ	susceptibility
$\pm_{FCA}$	free-carrier absorption cross-section

Abbreviations

2-D	two dimensional
3-D	three dimensional
ALD	atomic layer deposition
a.u.	arbitrary units
CMOS	complementary metal-oxide-semiconductor
CMP	chemical mechanical polishing
CPP	channel plasmon polariton
CW	continuous wave
DLSPP	dielectric-loaded surface plasmon polariton
DMAC	dimethylacetamide

EBL	electron beam lithography
EM	electromagnetic
EPIC	electronic-photonic integrated circuits
FCA	free carrier absorption
FDTD	finite difference time domain
FM	figure of merit
FWHM	full width at half maximum
GSPP	gap surface plasmon polariton
HPP	hybrid plasmonic-photonic
ICPRIE	inductively coupled plasma reactive ion etching
IM	insulator-metal
IMI	insulator-metal-insulator
I/O	input/output
IPA	isopropyl alcohol
LER	line edge roughness
LRSPP	long range surface plasmon polariton
MIBK	methyl isobutyl ketone
MIM	metal-insulator-metal
MIS	metal-insulator-semiconductor
MISIM	metal-insulator-semiconductor-insulator-metal
NA	numerical aperture
NSOM	near field scanning optical microscopy
PECVD	plasma enhanced chemical vapour deposition

PDE	plasma dispersion effect
PMMA	poly(methyl methacrylate)
Q	quality
R6G	Rhodamine 6G
RIE	reactive ion etching
RPM	revolutions per minute
SEM	scanning electron microscopy
SOA	semiconductor optical amplifier
SOI	silicon-on-insulator
SPASER	surface plasmon amplification by stimulated emission of radiation
SPP	surface plasmon polariton
TDMAH	tetrakis(dimethylamino)hafnium
TE	transverse electric
TEM	transverse electromagnetic
TM	transverse magnetic
TPA	two-photon absorption
UONL	Ultrafast Optics and Nanophotonics Laboratory
WD	working distance
WDM	wavelength-division multiplexing

Chapter 1

Introduction

1.1 Motivation

With today's modern transistors and other electronic components shrinking down to the tens of nanometers scale, the current generation of computation platforms is facing fundamental speed limitations. With the advent of large high speed broadband fiber optics networks for data transfer, information processing has begun to move towards photonic components. However, even with fiber optics networks, the optical signal must still be converted to an electrical signal at the chip level. Silicon photonics, taking advantage of monolithic integration with the standard and well developed complementary metal-oxide semiconductor (CMOS) technology, was originally thought to be the answer. However, while silicon photonics circuits show promise in overcoming the fundamental speed limits of conventional electronic circuits, they are ultimately limited in size by the light diffraction limit in the telecommunications band (1.3-1.6 μm) to device sizes far in excess of those found in conventional electronics. The light diffraction limit constrains the minimum dimension of a photonic device to half of the wavelength

of its operating frequency, sizes far in excess at telecommunication wavelengths of the nanoscale dimensions in electronic components

In recent years, there has been a growing interest in the emerging field of nanoplasmonics. Through exploration of surface waves at metal-dielectric interfaces, the optical signal in metal-dielectric plasmonic devices can be confined to mode sizes far below the light diffraction limit [1]. This makes plasmonics more capable of competing with conventional electronics in terms of device size, while still retaining the speed advantages of typical silicon photonic devices. The nanoscale optical mode confinement and subwavelength bending radii of nanoplasmonic waveguides give rise to high integration densities and more efficient access to higher order nonlinearities. This has led to their proposal as a lead contender for providing the basis for the next generation of chip-scale computing platforms offering ultrafast operation capabilities [2]. In addition, the integration of nanoplasmonics devices with a silicon based platform system allows for monolithic integration with standard CMOS technology, giving rise to the possibility of hybrid electronic/plasmonic nanocircuitry [3].

1.2 Theory of Surface Plasmons

Surface plasmon polaritons (SPPs) are surface electromagnetic (EM) excitations that occur when an evanescent EM wave is coupled to surface collective oscillations of free electrons at a metal-dielectric interface [4]. The SPPs are bound to and propagate along the interface. In 2-D geometries, the wave

equations derived from Maxwell's equations decouple into transverse magnetic (TM) and transverse electric (TE) modes, in which the electric field *E* is polarized in (*p*-polarized) and perpendicular to (*s*-polarized) the plane of propagation, respectively. The first boundary condition for a surface wave was at an interface requires that the field vanish infinitely far from the interface, requiring an exponential decay away from the interface. Maxwell's equations also require the components of the EM fields parallel to the interface, the tangential components, to be continuous. For TE modes, this means both the electric field, and for nonmagnetic media where the magnetic susceptibility $¡_m = 0$, its derivative normal to the interface $\nabla\vec{E} \bullet \hat{n}$ must be continuous across the interface. The result of these boundary conditions is that SPP modes cannot be *s*-polarized. It is important to note that in 3-D geometries while *s*-polarized SPPs cannot exist in nonmagnetic media, *p*-polarized TE-SPP modes can exist. For TM modes, both the magnetic field and the product $(1/£)\cdot\nabla\vec{E} \bullet \hat{n}$ must be continuous across the interface. These boundary conditions give rise to confined solutions for TM modes only for a change in the in the sign of the dielectric constant across the interface. Thus, the interface must be formed between material with a negative dielectric permittivity and one with a positive dielectric permittivity, normally a metal below its plasma frequency and a dielectric [4]. It should be noted that the interface between a dielectric and a negative refractive index material, one with both negative dielectric permittivity and negative magnetic permeability, would be capable of supporting both 2-D TE- and TM-SPP modes. For a metal-dielectric

interface, the result from Maxwell's equations that lead to the allowed TM-SPP modes is [4]:

$$\frac{\tilde{}_m}{£_m} + \frac{\tilde{}_d}{£_d} = 0, \tag{1.1}$$

where $\tilde{}_m$ is the exponential decay factor away from the interface in the metal, $\tilde{}_d$ is the exponential decay factor away from the interface in the dielectric, $£_m$ is the electric permittivity of the metal, and $£_d$ is the electric permittivity of the dielectric. Eq. 1.1 is satisfied only for a change in the sign of the dielectric permittivity between the materials. An illustrated of the SPP mode supported by a single metal-dielectric interface is depicted in Figure 1.1 From this it is possible to derive the SPP dispersion relation [4] for the complex wavevector of the SPP mode:

$$k_{SPP}(\mu) = \frac{\mu}{c}\sqrt{\frac{£_m(\mu)\cdot£_d(\mu)}{£_m(\mu)+£_d(\mu)}}. \tag{1.2}$$

The real part of the wavevector is required for phase matching with external media, either to excite the SPP mode or to couple the SPP mode out. The imaginary part of the wavevector is related to the propagation length of the mode, $L_p = 1/\mathrm{Im}(2k_{SPP})$. The propagation length is the distance the mode can travel before attenuating to 1/e of its initial power.

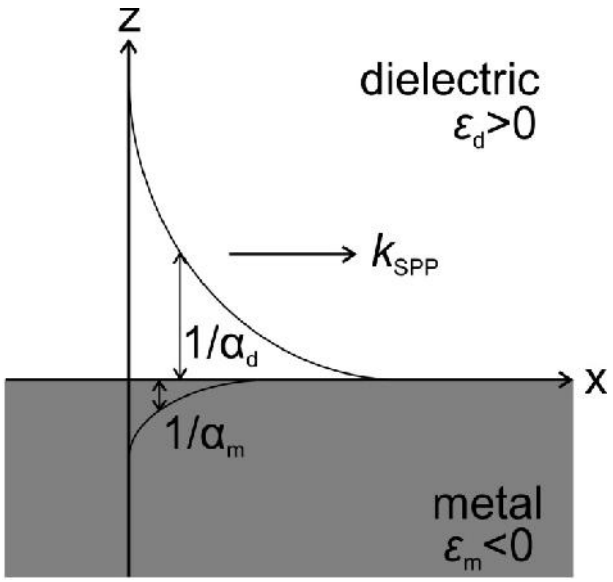

Figure 1.1: SPP mode supported by a metal-dielectric interface showing exponential decay away from the interface.

1.3 Traditional Plasmonic Waveguiding Configurations

Waveguides are the most fundamental and basic component of integrated photonic circuits. Not only do they support and guide optical signals, but many of the more advanced devices are formed or based on waveguides, such as waveguide ring resonators which are merely a waveguide closed into a circle, directional couplers, splitters, filters, Bragg gratings, disk resonators, modulators, amplifiers, and interferometers The addition of the metal layers in photonic waveguides has opened up the possibility to numerous different waveguiding configurations. The last decade has witnessed many innovative nanoplasmonic waveguiding configurations being proposed and explored in an effort to take

advantage of their unique properties. In all of the plasmonic waveguiding configurations there is an inherent trade-off between the propagation length of the waveguide mode and the confinement of the mode. As the mode size decreases, the propagation losses of the supported mode become increasingly large. What follows is a brief description of several plasmonic waveguiding configurations with a focus on the confinement and propagation length of the configuration at 1.55 μm unless otherwise noted. The applicability of a particular configuration for integration with standard CMOS compatible silicon-on-insulator (SOI) based photonic circuitry is also discussed.

1.3.1 Insulator-Metal Plasmonic Waveguides

The most basic plasmonic waveguide configuration is the insulator-metal (IM) or slab SPP waveguide consisting of a finite width metal layer on top of a dielectric slab. The mode is confined to the metal-dielectric interface, with the electric field decaying swiftly into the metal (at most tens of nanometers) and slower into the dielectric. The rate of decay of the electric field into a material is determined by the dielectric permittivity. The lateral extent of the plasmonic waveguide is determined by the width of the metal slab and can be further reduced by limiting the width of the underlying dielectric layer to facilitate waveguiding. The relatively simple fabrication required for these structures enables integration on a standard CMOS platform.

A notable demonstrated example of this configuration is [5] wherein a 300 nm wide and 340 nm tall SOI ridge waveguide was capped by a 50 nm gold slab. The

excellent nanoscale confinement of this structure, depicted in Figure 1.2, limits both the experimentally demonstrated and theoretically predicted propagation of the mode to 2 µm at 1.55 µm. Despite the high losses experienced by this mode, the demonstrated high coupling efficiency of 38% to conventional silicon photonic waveguides, low bending loss of 14.6%, and broadband operation show its capacity for integration in high density optical circuitry.

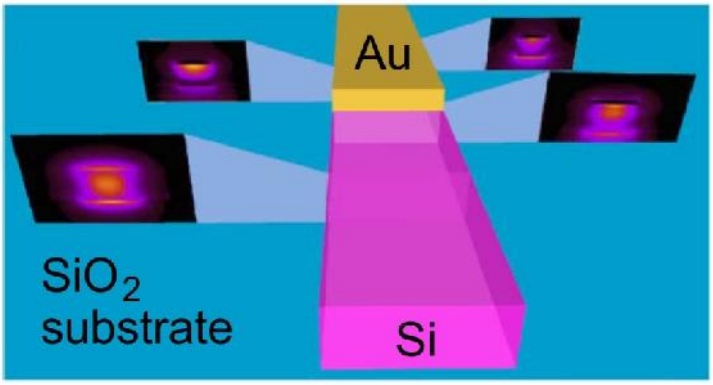

Figure 1.2: Evolution of the TM mode from a coupling photonic waveguide via a taper to an IM or slab nanoplasmonic waveguide from [5] calculated with numerical simulations. The plasmonic waveguide is formed of a 340 nm tall and 300 nm wide SOI ridge waveguide capped by a 50 nm thick Au layer.

1.3.2 Dielectric Loaded Plasmonic Waveguides

A variation of the IM configuration is the dielectric loaded plasmonic waveguide, wherein a dielectric slab is deposited on a metal surface. The ease of fabrication of this configuration comes at the expense of the available choice of dielectrics. The high processing temperature and the polycrystalline nature of silicon deposited by chemical vapour deposition limits its practicality for this

waveguide configuration for applications requiring CMOS compatibility. Commonly, dielectric loaded surface plasmon polariton (DLSPP) waveguides use the standard electron beam lithography (EBL) resist poly(methyl methacrylate), known as PMMA, as the dielectric material. The low refractive index of PMMA limits the scalability of DLSPP waveguides to sizes much larger than conventional Si photonic waveguides. However, using PMMA gives the DLSPP waveguides a correspondingly enhanced propagation length compared to IM plasmonic waveguides. For a 600 nm wide and 600 nm thick PMMA slab on gold, a propagation length of 43 µm was demonstrated in [6] at 1.55 µm which is in close agreement with the theoretical predictions. Figure 1.3 depicts a typical schematic of a DLSPP waveguide along with its mode and the effect of the dielectric slab width on propagation length.

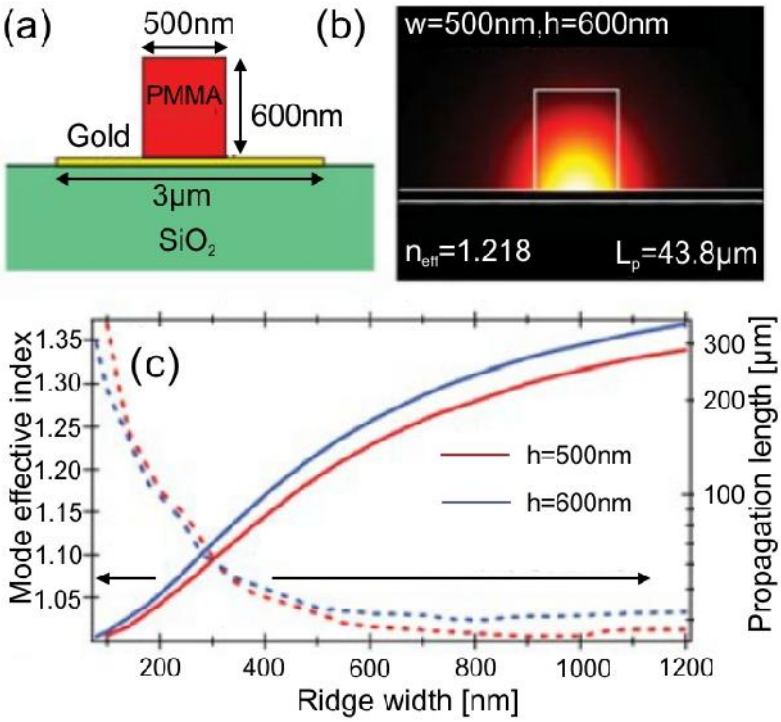

Figure 1.3: (a) Schematic cross section of a dielectric loaded plasmonic waveguide. (b) Electric field intensity mode distribution at 1.55 μm. (c) Calculated effect of PMMA ridge width on mode effective index and propagation length for ridge heights of 500 nm and 600 nm. Images from [7].

Despite the relatively large modal area of the DLSPP waveguides, their long propagation length has led to their use in the design of numerous integrated devices such as waveguide ring resonators [8], microdisk resonators [9], splitters [6], and directional couplers [10]. DLSPP waveguides and devices have even been integrated onto SOI platforms for efficient interfacing with conventional silicon photonics [11]. An example of this is shown in Figure 1.4.

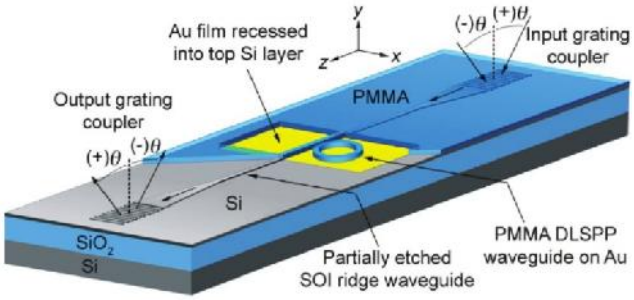

Figure 1.4: Dielectric loaded plasmonic waveguide and waveguide ring ring resonator integrated with a conventional SOI photonic ridge waveguide from [11].

1.3.3 Channel Plasmonic Waveguides

Channel plasmon polaritons (CPPs) are supported by grooves cut into a metallic surface, normally gold or silver. The most common examples are a 'V' shaped groove. Simple ion milling or an anisotropic wet etch of the metal surface is all that is required to fabricate these waveguides. The first experimental observation of CPPs at telecommunication wavelengths was conducted by Bozhevolnyi et al [12] using focused ion beam lithography of a gold surface. The 600 nm wide and 1 µm deep groove in gold was shown to support a low loss (~100 µm) and reasonably well confined (~1.1 µm in air) mode. The mode is guided by the bottom tip of the 'V' groove, which is what gives CPPs their strong confinement even in air. Numerous optical circuit components have been developed based on CPPs [13] such as splitters, interferometers, and ring resonators, examples of which are depicted in Figure 1.5. Unfortunately, despite the ease of fabrication CPP waveguides, detecting the signal is difficult with near-field scanning optical microscopy (NSOM) being relied upon to measure the field

just above the metal film. To date, there have been no demonstrations of integrated coupling of CPPs and conventional silicon photonics.

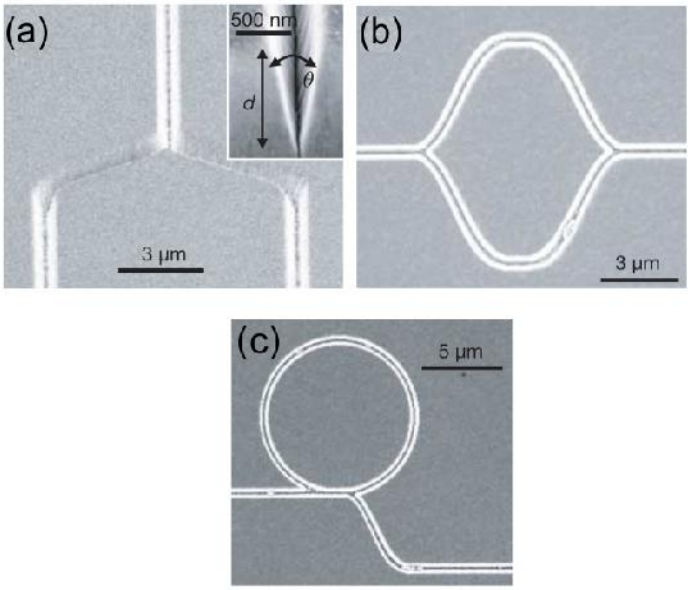

Figure 1.5: Scanning electron microscopy (SEM) images of CPP waveguide (a) splitter, (b) interferometer, and (c) ring resonator from [13]. Inset is SEM images of the CPP waveguide.

1.3.4 Insulator-Metal-Insulator Plasmonic Waveguides

Insulator-metal-insulator (IMI) plasmonic waveguides, carrying the long range surface plasmon polariton (LRSPP) mode, is another class of plasmonic waveguides. These waveguides have been extensively studied since their first experimental demonstration in 2000 [14]. The LRSPP mode arises from the coupling of two symmetric SPP modes on either side of a metal stripe embedded in a dielectric as depicted in Figure 1.6 (a). IMI waveguides and the LRSPP mode have propagation lengths on the order of millimeters, but with modal confinement

limited to micrometer scales in the telecommunications band. The propagation length of the LRSPP mode inversely dependent on the width of the metal stripe, though the modal extent increases comparatively. Single mode operation is reached at a sufficiently small metal stripe width and thickness [15]. As the metal stripe vanishes, this mode evolves smoothly into the TEM mode supported by the background dielectric [16]. The Gaussian-like field distribution of the LRSPP mode enables efficient excitation via end-fire coupling with single mode optical fibers. For example, a 14.5 nm thick and 2 μm wide Au stripe embedded in the polymer ZPU450 showed an impressive L_p=3.1 cm with a coupling loss of 3 dB per facet with a single mode optical fiber [15].

With the high propagation length of the LRSPP mode, the structure has been extensively exploited for integrated optics, primarily interconnects and other passive devices. Optical signal transmission up to 10 Gb/s [15] has been demonstrated with the LRSPP mode. Passive devices including Bragg grating, directional couplers, power splitters, interferometers, and bends, examples depicted in Figure 1.6 (b), have all been demonstrated [16]. However, other than [17], few examples exist of integrating IMI plasmonic waveguides with conventional silicon based technologies.

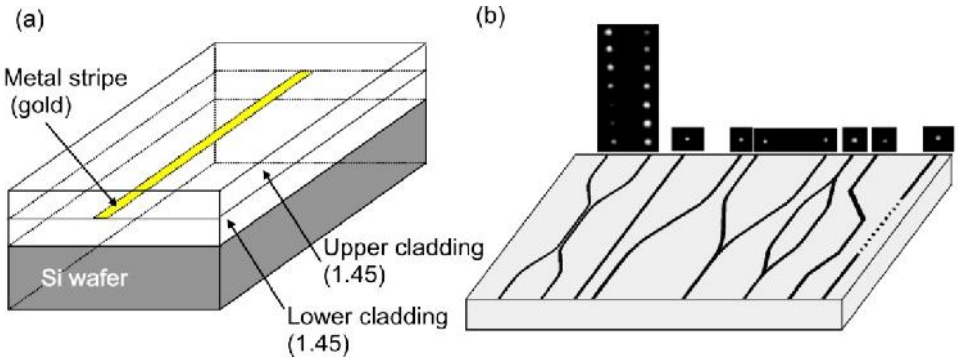

Figure 1.6: (a) Schematic of an IMI plasmonic waveguide from [15]. (b) A collection of passive LRSPP elements from [16] including directional coupler, power splitter, interferometer, and bend.

1.3.5 Metal-Insulator-Metal Plasmonic Waveguides

Unlike IMI plasmonic waveguides, metal-insulator-metal (MIM) plasmonic waveguides supporting the gap surface plasmon polariton (GSPP) mode sacrifice propagation length in favour of increased mode confinement. As two metal layers are brought close together across a dielectric gap, the individual single interface SPPs couple to one another across the dielectric gap to form the GSPP mode [4]. The lateral extent of this mode is limited purely by the dielectric gap width, though the propagation losses increase as the gap width is decreased. Common propagation lengths are on the order of a few microns. An extreme example of the subwavelength nature of the MIM configuration can be found in [18], wherein 830 nm light was focused into a 100nm wide Au/SiO_2/Au MIM waveguide with a SiO_2 gap of only 14 nm, though this device had a propagation length of only 880 nm. More practical waveguiding devices limit the dielectric core width from approximately 100-300 nm at the telecommunication wavelengths. A

representative example of a MIM plasmonic waveguide and its fundamental mode can be seen in Figure 1.6.

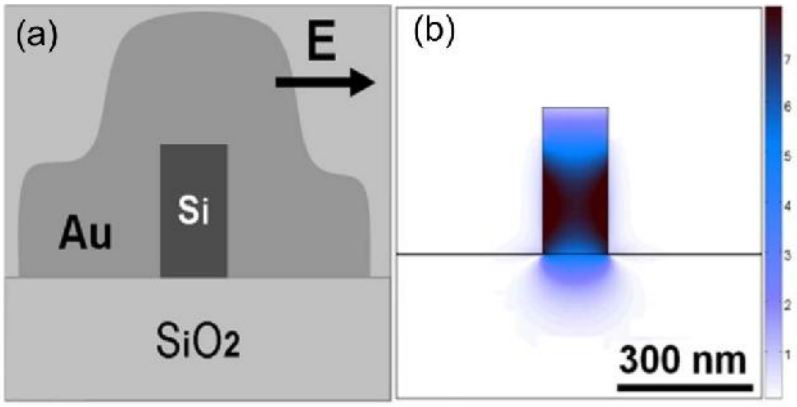

Figure 1.7: Images from [19]. (a) Schematic of a MIM plasmonic waveguide (b) Electric field mode distribution for the fundamental GSPP mode.

Though the limited propagation length of MIM plasmonic waveguides suggests they are unsuitable for long range interconnect applications, their nanoscale modal confinement recommends them for nonlinear devices reliant on high field intensities. In addition, the MIM configuration lends itself to easy integration onto a SOI platform through the use of silicon as the dielectric core. Several demonstrations of MIM plasmonic waveguides integrated with standard silicon photonic waveguides fabricated on SOI platforms exist [19-21].

1.4 Hybrid Plasmonic Waveguides

Recently, a new class of plasmonic waveguides has been introduced as a solution to the tradeoff between propagation length and modal confinement. First suggested by [22], the inclusion of a low index dielectric between a high index dielectric (nominally a semiconductor) and the metal layer was shown to dramatically increase the propagation length of a plasmonic system without sacrificing modal confinement through the creation of the hybrid plasmonic-photonic (HPP) mode. The concept came to prominence after the theoretical proposal in Oulton et al's Nature Photonics paper [23] of using semiconductor nanorods separated from a metal surface by a low index gap for waveguiding. Nanoscale confinement with propagation lengths ranging up to 150 μm at the telecommunication band were suggested. Soon afterwards, the same group experimentally demonstrated a plasmonic nanolaser (a CdS nanorod separated from a Ag surface by a 5 nm MgF_2 gap) in the visible spectrum based on the hybrid waveguide configuration with [24]. This configuration can be thought of as a metal-insulator-semiconductor or MIS plasmonic waveguide, which arises through the inclusion of a low index layer in a semiconductor based slab or dielectric loaded plasmonic waveguide. Since then, there have been numerous experimental demonstrations of MIS hybrid plasmonic waveguides [25-33], including a several based on CMOS compatible integration with conventional SOI photonics [30-33] as the configuration naturally lends itself to the use of Si with SiO_2. An example of integration of a 310 nm wide

Au(50nm)/SiO_2(70nm)/Si(325nm) MIS waveguide on a SOI platform with conventional silicon photonics from [31] is illustrated in Figure 1.8. The hybrid plasmonic waveguide demonstrated a propagation length of 105 µm and a coupling loss of -1.7 dB per interface at 1.55 µm.

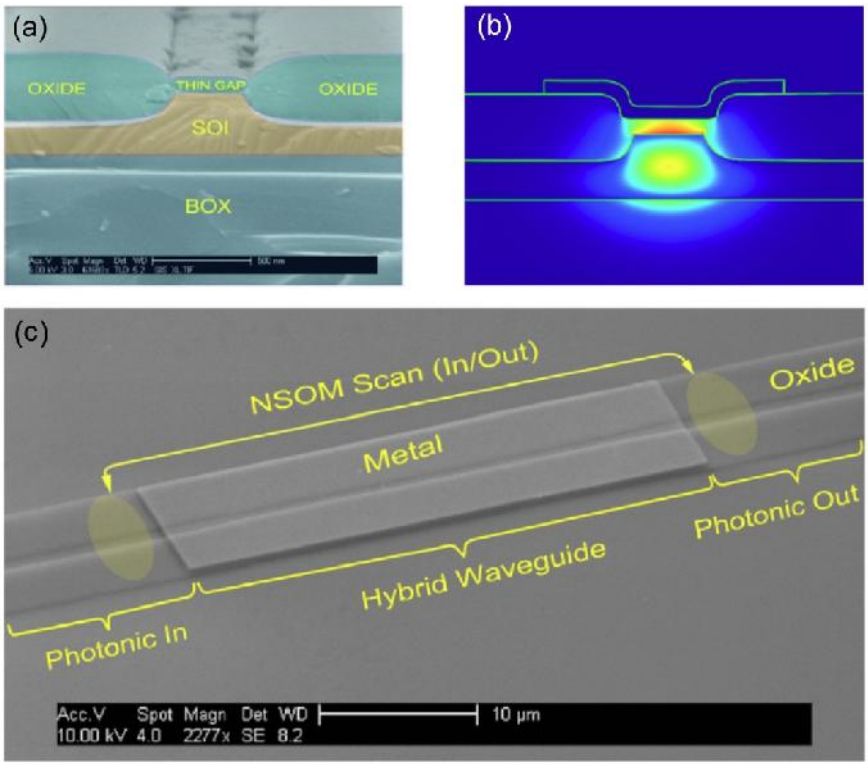

Figure 1.8: Images from [31]. (a) Cross sectional SEM image of hybrid plasmonic waveguide prior to Au deposition highlighting the various layers. (b) Simulated electric field intensity distribution of the fundamental mode. (c) SEM image of the hybrid plasmonic waveguide coupled to standard SOI photonic waveguides.

Another variation on the hybridization of plasmonic waveguides is the metal-insulator-metal-insulator-metal or MISIM hybrid plasmonic waveguide that arises from the inclusion of insulator spacer layers around the semiconductor core of a

MIM waveguide. Since hybridization of a plasmonic waveguide configuration does not sacrifice modal confinement, MIM waveguides have the most to gain from the increased propagation lengths that come from hybridization. This configuration has been used extensively in the creation of plasmonic nanolasers in the telecommunication band based on InGaAs [34-37]. Thus far, work on silicon based MISIM waveguides and their integration with conventional SOI photonics has been limited to a single group [38,39].

1.5 Active and Nonlinear Plasmonics

With the development of numerous passive and routing plasmonic devices based on the various waveguiding configurations, the next step in plasmonics is the creation of active and nonlinear devices. Active devices are a necessary requirement for the development of integrated nanoplasmonic circuitry. One area of interest has been the addition of gain into plasmonic systems to aid in the creation of nanoplasmonic amplifiers and lasers. Regrettably, the integration of gain into silicon based plasmonic systems remains unfulfilled. For further information on gain in plasmonic systems, the reader is directed to the Nature Photonics review article [40] and Chapter 5 of this thesis.

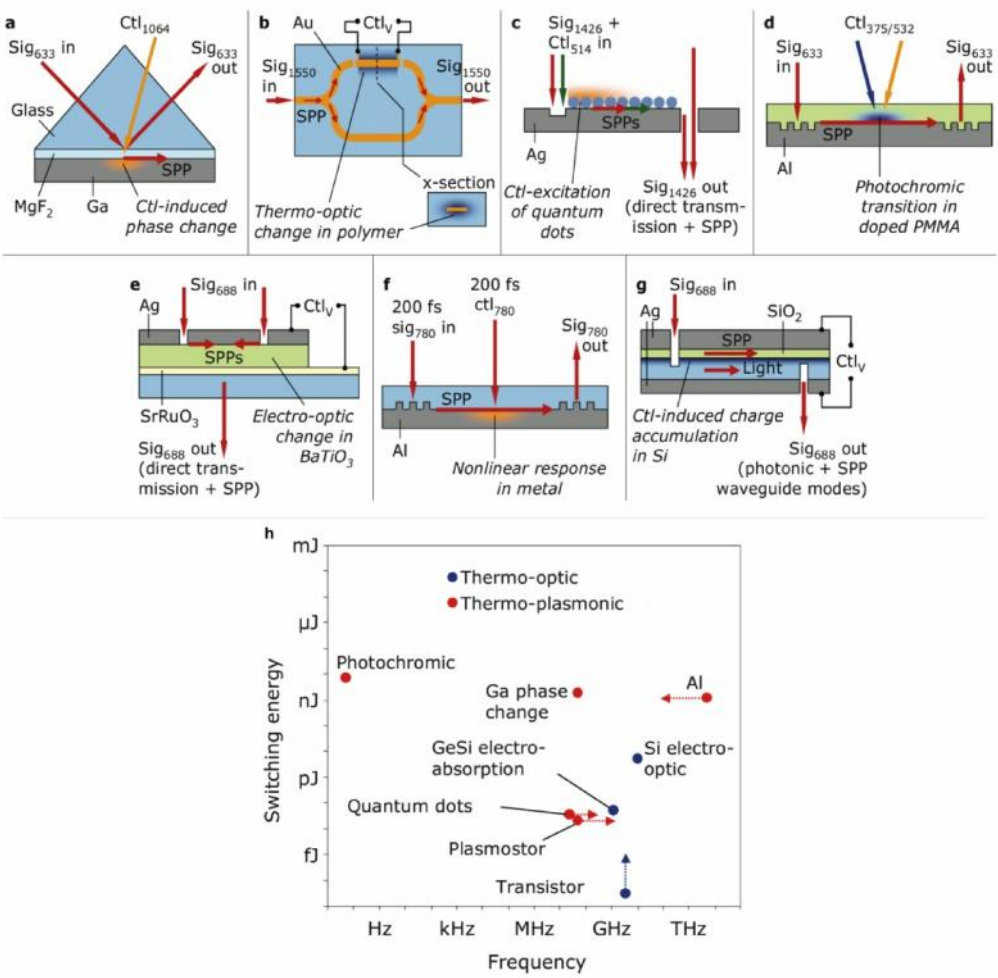

Figure 1.9: Images from [41]. Experimental plasmonic modulators with modulation mechanism: (a) Light-induced solid-liquid phase transition in gallium; (b) Voltage controlled refractive index change in LRSPP's dielectric cladding; (c) absorbance modulation of CdSe quantum dots; (d) photochromic switching of PMMA in a IM waveguide; (e) electro-optic modulation of the refractive index of barium titanate; (f) ultrafast optical excitation of aluminum; (g) carrier redistribution in silicon. (h) Switching energy and cycling frequency characteristics for active plasmonic modulation technologies (red) compared to existing photonic/electronic technologies (blue).

The ultimate goal of research in current active and nonlinear plasmonics remains a plasmonic analogue to the electronic transistor. This will require ultrafast modulation and switching of a plasmonic signal in the nanoscale. Since a

plasmonic mode is highly dependent of the refractive index of the materials that support it, many of the current modulation techniques involve modification of the refractive index of the dielectric or metal supporting the SPP mode. Figure 1.9 (a-g) depicts a number of these modulation schemes for SPPs with their characteristic switching frequency and energy per bit in Figure 1.9 (h). In these schemes, the modulation control is achieved externally by one of three methods: thermo-optic [42], electronic [43], or all-optical [44]. Thermo-optic modulation affects a refractive index change in the dielectric component of a plasmonic device by varying the temperature, generally using a simple resistive heating element. However, this modulation technique is almost six orders of magnitude slower than conventional electronics. Electronics-controlled modulation of the refractive index of the dielectric component of the plasmonic device is accomplished through direct carrier injection and re-distribution. Finally, all-optical control can be used to modulate a plasmonic signal by modulating the material properties of either the dielectric or metal component. Only all-optical modulation has the possibility of modulation speeds above and beyond those currently demonstrated by conventional electronics. However, many of the all-optical modulation methods require the use of an external pump laser to directly affect the material properties, which makes fully integrated nanoplasmonic circuitry unpractical.

By taking advantage of the nonlinear properties of materials, fully integrated plasmonic all-optical plasmonic modulators become possible. The material properties of the nonlinear dielectric in a plasmonic device could be controlled

through the use of a high intensity pump signal, thereby modulating a low intensity probe signal without worrying about self-modulation of the probe signal. Both the probe and pump signal can therefore take advantage of the same on-chip routing technologies. This method is especially attractive for silicon plasmonics. The variety of nonlinear effects exploited in silicon photonics [45] are already being examined for use in the field of silicon plasmonics [46]. Silicon's indirect band structure and centrosymmetry mean that the third order nonlinear process two-photon absorption is a lead contender for the method of all-optical modulation. The method of two-photon absorption and silicon's band structure can be seen in Figure 1.10.

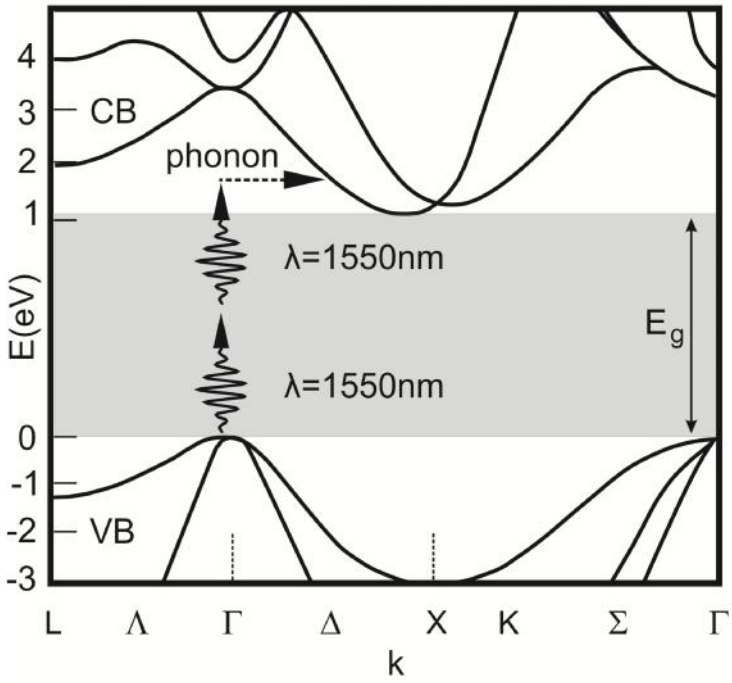

Figure 1.10: Band structure of silicon on an energy versus momentum plot. Depicts the indirect bandgap of 1.11 eV for silicon, as well as the two photon absorption process at λ=1550 nm.

Recently, a novel nanoscale logic gate based on interferometry of SPPs in MIM waveguides on silicon was demonstrated [47]. By relying only on the interference of identical SPP signals, it gives rise to another possible approach to low power ultrafast plasmonic switching.

1.6 Thesis Scope

Detailed descriptions of the equipment used in constructing the experimental setup are included to Chapter 2. This experimental setup was used for characterizing the nanoplasmonic devices investigated in Chapter 3 and Chapter 4. From this, interested readers will have the capacity to replicate the work if desired.

Chapter 3 describes the design, fabrication and characterization of silicon based MISIM hybrid nanoplasmonic waveguides. Due to the relatively unexplored nature of this plasmonic waveguide configuration, a focus is put on the effect the use of various materials has on the waveguide properties. The use of Ag, Au, and Cu as the MISIM metal cladding and HfO_2 and SiO_2 as the insulating spacer layers is explored. Experimental and theoretical results are compared for the propagation length and coupling efficiency to standard silicon photonic waveguides at 1.55 μm for each of the material combinations in order to determine the suitability of bulk material data for the theoretical predictions. Nanoring waveguide resonators were fabricated, but broadband spectral characterization revealed no significant resonances.

Moving slightly away from the focus on mode confinement to allow for a longer propagation length, the design, fabrication and characterization of $Au/SiO_2/Si$ MIS hybrid nanoplasmonic waveguides was undertaken as discussed in Chapter 4. The MIS nanoplasmonic waveguides are characterized for propagation length and coupling efficiency to standard silicon photonic waveguides at 1.55 µm. The properties of the MIS nanoplasmonic waveguides are used in the successful design of linear distributed Bragg reflector resonators based on the selective removal of the Au capping layer to form a central cavity surrounded by tapered Bragg mirrors. The MIS nanoplasmonic waveguides are used in the formation of waveguide ring resonators and micro disk resonators as well.

Since a major drawback of any plasmonic systems is the large ohmic losses and, consequently, the short propagation lengths of plasmonic waveguides, the introduction of gain into plasmonic systems has been suggested as a solution to this problem. As such, in Chapter 5 the gain characteristics of an electrically-pumped MISIM nanoplasmonic $In_{0.485}Ga_{0.515}As$ amplifier design for the telecommunications wavelength of 1.55 µm are investigated through nonlinear 3-D FDTD simulations. The rate equations model developed for the simulations is compared to a conventional semiconductor optical amplifier model. The effect of integrating the nanoplasmonic amplifier into an interconnect network is studied.

Modulators and other switching devices form the cornerstone of optical circuits. For plasmonics to become an integral part of next generational optical circuits, plasmonic devices capable of efficient signal modulation must be

incorporated onto the conventional SOI platform. Chapter 6 presents a study of all-optical modulation in a silicon based MISIM nanoring resonator based on two photon absorption (TPA) using nonlinear 3-D FDTD simulations. The modulation characteristics in the telecommunication band of three separate devices are explored at a variety of pump pulse energies.

In Chapter 7, explores the possibility of 3-D integration of plasmonic circuits through signal transfer between vertically coupled MIM nanoring resonators. The coupled nanoring resonators are evanescently coupled to MIM bus plasmonic waveguides on several device layers. The effect of the nanoring radii and bus waveguide orientation on the frequency selective signal transfer is determined through 3-D FDTD simulations.

Chapter 1 References

[1] D. K. Gramotnev and S. I. Bozhevolnyi, “Plasmonics beyond the diffraction limit,” Nat. Photon. **4**, 83-91 (2010).

[2] E. Ozbay, “Plasmonics: merging photonics and electronics at nanoscale dimensions,” Science **311**, 189-193 (2006).

[3] S. Sederberg, V. Van, and A. Y. Elezzabi, “Monolithic integration of plasmonic waveguides into a complimentary metal-oxide-semiconductor- and photonic-compatible platform,” Appl. Phys. Lett. **96**, 121101 (2010).

[4] S. I. Bozhevolnyi, “Introduction to Surface Plasmon-Polariton Waveguides,” in *Plasmonic Nanoguides and Circuits*, S. I . Bozhevolnyi, eds. (Pan Standford, Singapore, 2009), pp. 1-32.

[5] S. Sederberg, V. Van, and A. Y. Elezzabi, “Monolithic integration of plasmonic waveguides into a complimentary metal-oxide-semiconductor- and photonic-compatible platform,” Appl. Phys. Lett., **96**, 121101 (2010).

[6] A. V. Krasavin and A. V. Zayats, "Passive photonic elements based on dielectric-loaded surface plasmon polariton waveguides," Appl. Phys. Lett. **90**, 211101 (2007).

[7] A. Kumar, J. Gosciniak, V. S. Volkov, S. Papaioannou, D. Kalavrouziotis, K. Vyrsokinos, J. C. Weeber, K. Hassan, L. Markey, A. Dereux, T. Tekin, M. Waldow, D. Apostolopoulos, H. Avramopoulous, N. Pleros, and S. I. Bozhevolnyi, “Dielectric-loaded plasmonic waveguide components:

Going practical," Laser Photon. Rev., DOI: 10.1002/lpor.201200113 (2013).

[8] T. Holmgaard, Z. Chen, S. I. Bozhevolnyi, L. Markey, and A. Dereux, "Dielectric-loaded plasmonic waveguide-ring resonators," Opt. Express **17**, 2968-2975 (2009).

[9] S. Randhawa, A. V. Krasavin, T. Homgaard, J. Renger, S. I. Bozhevolnyi, A. V. Zayats, and R. Quidant, "Experimental demonstration of dielectric-loaded plasmonic waveguide disk resonators at telecom wavelengths," Appl. Phys. Lett. **98**, 161102 (2011).

[10] T. Holmgaard, Z. Chen, S. I. Bozhevolnyi, L. Markey, and A. Dereux, "Design and characterization of dielectric-loaded plasmonic directional couplers," J. Lightwave Technol. **27**, 5521-5528 (2009).

[11] R. M. Briggs, J. Grandidier, S. P. Burgos, E. Feigenbaum, and H. A. Atwater, "Efficient coupling between dielectric-loaded plasmonic and silicon photonic waveguides," Nano. Lett. **10**, 4851-4857 (2010).

[12] S. I. Bozhevolnyi, V. S. Volkov, E. Devaux, and T. W. Ebbesen, "Channel plasmon-polariton guiding by subwavelength metal grooves," Phys. Rev. Lett. **95**, 046802 (2005).

[13] S. I. Bozhevolnyi, V. S. Volkov, E. Devaux, J. Y. Lauet, and T. W. Ebbesen, "Channel plasmon subwavelength waveguide components including interferometers and ring resonators," Nature **440**, 508-511 (2006).

[14] R. Charbonneau, P. Berini, E. Berolo, and E. L. Shrzek, “Experimental observation of plasmon polariton waves supported by a thin metal film of finite width,” Opt. Lett. **25**, 844-846 (2000).

[15] S. Park, M. S. Kim, J. T. Kim, S. K. Park, J. J. Ju, and M. H. Lee, “Long range surface plasmon polariton waveguides at 1.31 and 1.55 μm wavelengths,” Opt. Commun. **281**, 2057-2061 (2008).

[16] P. Berini, “Integrated optics based on long-range surface plasmon polaritons,” in *Surface Plasmon Polaritons*, M. L. Brongersma and P. G. Kik, eds. (Springer, Dordrecht, 2007), pp. 217-233.

[17] V. Giannini, Y. Zhang, M. Forcales, and J. G. Rivas, “Long-range surface polaritons in ultra-thin films of silicon,” Opt. Express **16**, 19674-19685 (2008).

[18] H. Choo, M. K. Kim, M. Staffaroni, T. J. Seok, J. Bokor, S. Cabrini, P. J. Schuck, M. C. Wu, and E. Yablonovitch, “Nanofocusing in a metal-insulator-metal gap plasmon waveguide with a three-dimensional linear taper,” Nat. Photonics **6**, 838-844 (2012).

[19] L. Chen, J. Shakya, and M. Lipson, “Subwavelength confinement in an integrated metal slot waveguide on silicon,” Opt. Lett. **31**, 2133-2135 (2006).

[20] Z. Han, A. Y. Elezzabi, and V. Van, “Experimental realization of subwavelength plasmonic slot waveguides on a silicon platform,” Opt. Lett. **35**, 502-504 (2010).

[21] L. Y. M. Tobing, L. Tjahjana, and D. H. Zhang, "Demonstration of low-loss on-chip integrated plasmonic waveguide based on simple fabrication steps on silicon-on-insulator platform," Appl. Phys. Lett. **101**, 041117 (2012).

[22] R. Salvador, A. Martinez, C. G. Meca, R. Ortuno, and J. Marti, "Analysis of hybrid dielectric plasmonic waveguides," IEEE J. Sel. Top. Quant. Electron. **14**, 1496-1501 (2008).

[23] R. F. Oulton, V. J. Sorger, D. A. Genov, D. F. P. Pile, and X. Zhang, "A hybrid plasmonic waveguide for subwavelength confinement and long-range propagation," Nat. Photonics **2**, 496-500 (2008).

[24] R. F. Oulton, V. J. Sorger, T. Zentgraf, R. M. Ma, C. Gladden, L. Dai, G. Bartal, and X. Zhang, "Plasmon lasers at deep subwavelength scale," Nature **461**, 629-632 (2009).

[25] Z. Fang, S. Huang, F. Lin, and X. Zhu, "Colour-tuning and switching optical transport through CdS hybrid plasmonic waveguide," Opt. Express **17**, 20327-20332 (2009).

[26] J. T. Kim, J. J. Ju, S. Park, M. Kim, S. K. Park, and S. Y. Shin, "Hybrid plasmonic waveguide for low loss lightwave guiding," Opt. Express **18**, 2808-2813 (2010).

[27] J. T. Kim, S. Park, J. J. Ju, S. Lee, and S. Kim, "Low bending loss characteristics of hybrid plasmonic waveguide for flexible optical interconnect," Opt. Express **18**, 24213-24220 (2010).

[28] J. Tian, Z. Ma, Q. Li, Y. Song, Z. Liu, Q. Yang, C. Zha, J. Akerman, L. Tong, and M. Qiu, "Nanowaveguides and couplers based on hybrid plasmonic modes," Appl. Phys. Lett. **97**, 231121 (2010).

[29] F. Lou, Z. Wang, D. Dai, L. Thylen, L. Wosinski, "Experimental demonstration of ultra-compact directional couplers based on silicon hybrid plasmonic waveguides," Appl. Phys. Lett. **100**, 241105 (2012).

[30] M. Wu, Z. Han, and V. Van, "Conductor-gap-silicon plasmonic waveguides and passive components at subwavelength scale," Opt. Express **18**, 11728-11736 (2010).

[31] I. Goykhman, B. Desiatov, and U. Levy, "Experimental demonstration of locally oxidized hybrid silicon-plasmonic waveguide," Appl. Phys. Lett. **97**, 141106 (2010).

[32] X. Sun, M. Z. Alam, S. J. Wagner, J. S. Aitchison, and M. Mojahedi, "Experimental demonstration of a hybrid plasmonic transverse electric pass polarizer for a silicon-on-insulator platform," Opt. Lett. **37**, 4814-4816 (2012).

[33] S. Zhu, G. Q. Lo, and D. L. Kwong, "Experimental demonstration of vertical Cu-SiO_2-Si hybrid plasmonic waveguide components on an SOI platform," IEEE Photon. Technol. Lett. **24**, 1224-1226 (2012).

[34] M. T. Hill, M. Marell, E. S. Leong, B. Smalbrugge, Y. Zhu, M. Sun, P. J. van Veldhoven, E. J. Geluk, F. Karouta, Y. S. Oei, R. Nöetzel, C. Z. Ning, and M. K. Smit, "Lasing in metal-insulator-metal sub-wavelength plasmonic waveguides," Opt. Express **17**, 11107-11112 (2009).

[35] M. J. H. Marell, B. Smalbrugge, E. J. Geluk, P. J. van Veldhoven, B. Barcones, B. Koopmans, R. Nöetzel, M. K. Smit, and M. T. Hill, “Plasmonic distributed feedback lasers at telecommunications wavelengths,” Opt. Express **19**, 15109-15118 (2011).

[36] J. H. Lee, M. Khajavikhan, A. Simic, Q. Gu, O. Bondarenko, B. Slutsky, M. P. Nezhad, and Y. Fainman, “Electrically pumped sub-wavelength metallo-dielectric pedestal pillar lasers,” Opt. Express **19**, 21524-21531 (2011).

[37] K. Ding, Z. C. Liu, L. J. Yin, M. T. Hill, M. J. H. Marell, P. J. van Veldhoven, R. Nöetzel, and C. Z. Ning, “Room-temperature continuous wave lasing in deep-subwavelength metallic cavities under electrical injection,” Phys. Rev. B **85**, 041301 (2012).

[38] S. Zhu, T. Y. Liow, G. Q. Lo, and D. L. Kwong, “Fully complementary metal-oxide-semiconductor compatible nanoplasmonic slot waveguides for silicon electronic photonic integrated circuits,” Appl. Phys. Lett. **98**, 021107 (2011).

[39] S. Zhu, G. Q. Lo, and D. L. Kwong, “Components for silicon plasmonic nanocircuits based on horizontal Cu-SiO_2-Si-SiO_2-Cu nanoplasmonic waveguides,” Opt. Express **20**, 5867-5881 (2012).

[40] P. Berini and I. D. Leon, "Surface plasmon-polariton amplifiers and lasers," Nat. Photonics **6**, 16-24 (2012).

[41] K. F. MacDonald and N. I. Zheludev, “Active plasmonics: current status,” Laser Photon. Rev. **4**, 562-567 (2010).

[42] T. Nikolajsen, K. Leosson, and S. I. Bozhevolnyi, “Surface plasmon polariton based modulators and switches operating at telecom wavelengths,” Appl. Phys. Lett. **85**, 5833-5835 (2004).

[43] J. A. Dionne, K. Diest, L. A. Sweatlock, and H. A. Atwater, “PlasMOStor: a metal-oxide-Si field effect plasmonic modulator,” Nano Lett. **9**, 897–902 (2009).

[44] J. N. Caspers, N. Rotenberg, and H. M. van Driel, “Ultrafast silicon-based active plasmonics at telecom wavelengths,” Opt. Express **18**, 19761–19769 (2010).

[45] H. K. Tsang and Y. Liu, "Nonlinear optical properties of silicon waveguides," Semiconductor Science and Technology **23**, 064007 (2008).

[46] I. D. Rukhlenko, M. Premaratne, and G. P. Agrawal, "Nonlinear propagation in silicon-based plasmonic waveguides from the standpoint of applications," Opt. Express **19**, 206-217 (2011).

Chapter 2

Experimental Setup

2.1 Overview

In order to characterize the devices designed in Chapters 3 and 4 of this thesis, an experimental setup was designed and built in the Ultrafast Optics and Nanophotonics Laboratory. This section gives a brief overview of the experimental setup, with further details about the individual elements described in the following section. A representative schematic of the experimental setup is shown in Figure 2.1.

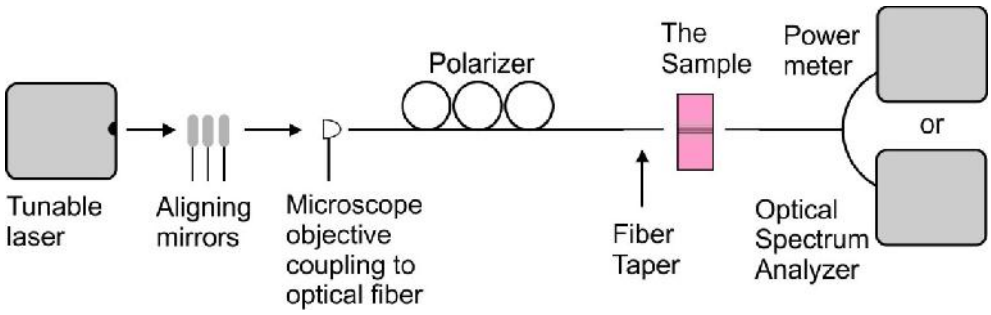

Figure 2.1: Schematic representation of the experimental setup. CW light around 1550 nm from a tunable laser is coupled into an optical fiber through aligning mirrors and a focusing microscope objective. After passing through a polarizer, the lensed fiber focuses the light to couple to waveguides on the chip via end-fire coupling. After interacting with the device, it couples to another lensed optical fiber and is collected by a photodetector connected to a power meter or by an optical spectrum analyzer.

The sample, a cleaved SOI chip containing several devices, is mounted on an optical stage equipped with positional piezoelectric motors in all three dimensions for alignment between the end facets of the sample and the lensed optical fibers for end-fire coupling of the laser light. The laser light, from a continuous wave (CW) diode laser from 1509-1581 nm, is coupled to a lensed optical fiber from free space using several aligning mirrors to focus the light on the optical fiber through a microscope objective. A flipper mirror enables toggling of the light source from this experimental setup to an adjacent one. The fiber passes through a polarizer before end-fire coupling to the coupling input photonic waveguides on the sample. By replacing the sample in the setup by a polarizing beam splitter cube, the polarizer could be adjusted to maximize the transmission of the appropriate polarization of the laser. The input/output (I/O) photonic waveguides carry the light to and from the devices. The signal end-fire couples from the output photonic waveguide and couples to a second lensed optical fiber. The output optical fiber is connected to either an infrared photodetector so that the signal intensity can be measured by a power meter or to an optical spectrum analyzer (OSA) for broadband spectral measurements. A schematic of the experimental setup can be seen in Figure 2.2.

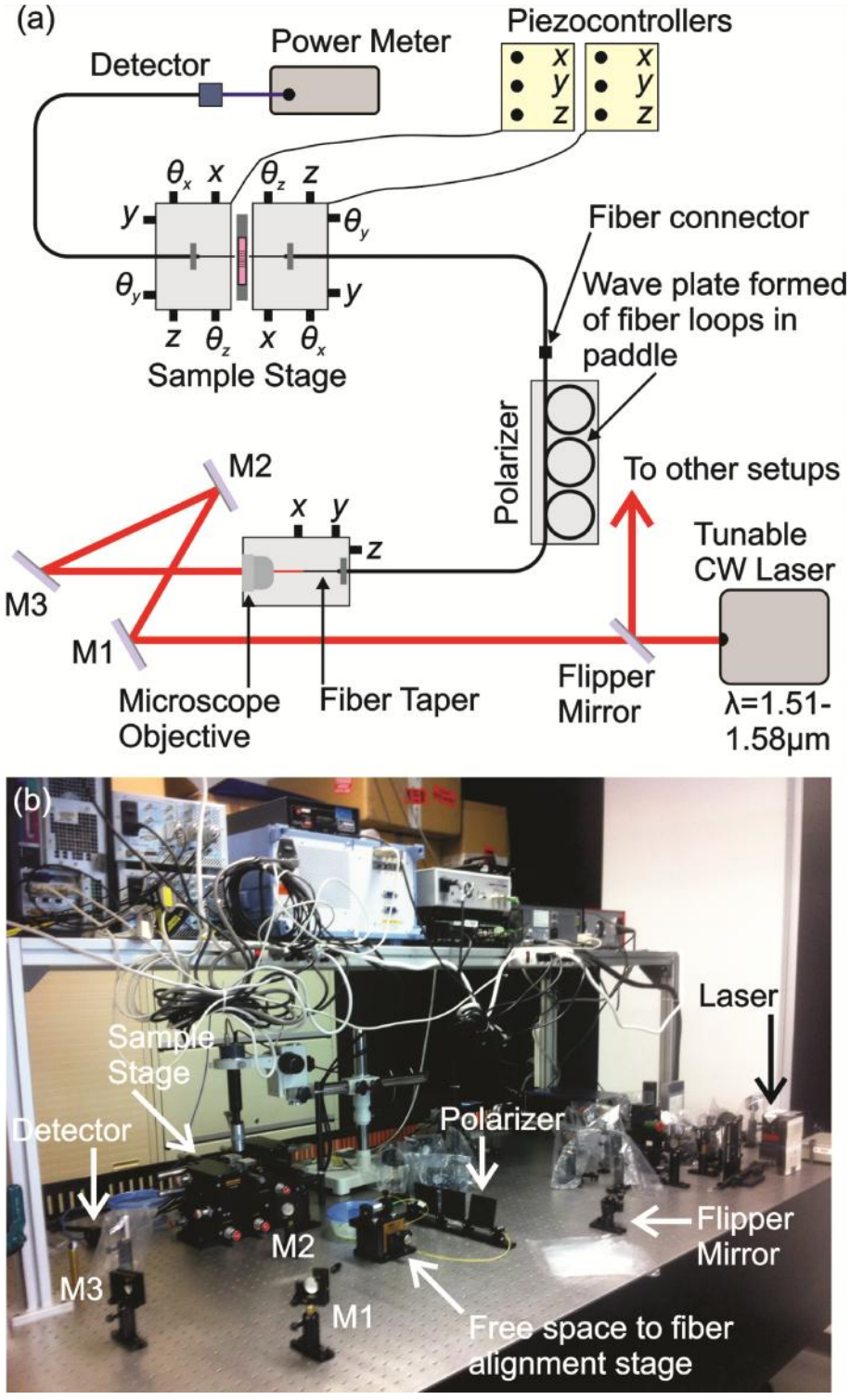

Figure 2.2: (a) Layout of experimental setup with transmitted power measured by the power meter. (b) Picture of the experimental setup.

2.2 Equipment

What follows are detailed descriptions of the equipment used in the experimental setup.

2.2.1 Tunable Diode Laser

The light source used in the experimental setup was a 6328 Velocity™ Tunable Diode Laser from New Focus Inc., capable of CW operation between 1509-1581 nm with 0.01 nm tuning resolution with a narrow linewidth of <200 kHz. The wavelength tuning is accomplished through the use of a piezoelectric controlled diffraction grating which angles only one wavelength toward the output. While the maximum output power of the electrically pumped InGaAs diode laser is 25 mW @ 1545 nm, in order to maintain temperature stability the pump current was kept below 90 mA and the output power was maintained at 10 mW at 1.55 µm. A picture of the laser is shown in Figure 2.3.

Figure 2.3: (a) Velocity™ Tunable Diode Laser and (b) laser controller.

2.2.21 Free Space Optics

With a flipper mirror toggled to direct the laser to this experimental setup, silver coated mirrors with protective SiO_2 layers from Thorlabs aligned the laser to a stage mounted microscope objective. The use of silver on the mirrors enables reflectivity of better than 97.5% in the wavelength range under consideration. Since both the laser source and microscope objective faced different directions and were at different heights, three mirrors (M1, M2, M3) were required to align the laser on the same plane as the microscope objective. The microscope objective (Carl Zeiss with a magnification of 10:1, numerical aperture (NA) of 0.30 and working distance (WD) of 5.2 mm) was fixed to a stage containing a mounted lensed optical fiber in a fiber coupler. The tapered end of the lensed optical fiber was aligned to the focal point of the microscope objective using *x*, *y* and *z* micrometer screw gauges. The alignment of both the mirrors and optical fiber were evaluated by connected the other fiber coupler mounted end of the optical fiber to a power meter and maximizing the transmitted power before each experiment. Between 25% and 37% of the laser output power could be coupled to the optical fiber this way, depending on the alignment. A picture of the free space optics used for alignment can be seen in Figure 2.4.

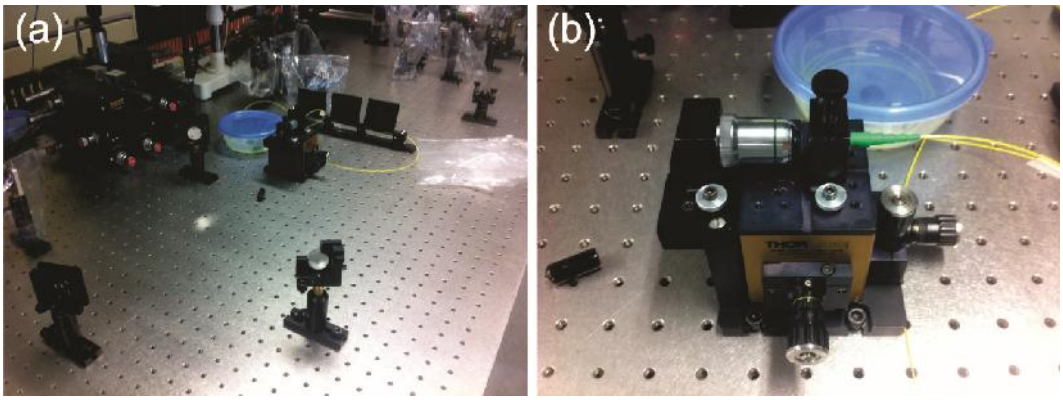

Figure 2.4: (a) Alignment mirrors and (b) free-space to fiber coupling alignment stage.

2.2.3 Fiber Optics and Polarizer

Three separate optical fibers were used in the experimental setup. All three fibers are laser shaped tapered and lensed single-mode Corning SMF28 fibers from OZ Optics with a 9 µm core diameter, 125 µm cladding diameter and 1 mm Acrylate jacket diameter. The tapered ends of the fibers have 55º taper angles with 5 µm radius of curvature, giving them a WD of 12 µm and a 2 µm spot size. Each end of the optical fiber is either fitted to a fiber connecter for mounting or coupling to other fibers or detectors, or has the last 7 mm of the fiber stripped of its coating to enable alignment and coupling to and from the samples. The first fiber, fitted with fiber couplers on both ends, was placed inside a FPC560 fiber polarization controller or polarizer from Thorlabs. One end of the first fiber was mounted to the free space alignment stage to receive the laser light from the microscope objective and the other end was connected to the second fiber. The other end of the second optical fiber was stripped to enable alignment to the end

facet of the sample and was custom mounted to the sample stage. The third optical fiber's stripped end was mounted to the sample stage on the output side of the sample and its fiber coupler fitted end connected to the power detector.

The polarizer was used to convert the elliptically polarized laser light into linearly polarized light. The polarizer was formed of three paddles containing the looped optical fiber, each of which creates an independent fractional, fixed wave plate whose angle could be manually adjusted to alter the polarization of the transmitted light through stress-induced birefringence along the length of fiber. By measuring the power transmitted through a birefringent SF2 glass PBS104 polarizing beamsplitter cube from Thorlabs, which splits the signal into reflected *s*-polarized and transmitted *p*-polarized components, placed on the sample stage, the polarization of the transmitted light could be made >95% TE (for the devices in Chapter 3) or TM (for the devices in Chapter 4). A picture of this portion of the experimental setup can be seen in Figure 2.5.

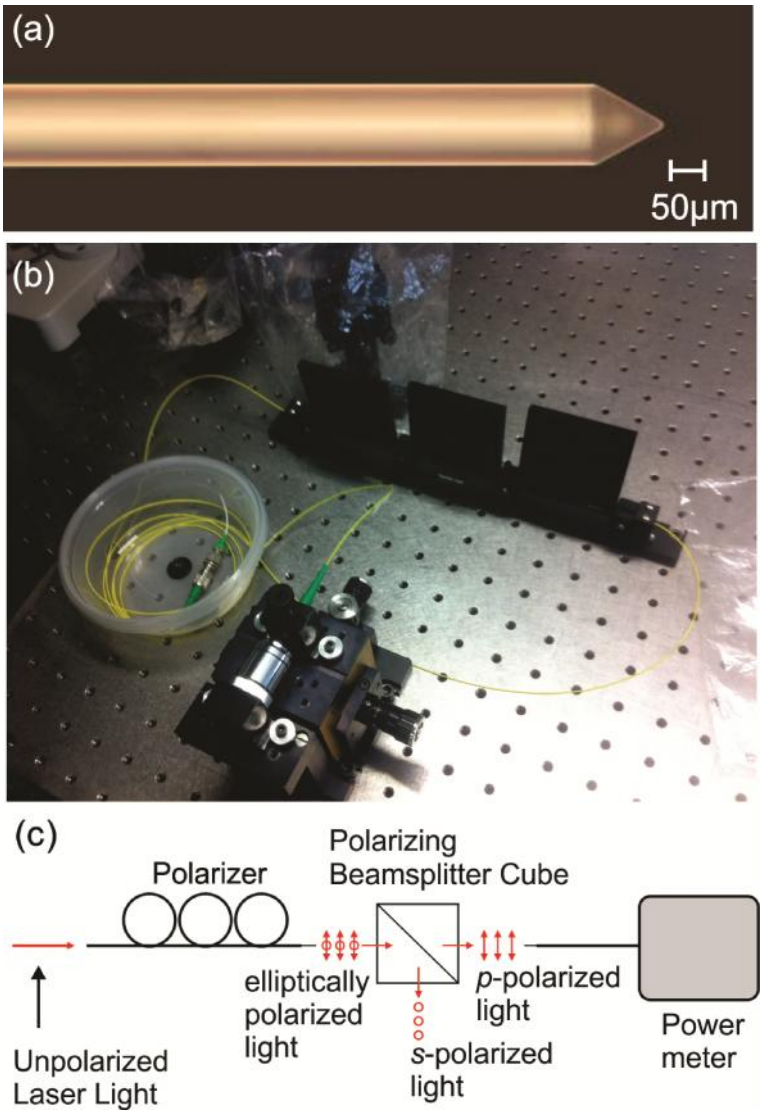

Figure 2.5: (a) Stripped end of an optical fiber. (b) Polarizer, fiber to fiber connector and free-space to fiber coupling alignment stage. (c) Schematic of experimental setup for determining the signal polarization.

2.2.4 Sample Stage

The stripped ends of the I/O lensed optical fibers are custom mounted onto 17MAX600 stages from Melles Griot with six micrometer screw gauges for alignment in x, y, z, θ_x, θ_y and θ_z directions. CVI model 17BPC203

piezocontrollers enable increased alignment accuracy in the *x*, *y* and *z* directions by increasing the resolution down to 4 nm. The sample under consideration was placed on a 2 mm wide pillar between the fiber alignment stages. Alignment of the I/O optical fibers to the cleaved end facets of the coupling SOI waveguides on the sample was initially done visually with the micrometer screw gauges using a CCD camera with a microscope objective whose output could be seen on a television. After the initial alignment, the transmitted power could be maximized using the piezocontrollers. Approximately 15% coupling efficiency per interface was found between the lensed optical fibers and the cleaved end facets of the coupling SOI waveguides. A picture of the sample stage can be seen in Figure 2.6.

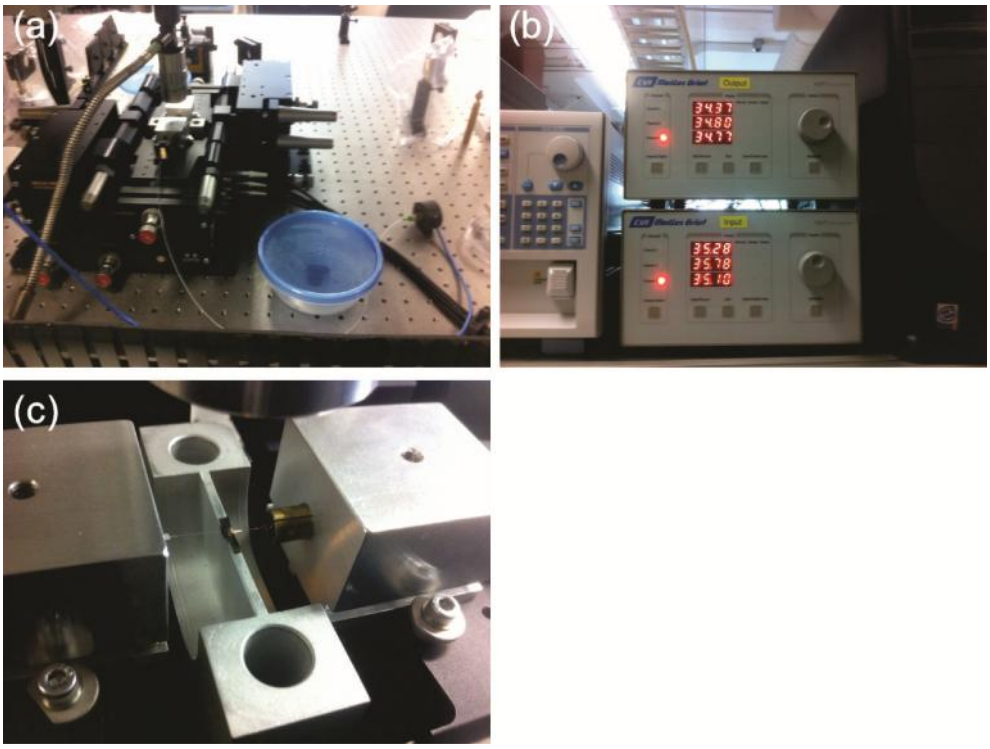

Figure 2.6: (a) Sample stage with (b) piezocontrollers. (c) Sample with aligned optical fibers.

2.2.5 Infrared Power Detector and Meter

The fiber connector end of the output optical fiber could be connected to the enclosed housing of a 3mm diameter germanium photodiode infrared power detector model 818-IR from Newport Corporation. The photodiode power detector was capable of detection of powers ranging from a few nanowatts up to 2 mW with 3% accuracy at λ=800-1800 nm. The detector was attached to a 835 digital power meter from Newport Corporation for reading the output power of devices at λ=1.55 μm.

2.2.6 Optical Spectrum Analyzer

For broadband spectral measurements, the fiber connector end of the output optical fiber was connected to an AQ6370C optical spectrum analyzer capable of measurements in the wavelength range of λ=600-1700 nm with 0.01 nm resolution. Before operation, the OSA underwent wavelength calibration using a built in 40 nW reference source at λ=1.55 μm. The Matlab program *Laser_Scan.m* described in Appendix A was used to control both the OSA and laser source and record the results during broadband measurements.

Chapter 3

Nanoplasmonic MISIM Waveguides and Resonators on a Silicon Platform[1]

3.1 Background

Of the proposed conventional plasmonic waveguiding configurations, the realized metal-insulator-metal (MIM) plasmonic waveguides [1-4] have been demonstrated as prime candidates for high density integration of plasmonic waveguides on the chip scale. This is because, in MIM waveguides, the lateral mode confinement is entirely determined by the insulator thickness [5], allowing for the insulating gap to be reduced down to nanometer dimensions if desired. However, like all conventional plasmonic waveguiding configuration, there is an inherent tradeoff between modal confinement and propagation length. In this class of plasmonic waveguides, the tighter the confinement, the greater the losses. In

[1] *A version of this chapter has been submitted for publication. M. P. Nielsen, A. Ashfar, K. Cadien, and A. Y. Elezzabi, Opt. Material, OM-D-13-00549, submitted June 4, 2013.*

addition, the use of a Si core for the waveguide, necessary for monolithic integration with existing electronic-photonic integrated circuits (EPICs) based on standard silicon CMOS technology, further increases the losses of the MIM plasmonic waveguide as propagation losses increase for higher core index. It has been proposed that the high losses in plasmonic waveguides can be mitigated through intelligent design which includes a thin low index spacer layer between the high index core and the metal layers [6]. The hybrid plasmonic waveguide suffers reduced losses without increasing modal volume. Incorporating this into the MIM configuration creates the metal-insulator-semiconductor-insulator-metal (MISIM) waveguide geometry carrying a hybrid plasmonic-photonic mode. Further loss reduction in silicon based MISIM plasmonic waveguides relies upon careful choice of the materials and structure of the waveguide.

To date, the MISIM plasmonic waveguide geometry remains relatively unexplored at telecommunication wavelengths. An InGaAs-based nanolaser near 1500 nm at 78 k [7] was the first demonstrated example of the MISIM geometry. Further improvements on the nanolaser design enabled lasing to occur at room temperatures [8]. However, with the focus on lasing in InGaAs, no characterization of the waveguiding or material properties of the designs was conducted. In addition, InGaAs is not a CMOS compatible material for large scale integration and processing. More recently, Al/SiO_2/Si/SiO_2/Al MISIM plasmonic waveguides on a silicon-on-insulator (SOI) platform for CMOS compatibility were demonstrated [9]. However, aluminum's unsuitability for plasmonic applications at telecommunication wavelengths [10] resulted in propagation losses

as high as 1.63 dB/µm (propagation length L_p=2.66 µm) at 1.55 µm. To retain CMOS compatibility, the Al cladding was changed to Cu to create $Cu/SiO_2/Si/SiO_2/Cu$ MISIM plasmonic waveguides [11]. However, the experimental result of propagation lengths in excess of 15µm at 1.55µm for the Cu clad MISIM waveguides is questionable. This long propagation length is much higher than any predicted or realized propagation lengths for similar MISIM waveguides using Au or any other metal. Furthermore, the reported propagation distance of 15µm does not agree with theoretical models based on the widely used material data from [12] that shows Cu as considerably worse than Au for low loss plasmonic waveguiding in the telecommunication band. This shows that further study into the materials used for the design of MISIM plasmonic waveguides and devices is required.

Due to its stability and relatively low loss, Au is the most common metal used in nanoplasmonic devices. However, it often requires an adhesion layer, such as Cr or Ti, in order to be practically put into use. This adhesion layer adds considerable losses to the SPP mode. In addition, the experimental results for gold plasmonic waveguides of similar structures [13,14] have shown vastly different results. Silver, the other common plasmonic noble metal, has the lowest loss at telecommunication wavelengths around 1.55 µm [10], but is often associated with fabrication challenges. However, neither of these metals is compatible with electronic CMOS fabrication processes. Copper, on the other hand, is a CMOS compatible metal, though often requires a lossy diffusion barrier to prevent metal ions from diffusing into Si. If the barrier layer is neglected, the metal ions will

provide optical absorption sites in an otherwise effectively lossless material, but effect of including a barrier layer is similar to that of an adhesion layer for Au. However, the results on the use of Cu as a plasmonic material have been contradictory, with material data showing Cu either considerably worse [12] or better [15] than Au for low loss plasmonic waveguiding in the telecommunication band. This makes determining the correct choice of Cu material data for modeling of plasmonic structures a critical one. Due to the high field concentration along material interfaces in nanoplasmonic devices, a crucial factor in device losses is the quality of the interfaces, primarily the metal-dielectric interfaces. Conformal growth of high quality dielectrics is required for smooth interfaces. Both silicon dioxide (SiO_2) and hafnium dioxide (HfO_2), important dielectrics for CMOS processes, are capable of high quality conformal growth.

3.2 Design of MISIM Waveguides and Ring Resonators

The focus of this chapter is the investigation of the MISIM class of nanoplasmonic waveguides for their superior field confinement compared to other classes of plasmonic waveguides, and the exploration into using MISIM waveguides for ring resonator devices. As this greater field confinement comes at the cost of increased propagation losses, it is important to design the waveguides to minimize these losses. To this end, the effect of various plasmonic materials on the propagation losses of MISIM waveguides was studied. Three metals, the

common plasmonic noble metals Au and Ag and the CMOS compatible Cu, and two insulators, the ubiquitous SiO_2 and the high dielectric permittivity insulator HfO_2, were studied in different combinations to form MISIM waveguides and their propagation lengths were determined experimentally and compared to theoretical calculations. Nanoring resonators, based on the MISIM waveguides, were designed and characterized experimentally.

Prior to fabrication and characterization of the MISIM nanoplasmonic waveguides, 3-D self-consistent finite difference time domain (FDTD) simulations using the commercial software Lumerical FDTD Solutions were used to determine the optimum waveguide dimensions using material data for the complex refractive index of Ag [12], Au [12], Cu [12], HfO_2 [16], SiO_2 [17], and Si [17]. Further information on the FDTD simulations using Lumerical FDTD Solutions can be found in Appendix B. Since these simulations rely on bulk material properties, the discrepancy between theoretical and experimental results can be used to determine the applicability of bulk material data for nanoscale applications. The two most important considerations in designing MISIM nanoplasmonic waveguides for interconnect applications are minimizing both the waveguide losses and its spatial footprint. However, as previously mentioned, these two considerations are mutually exclusive. Thus, when designing a nanoplasmonic waveguide structure, a compromise must be made between the spatial footprint and the inherent losses. While MIM type geometries, and by extension MISIM waveguides, have no lower limit on their core size, as the core size decreases, more of the optical field is coupled into the metal layer [5], greatly

increasing losses. In order to obtain nanoscale footprint waveguiding far below the diffraction limit spot size at 1.55 µm while minimizing losses, the final MISIM waveguide gap width was kept close to 200 nm.

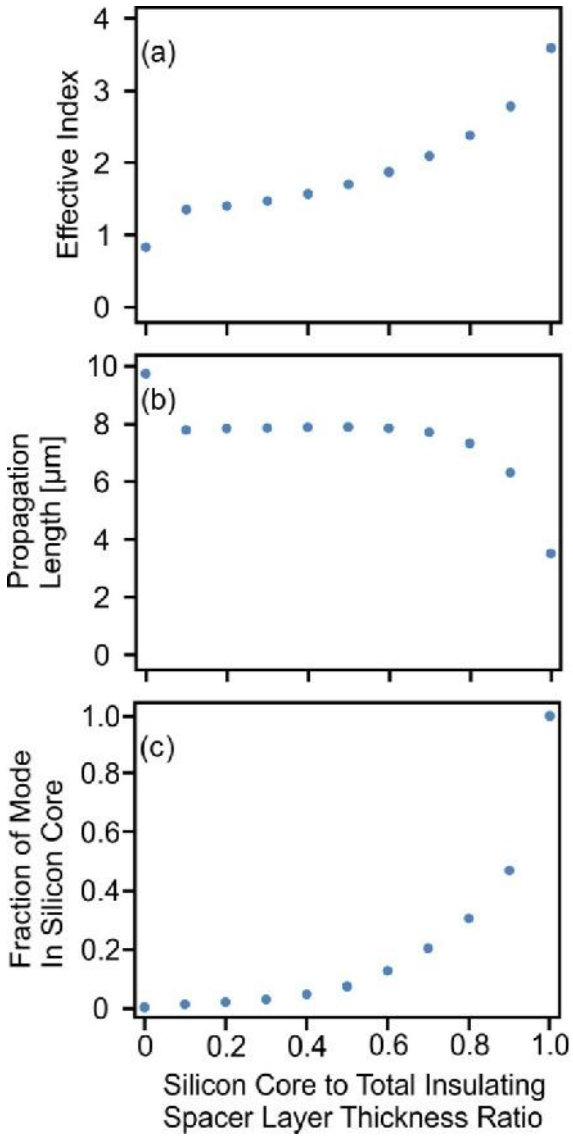

Figure 3.1: The effect of varying the semiconductor core width to total spacer layer thickness ratio for a fixed 200 nm gap $Au/SiO_2/Si/SiO_2/Au$ MISIM waveguide on the (a) effective mode index, (b) the propagation length, and (c) the fraction of the mode in the Si core at 1.55 µm as calculated with Lumerical using refractive index data from [12,17].

Once the total gap width was determined, it was important, especially for future nonlinear device applications and active modulation, to find the optimum ratio of the semiconductor core width to the total thickness of the insulator spacer layers that separate the semiconductor core from the metallic sidewalls. Figure 3.1 depicts, for a 200 nm wide Au/SiO_2/Si/SiO_2/Si MISIM nanoplasmonic waveguide, how for the fundamental transverse electric (TE) mode as the ratio of the Si core width to the total insulating spacer layer thickness decreases the effective mode index decreases (Figure. 3.1 (a)), the propagation length increases (Figure 3.1 (b)), and the mode is squeezed into the spacer layers and out of the Si core (Figure 3.1 (c)). For Si based nonlinear applications, it is important that as much of the mode as possible propagate in the Si core while at the same time maximizing the propagation length of the mode. Figure 3.1 (b) shows that the propagation length reaches a plateau for core width to total spacer thickness ratios between 0.1 and 0.75, while ~25% of the mode still resides in the Si core at a ratio of 0.75, as shown in Figure 3.1 (c). As such, the fabricated total spacer layer thickness was kept to 25% of the total gap width.

In order to characterize the MISIM nanoplasmonic waveguides, an optical signal must be coupled into and out of the MISIM waveguides. This is easily accomplished through the use of photonic coupling waveguides. The optical signal, a tunable continuous wave (CW) laser from 1.51 µm to 1.58 µm, can be coupled from lensed optical fibers to the 2 µm wide photonic coupling waveguides and vice versa. The large width of the coupling waveguide (2 µm as compared to the 500 nm commonly used in Si photonics) makes for ease of

alignment with the optical fibers. The photonic waveguides taper linearly over a 4 μm length from 2 μm wide to the 200 nm wide plasmonic waveguides. The MISIM metal cladding begins at a taper width of 500nm, as it would if the common 500nm wide Si photonic waveguide had been used. Such a taper design couples the signal directly from the fundamental TE photonic mode to the fundamental TE plasmonic mode with coupling efficiencies, *T*, as high as 85% for a Au/SiO_2(25nm)/Si(150nm)/SiO_2(25nm)/Au MISIM waveguide according to the FDTD simulations. In the TE polarization the electric field is polarized perpendicular to the metallic sidewalls. Schematic representations of the MISIM waveguides and the coupling taper can be seen in Figure 3.2 along with the electric field intensity distribution for the fundamental TE mode.

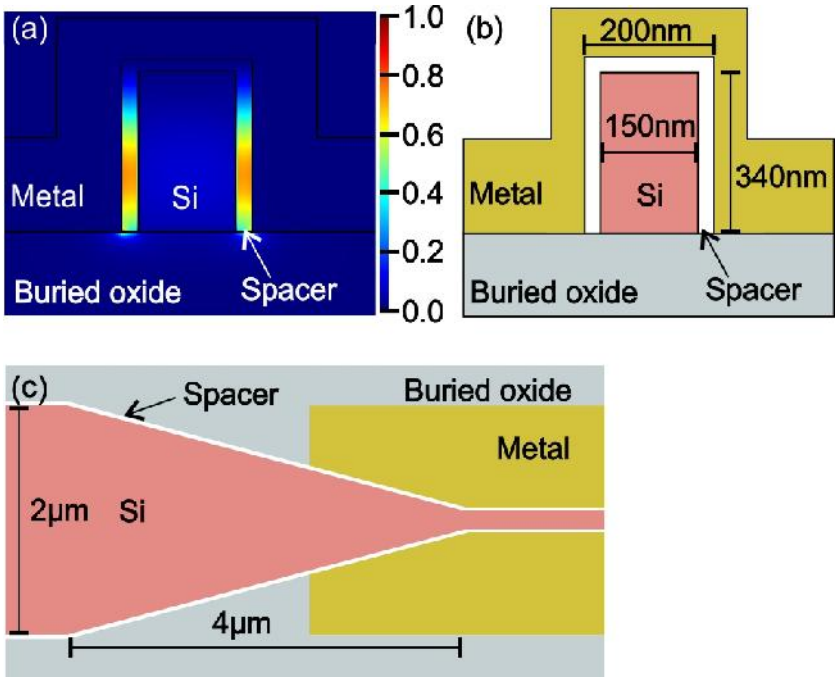

Figure 3.2: (a) Electric field intensity mode profile and (b,c) cross-sectional views of an Au/SiO_2(25nm)/Si(150nm)/SiO_2(25nm)/Au MISIM waveguide and corresponding taper.

The high losses of MISIM waveguides means that for non-linear switching and modulation applications, resonant devices are required to concentrate the fields in order to reduce the overall device size. Ring resonators are a practical example of a resonant device commonly used in conventional integrated Si photonics [18] that can be easily formed from the designed MISIM waveguides. Due to the low field penetration into the metal in MISIM waveguides, it is more practical to use aperture rather than evanescent coupling to the ring from a bus waveguide.

Due to the sensitivity of the resonant characteristics of ring resonator devices to the final fabricated ring dimensions [18], without the incorporation of individual ring resonator tuning capabilities it is very difficult to determine whether the resonance of a particular fabricated MISIM nanoring will fall within the 1.51 µm to 1.58 µm range the experimental setup can monitor. To overcome this, MISIM nanoring resonators were fabricated with a range of nanoring radii from 430 nm to 1.1 µm. With the decay length of an optical field at the telecommunications wavelengths into a metal around 20 nm, the evanescent coupling used for photonic microrings is unpractical for MISIM nanorings. Aperture coupling, the inclusion of a small gap in the metallic sidewall between the plasmonic bus waveguide and the nanoring, was used to couple to the nanorings. The FDTD simulations showed efficient coupling for a 300 nm wide aperture with 100 nm separation between bus waveguide and nanoring. For a 450 nm radii Au/SiO_2(25nm)/Si(150nm)/SiO_2(25nm)/Au MISIM nanoring, this resulted in a resonance at 1.543 µm with a quality (Q) factor of 36.7.

3.3 Fabrication of MISIM Waveguides and Ring Resonators

Fabrication of the MISIM nanoplasmonic waveguides and ring resonator devices was conducted primarily at the University of Alberta Nanofab, with atomic layer deposition (ALD) of conformal thin films performed by Amir Ashfar at Prof. K. Cadien's Nanofabrication Group at the University of Alberta. The Nanofab is a state of the art micro and nanofabrication facility containing a class 10 clean room, an extensive collection of fabrication equipment, and knowledgeable support staff. A process flow for the fabrication of the MISIM nanoplasmonic waveguides is depicted in Figure 3.3.

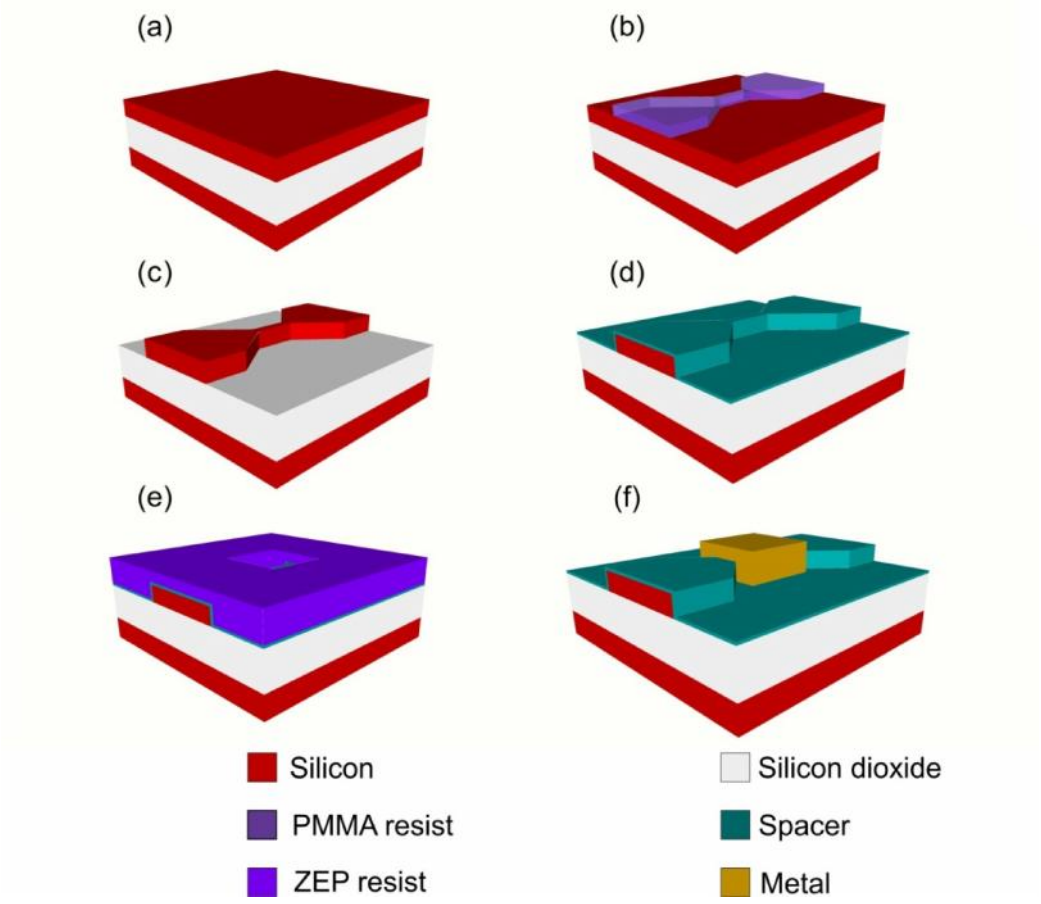

Figure 3.3: Step by step schematic of the MISIM waveguide fabrication process (dimensions not to scale). (a) SOI chip. (b) First EBL step to pattern PMMA to define underlying photonic features. (c) ICPRIE to transfer pattern through Si device layer. (d) Deposition of spacer layer. (e) Second EBL step to pattern ZEP to define metallic features. (f) Metal deposition and liftoff.

The MISIM nanoplasmonic waveguides and ring resonators were fabricated on a commercially available 10 cm diameter silicon-on-insulator (SOI) wafer consisting of a 340 nm Si device layer and 1 µm buried oxide layer diced into 1 cm by 1 cm chips through the use of a Dicing Saw. The chips were first cleaned by removing any organic residue with a Piranha cleaning process. Piranha is a 3:1

mixture of 96% sulfuric acid, H_2SO_4, and 30% hydrogen peroxide, H_2O_2. The Si features and photonic coupling waveguides were defined using electron beam lithography (EBL) and inductively coupled plasma reactive ion etching (ICPRIE). A PMMA 950 A2 positive resist spun on a cleaned SOI wafer at 4000 RPM for 40 s and baked for 15 minutes at 180 ºC to evaporate the solvent formed a 90 nm etch mask. A Filmetrics thickness mapping system was used to monitor the thickness of the resist after baking and other thin films after deposition to ensure their thicknesses remained consistent between subsequent rounds of fabrication. The features were defined using a Raith 150-2 EBL tool at 10 kV accelerating

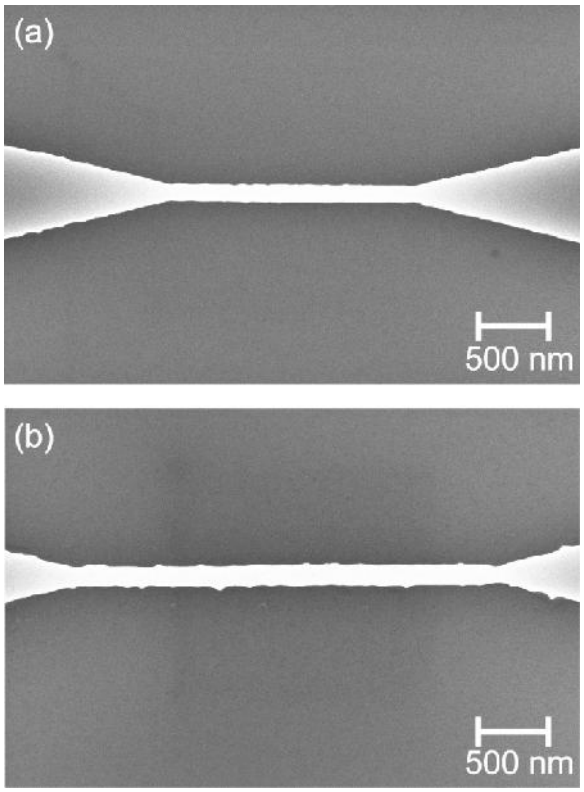

Figure 3.4: SEM images showing the comparison of waveguide roughness after ICPRIE from using different PMMA developers. (a) IPA:water 7:3. (b) MIBK:IPA 1:3.

voltage and 20 μm aperture with the dosage set to 93.5 μC/cm2 and developed for 20 s in a 7:3 mixture of IPA:water and rinsed with IPA. Notably, the specific use of 7:3 IPA:water mixture ratio for PMMA development was discovered to result in a considerable reduction of line edge roughness (LER) of the devices compared to the standard 1:3 methyl isobutyl ketone:isopropyl alcohol (MIBK:IPA) developer. A development test, with waveguides after ICPRIE depicted in Figure 3.4, shows the difference using the two different developers had on LER on identical chips from the same sample set. The 340 nm Si device layer was etched through in 27s using an ICPRIE system from Oxford. In order to etch the sample in the ICPRIE system, the sample was first mounted to a dummy coin rolled Si wafer using the adhesive Crystalbond. A drop of Crystalbond is melted onto the dummy wafer at 115 ºC and the sample is attached to the dummy wafer. After etching, the sample is released from the dummy wafer by a bath in boiling water. The remaining resist mask was removed using acetone and any lingering organic residue was stripped using piranha cleaning. Examples of several devices at this stage can be seen in Figure 3.5.

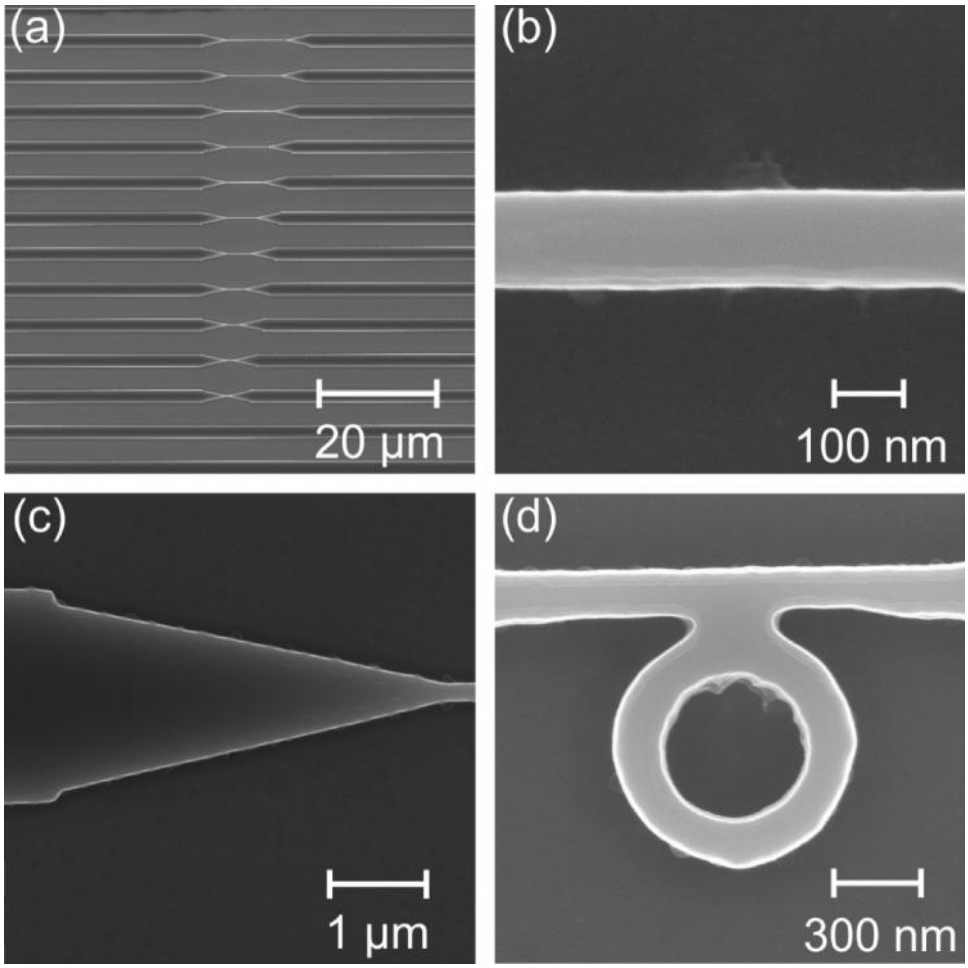

Figure 3.5: SEM images of various patterns after ICPRIE etching. (a) Set of waveguides with lengths varying from 0 µm to 10 µm. (b) Close up on waveguide. (c) Taper. (d) 450 nm radii nanoring with 300 nm wide coupling aperture.

After patterning the Si features, the insulating spacer layers were grown. The HfO_2 spacer layers were consistently grown to 20 nm over 107 cycles in an ALD system and measured with an in-situ spectroscopic ellipsometer. The deposition was conducted at 300 ºC using tetrakis(dimethylamino)hafnium (TDMAH) and plasma (600W) O_2 as precursors in a Ar carrier gas at 1 mTorr. The ALD films are almost perfectly conformal and cover the devices uniformly. The 26 nm SiO_2

spacer layers were grown using wet thermal oxidization in a tube furnace attached to a bubbler at 900 ºC for 3.5. Unlike ALD, thermal oxidization does not maintain the exact dimensions of the underlying Si structures as for every 2.27 nm of SiO_2 grown, 1 nm of Si is consumed.

To pattern the metal layers, a ZEP-520A positive resist was spun at 2000 RPM for 40s and baked for 10 minutes at 170ºC to form a 600nm layer. For lift-off processes, it is common practice for the resist to be at least three times the thickness of the deposited metal. Since sputtered metals deposit approximately one quarter to one half of their total thickness on sidewalls, the metal films were all set to 200 nm thick to ensure optically thick sidewalls. The metallization regions were aligned to the previous patterning step and exposed in a Raith 150-2 EBL tool at 30 kV accelerating voltage and 30 µm aperture with the dosage set to 300 $\mu C/cm^2$ and developed for 60 s in ZED-N50 developer followed by 30 s in 1:3 MIBK:IPA and rinsed with IPA. Due to the blanket deposition of the metal layers, the 25 nm precision of the Raith 150-2 EBL system was not a concern at this step. For the Au clad MISIM waveguides, Cr adhesion layers of up to 5 nm were used to ensure successful liftoff. After sputter deposition of the metal layers in a 7 mTorr Ar plasma at 300 W for Ag, Cr, and Cu and 80 W for Au, lift-off was performed by immersing the sample in dimethylacetamide (DMAC) and subjecting it to gentle ultrasonic vibrations to strip the resist and unwanted metal. Examples of several devices at this stage are presented in Figure 3.6. Immediately after lift-off, a final 600 nm ZEP cladding layer was spun on the samples to

prevent any oxidization of the metal cladding. Finally, the samples were cleaved to expose the end facets of the coupling photonic waveguides.

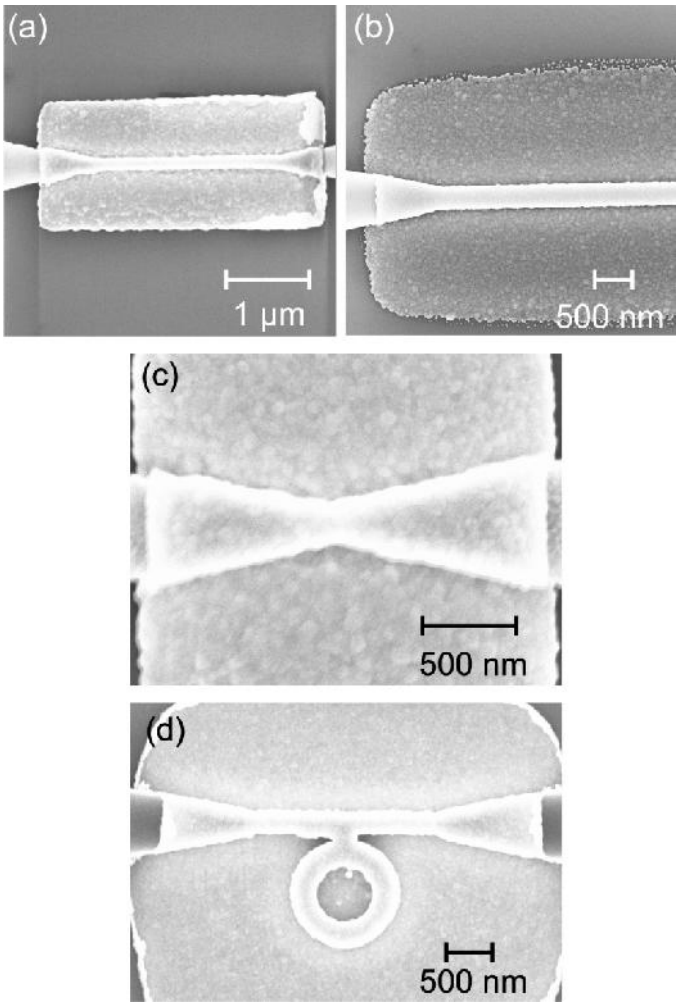

Figure 3.6: SEM images of various patterns after metal deposition and liftoff. (a) Waveguide after Au deposition. (b) Waveguide after Ag deposition. (c) Coupler to coupler device after Cu deposition. (d) 450 nm radii nanoring with 300 nm coupling aperture nanoring after Au deposition.

3.4 Experimental Results

After fabrication, the MISIM nanoplasmonic waveguides and nanoring resonators were characterized with an experimental setup located in the Ultrafast Optics and Nanophotonics Laboratory (UONL) at the University of Alberta, a full description of which can be found in Chapter 2. To probe the MISIM nanoplasmonic waveguides and nanoring resonators, a TE polarized CW optical signal from 1.51 µm to 1.58 µm was end-fire coupled from a lensed optical fiber to the input photonic waveguide and extracted from the output photonic waveguide after the nanoplasmonic device with another lensed optical fiber. The output optical fiber was attached to a detector to monitor the power transmitted through the nanoplasmonic device.

Table 3.1: Realized propagation length and coupling efficiencies for Si MISIM nanoplasmonic waveguides

Core Width [nm]	Spacer (Width [nm])	Metal Cladding (Adhesion)	L_p [µm] Experimental (Theoretical)	T [%] Experimental (Theoretical)
135	HfO_2 (20)	Au (5nm Cr)	2.11 (2.55)	44 (59)
135	SiO_2 (26)	Au (5nm Cr)	4.74 (4.01)	58 (64)
135	SiO_2 (26)	Au (3nm Cr)	5.11 (4.56)	60 (68)
135	SiO_2 (26)	Au	7.25 (7.94)	83 (77)
169	HfO_2 (20)	Cu	2.58 (4.69)	52 (65)
145	SiO_2 (26)	Cu	3.58 (5.66)	43 (67)
145	HfO_2 (20)	Ag	5.71 (19.6)	45 (73)
145	SiO_2 (26)	Ag	9.17 (27.7)	60 (78)

After measuring the power transmitted through the Si photonic waveguide and MISIM waveguides of various lengths ranging from 0 µm (just the coupling tapers) to 10 µm in 1 µm increments, an exponential fit to the data was used to extract the propagation lengths and coupling efficiencies of the various plasmonic material combinations. Not every nanoplasmonic waveguide was used to determine the exponential fit to the data. As the experimental results are extremely dependent on the coupling between the optical fibers and the coupling photonic waveguides, any damage to the coupling photonic waveguides' cleaved end facets can cause a severe reduction in transmission. Where possible, the transmission through these damaged waveguides was removed from the exponential fitting. Table 3.1 presents the experimental results and theoretical predications for the propagation lengths and coupling efficiencies per taper by the FDTD simulations using refractive index data from [12,16,17] along with the Si core width and dielectric spacer material and thickness. A comparison of the experimental results with the theoretical curves is depicted in Figure 3.7. All of the MISIM waveguides were found to have efficient coupling, with coupling efficiencies varying from 43% for the Cu/SiO_2 MISIM waveguides to 83% for Au/SiO_2 MISIM waveguides (i.e. -3.67 to -0.81 dB per taper). In general, the coupling efficiency increased with increased propagation length.

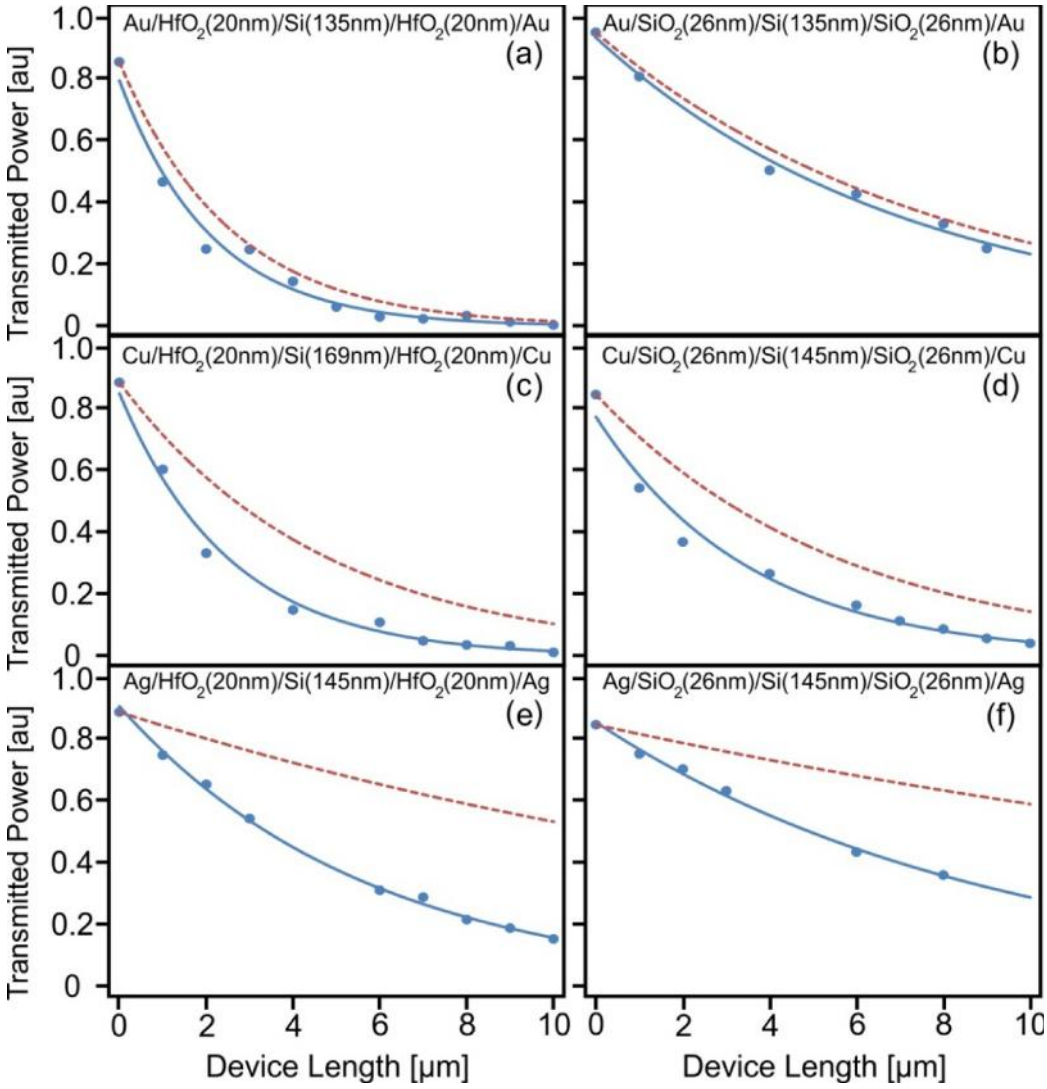

Figure 3.7: Normalized power transmitted by the (a) Au/HfO_2, (b) Au/SiO_2, (c) Cu/HfO_2, (d) Cu/SiO_2, (e) Ag/HfO_2, and (f) Ag/SiO_2 MISIM Si nanoplasmonic waveguides. The experimental results are depicted by the blue dots and fitted to an exponential blue solid lines and the theoretical predictions, calculated with Lumerical using refractive index data from [12,16,17], are represented by the red dashed lines.

The experimental data for the Au clad MISIM waveguides with HfO_2 and SiO_2 spacer layers are depicted in Figures 3.7 (a) and 3.7 (b) respectively. Commonly,

Au requires an adhesion layer of Cr or Ti when doing liftoff patterning on Si or oxides. This is a downside of using Au for nanoplasmonic waveguiding applications as both Cr and Ti are very lossy at 1.55 µm, and most of the field in the metal cladding is limited to the adhesion layer. The adhesion layer also adds another interface whose quality may be a concern. However, it was found that that an adhesion layer was not required for good contact between the Au cladding and the SiO_2 spacer layers. Figure 3.8 depicts the effect of using a Cr adhesion layer for the Au/SiO_2/Si/SiO_2/Au waveguides. As illustrated, the propagation length increased from 4.74 µm to 7.25 µm as the adhesion layer was decreased from 5 nm to 0 nm. However, an adhesion layer was still required for the Au/HfO_2/Si/HfO_2/Au waveguides, leading to their lower propagation length of 2.11 µm. In all cases, the experimental propagation lengths for the Au clad MISIM waveguides most closely matched the theoretical results, with the

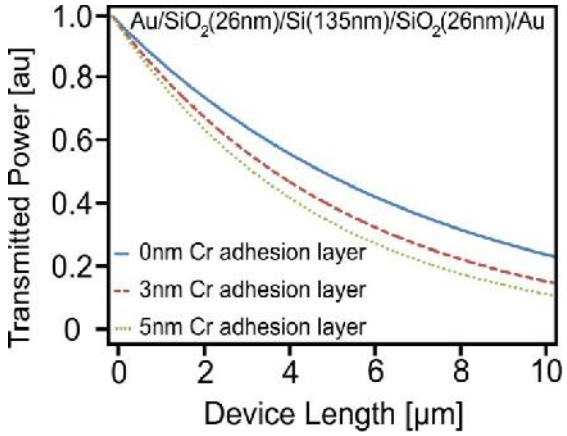

Figure 3.8: Normalized experimental transmitted power for Au/SiO_2 waveguides with no Cr adhesion layer (blue solid line), 3 nm Cr adhesion layer (red dashed line), and 5 nm Cr adhesion layer (green dotted line).

Au/SiO_2 MISIM waveguides without Cr being within 9% of their predicted value. To match the theoretical values for both propagation length and taper coupling efficiency of the Au clad MISIM waveguides to the experimental values, a complex refractive index $\tilde{n}$=0.56+i10.7 at 1.55 µm should be used instead of $\tilde{n}$=0.52+i10.72 from [12] for modeling applications. The Au/HfO_2 MISIM nanoplasmonic waveguides were used to determine the effect of waveguide LER on the propagation length of the waveguides. LER is a consequence of high resolution lithographic techniques. Since for EBL each sample must be exposed separately, changes in the focus and stigmation in the electron lens from chip to chip can cause variations in LER within the same sample set. In addition, variations in the ICPRIE processing conditions can cause LER to differ between sample sets. Figure 3.9 depicts two waveguides from different chips within the same sample set. One chip had a LER of 7 nm (Figure 3.9 (a)) whereas the other had a LER of 13 nm (Figure 3.9 (b)). The increase in LER caused the propagation length of the Au/HfO_2 MISIM nanoplasmonic waveguides to decrease from 2.11 µm to 1.18 µm. The normalized experimental transmitted power, along with an exponential fit to the data, can be seen in Figure 3.9 (c).

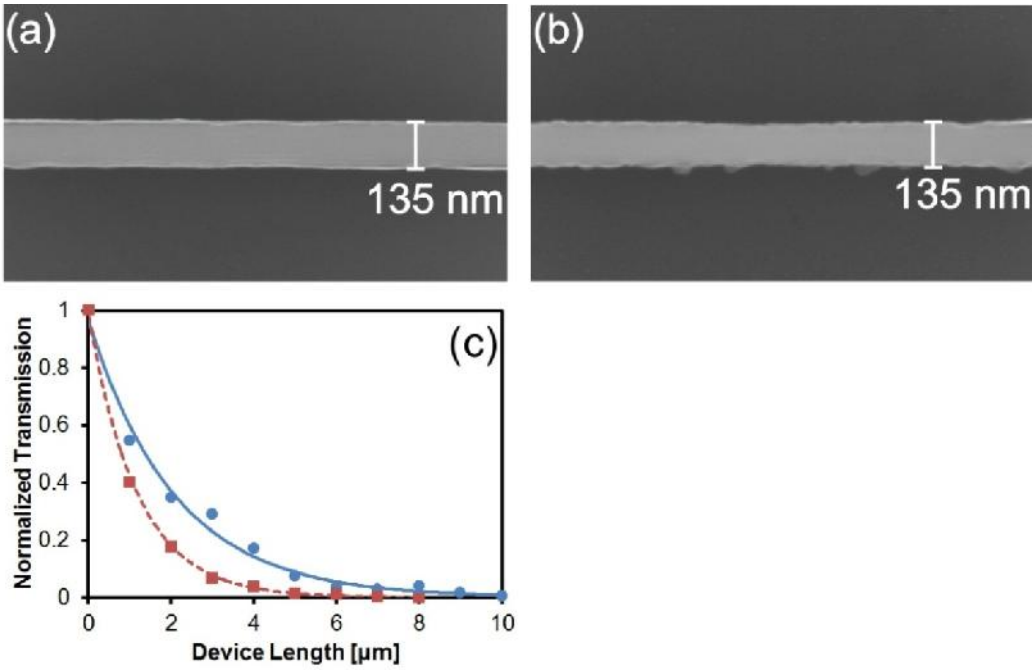

Figure 3.9: Effect of waveguide LER on propagation length for Au/HfO_2/Si/HfO_2/Au waveguides with 20 nm HfO_2 spacer layers as compared with waveguides from two different chips from the same sample set. (a) Waveguide LER= 7 nm. (b) Waveguide LER=13 nm. (c) Normalized experimental transmitted power with the chip with smooth edges shown with blue dots (fitted to an exponential blue solid line) and the chip with rough edges shown with red squares (fitted to an exponential red dashed line).

As seen in Table 3.1 and Figures 3.7 (c,d), the Cu clad MISIM waveguides had twice the propagation losses of the Au clad MISIM waveguides when no other metals, such as diffusion barriers or adhesion layers, were included. From the differences between the predicted and realized propagation length and coupling efficiency for the Cu clad MISIM waveguides, devices based on Cu clad MISIM waveguides would be better modeled using $\tilde{n}$=0.94+i10.4 at 1.55µm rather than $\tilde{n}$=0.71+i10.58 from [12]. Since the Cu clad MISIM waveguides exhibit even higher losses than predicted using material data from [12], it is unlikely that the

material data for Cu from [15] should be used in modeling Cu based nanostructures or fitting to their results.

Unlike the Au clad MISIM waveguides, the experimental transmitted power and propagation lengths of the Ag MISIM waveguides, seen in Figure 3.7 (e,f) and in Table 3.1, were only ~33% of the calculated theoretical values. This is because the calculated values assume a perfect interface and a perfectly contiguous and continuous metal film, but the sputtered Ag films were observed to be formed of many small domains, on the order of 25 to 50nm, whereas the Au and Cu films appeared to be more continuous. The effect of these many small domains was to add additional losses through the roughness at the domain edges. Examples of the Ag as compared to Au and Cu films can be seen in Figure 3.6. The Ag clad MISIM waveguides and coupling tapers can be modeled more accurately at 1.55µm using $\tilde{n}$=0.44+i11 than $\tilde{n}$=0.166+i11.27 obtained from [12].

As expected, due to its lower dielectric constant, the MISIM waveguides with thermally grown SiO_2 had propagation lengths 1.4 to 2.2 times longer than those with ALD grown HfO_2. The advantage of HfO_2 will always be that, due to its high dielectric constant, it confines more of the mode to the Si core for nonlinear applications. However, it was found that the experimental propagation lengths of the MISIM waveguides with thermally grown SiO2 were also slightly closer matched to their theoretical predications than those with ALD grown HfO_2. This is because the thermal growth of SiO_2 creates a cleaner interface between the semiconductor and the dielectric than ALD.

Since the first step towards creating an efficient all-optical modulation device is the development of a resonant structure, each sample containing the straight MISIM nanoplasmonic waveguides also contained MISIM nanoring resonators of radii 430-590 nm in 20 nm increments and 900-1100 nm in 100 nm increments coupled to bus MISIM by 300 nm wide and 100 nm deep coupling apertures. Unfortunately, no significant resonances were observed on any of the samples. The transmitted signal through each nanoring was dominated by Fabry-Perot resonances due to reflections from both the end facets of the photonic coupling waveguides and the plasmonic coupling tapers. An example of the measured and predicted transmission spectra for Au/SiO_2 (26nm)/Si(135nm)/SiO_2(26nm)/Au MISIM nanorings without Cr adhesion layers with 450 nm and 1 μm ring radii can be seen in Figure 3.10. The lack of significant resonances is attributed to the low propagation lengths of the waveguides with respect to the cirumference of the nanoring resonators.

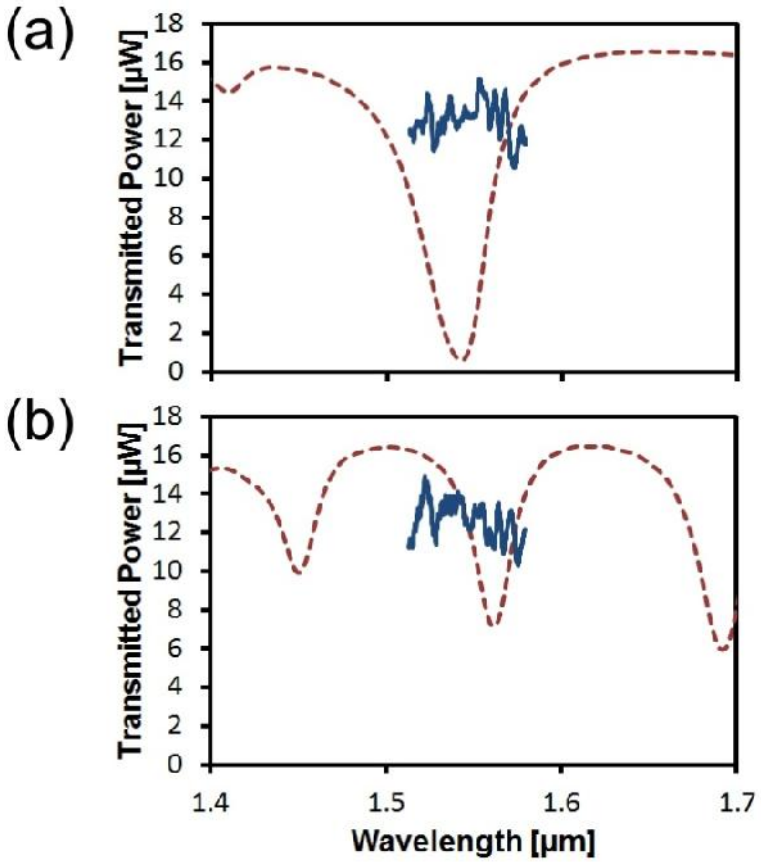

Figure 3.10: Experimental broadband transmission (blue solid line) compared to experimentally normalized FDTD simulations using Lumerical (red dashed line) for Au/SiO_2/(26nm)/Si(135nm)/SiO_2(26nm)/Au nanorings without Cr adhesion layers and with 300 nm wide and 100 nm tall coupling apertures with (a) 450 nm ring radii and (b) 1 μm ring radii.

3.5 Conclusion

From the experimental results, Au without an adhesion layer and SiO_2 are the best candidates for the metal cladding and insulating spacer layer material respectively for MISIM waveguides with Si cores. The Au/SiO_2(26nm)/Si(135nm)/SiO_2(26nm)/Au waveguide was found to have the

second longest propagation length at 7.25µm and the highest coupling efficiency at 83%, which corresponds to a low coupling loss of -0.81dB per taper. Though the Ag/SiO_2(26nm)/Si(145nm)/SiO_2(26nm)/Ag waveguide had a longer propagation length of 9.17µm, this was only 33% of the predicted value compared to 91% for the Au clad waveguides. This implies that FDTD simulations of nanoplasmonics waveguide characteristics such as propagation length, coupling efficiency, and effective index using bulk material permittivity for sputtered Ag cannot be used to accurately predict the performance of Ag clad MISIM based nanoplasmonic devices, whereas the bulk material data for Au was quite accurate. Similar to the Ag clad MISIM waveguides, the experimental results for the Cu clad devices were far lossier than theoretically predicted. No significant resonances were discovered for MISIM nanorings of various sizes or material composition.

Chapter 3 References

[1] A. Dionne, H. J. Lezec, and H. A. Atwater, “Highly confined photon transport in subwavelength metallic slot waveguides,” Nano Lett. **6**, 1928-1932 (2006).

[2] P. Neutens, P. Van Dorpe, I. De Vlaminck, L. Lagae, and G. Borghs, “Electrical detection of confined gap plasmons in metal-insulator-metal waveguides,” Nat. Photonics **3**, 283-286 (2009).

[3] Z. Han, A. Y. Elezzabi, and V. Van, “Experimental realization of subwavelength plasmonic slot waveguides on a silicon platform,” Opt. Lett. **35**, 502-504 (2010).

[4] H. Choo, M. K. Kim, M. Staffaroni, T. J. Seok, J. Bokor, S. Cabrini, P. J. Schuck, M. C. Wu, and E. Yablonovitch, “Nanofocusing in a metal-insulator-metal gap plasmon waveguide with three-dimensional linear taper,” Nat. Photonics **6**, 838-844 (2012).

[5] S. Bozhevolnyi, *Plasmonic Nanoguides and Circuits* (Pan Stanford, Singapore, 2009).

[6] R. F. Oulton, V. J. Sorger, D. A. Genov, D. F. P. Pile, and X. Zhang, “A hybrid plasmonic waveguide for subwavelength confinement and long-range propagation,” Nat. Photonics **2**, 496-500 (2008).

[7] M. T. Hill, M. Marell, E. S. Leong, B. Smalbrugge, Y. Zhu, M. Sun, P. J. van Veldhoven, E. J. Geluk, F. Karouta, Y. S. Oei, R. Nöetzel, C. Z. Ning,

and M. K. Smit, “Lasing in metal-insulator-metal sub-wavelength plasmonic waveguides,” Opt. Express **17**, 11107-11112 (2009).

[8] K. Ding, Z. C. Liu, L. J. Yin, M. T. Hill, M. J. H. Marell, P. J. van Veldhoven, R. Nöetzel, and C. Z. Ning, “Room-temperature continuous wave lasing in deep-subwavelength metallic cavities under electrical injection,” Phys. Rev. B **85**, 041301 (2012).

[9] S. Zhu, T. Y. Liow, G. Q. Lo, and D. L. Kwong, “Fully complementary metal-oxide-semiconductor compatible nanoplasmonic slot waveguides for silicon electronic photonic integrated circuits,” Appl. Phys. Lett. **98**, 021107 (2011).

[10] P. West, S. Ishii, G. Naik, N. Emani, V. Shalaev, and A. Boltasseva, “Searching for better plasmonic materials,” Laser Photonics Rev. **4**, 795-808 (2010).

[11] S. Zhu, G. Q. Lo, and D. L. Kwong, “Components for silicon plasmonic nanocircuits based on horizontal Cu-SiO_2-Si-SiO_2-Cu nanoplasmonic waveguides,” Opt. Express **20**, 5867-5881 (2012).

[12] P. B. Johnson and R. W. Christy, “Optical constants of the noble metals,” Phys. Rev. B **6**, 4370-4379 (1972).

[13] L. Chen, J. Shakya, and M. Lipson, “Subwavelength confinement in an integrated metal slot waveguide on silicon,” Opt. Lett. **31**, 2133-2135 (2006).

[14] L. Y. M. Tobing, L. Tjahjana, and D. H. Zhang, “Demonstration of low-loss on-chip integrated plasmonic waveguide based on simple fabrication

steps on silicon-on-insulator platform," Appl. Phys. Lett. **101**, 041117 (2012).

[15] S. Roberts, "Optical Properties of *Copper,"* Phys. Rev. **118**, 1509-1518 (1960).

[16] J. D. T. Kruschwitz and W. T. Pawlewicz, "Optical and durability properties of infrared transmitting thin films," Appl. Opt. **36**, 2157-2159 (1997).

[17] E. D. Palik, *Handbook of Optical Constants of Solids*, (Academic Press, San Diego, 1998).

[18] W. Bogaerts, P. De Heyn, T. Van Vaerenbergh, K. De Vos, S. Kumar Selvaraja, T. Claes, P. Dumon, P. Bienstman, D. Van Thourhout, and R. Baets, "Silicon microring resonators," Laser Photon. Rev. **6**, 47-73 (2012).

Chapter 4

Au/SiO_2/Si MIS Waveguides and Resonators[2,3]

4.1 Background

Resonant devices form one of the key components of all-optical circuitry. In silicon photonics, integrated resonators allow for enhanced nonlinear effects, such as the Kerr nonlinearity, free-carrier absorption, plasma dispersion, two-photon absorption and thermo-optic effects, and are a prerequisite for the design of efficient modulation and switching devices due to the otherwise weakly nonlinear response of Si. The most common resonant device in Si photonics is the microring resonator [1]. Due to the low loss nature of Si photonics, quality (Q) factors of up to 10^4 have been shown in devices with device footprints, the lateral area *A* taken up by a device, as low as 9.00 μm^2 [2]. However, the Q factor decreases rapidly with reduced device ring size due increased bending losses, making nanoscale

[2] *A version of this chapter has been published. M. P. Nielsen and A. Y. Elezzabi, Appl. Phys. Lett.. **103**, 051107 (2013).*

[3] *A version of this chapter has been submitted for publication. M. P. Nielsen and A. Y. Elezzabi, Electron. Lett., ELL-2013-2209, submitted July 2, 2013.*

devices sizes impossible. In addition, slight variations in the ring dimensions, due to the vagaries of the fabrication processes, can lead to large shifts in the resonant response of the microring resonators. To overcome this, individual tuning of each microring of a chip is required [1]. Unfortunately, the inclusion of separate micro-heaters for thermal tuning of each microring leads to a vastly increased footprint for each device due to the added complexity of the required heater electrical circuitry. Recently, a new class of photonic resonant devices has been demonstrated to overcome the tradeoff between device size and Q factor that plagues microring resonators. Bragg reflector resonators based on one dimensional photonic crystal cavities with a very compact device footprint of 5.00 μm^2 have exhibited Q factors on the order of 10^5 [3] at telecommunication wavelengths. Using a figure of merit for telecommunication wavelength resonators of FM=Q/*A*, the Bragg reflector resonators show an improvement of almost two order of magnitude over conventional microring resonators. However, these resonant devices sizes are still far in excess of the nanoscale size of current CMOS electronics and interconnect, requiring the transition to silicon plasmonics in order to bring Si photonic technologies to the nanoscale.

As in Si photonics, silicon plasmonics requires the use of resonant structures for the development of all-optical modulators due to the high propagation losses. Since the propagation losses for the MISIM waveguide ring resonator structures in Chapter 3 were too high to obtain a strong resonance, a less lossy configuration is required: silicon based metal-insulator-semiconductor (MIS) waveguides. This configuration sacrifices some mode confinement for increased propagation length

compared to MISIM hybrid nanoplasmonic waveguides. Very few integrated Si-based plasmonic resonators in the telecommunications band have been experimental demonstrated, with the most impressive examples based on the hybrid MIS configuration. A 9.00 μm^2 $Cu/TiO_2/Si$ MIS waveguide ring resonator was found to have a Q factor of 140 (FM=15.6 μm^{-2}) at 1.556 µm [4]. Despite the impressive Q factor for a plasmonic device, this plasmonic waveguide ring resonator provides no reduction in device footprint compared to photonic waveguide ring resonators. Similarly to photonic waveguide ring resonators, as the device size decreases the Q factor, and FM, drop accordingly. For a 4.75 μm^2 $Cu/SiO_2/Si$ MIS waveguide ring resonator, the Q factor was measured to be only 53 (FM=11.2 μm^{-2}) at 1.56 µm [5]. Further miniaturization and improvement of Si-based plasmonic resonators is required in order for truly CMOS compatible plasmonic nanocircuity and to provide complex functionalities beyond those provided by conventional electronic devices. As in silicon photonics, the introduction of plasmonic Bragg reflector resonators is required in order to further reduce plasmonic resonator device size without sacrificing device performance.

4.2 MIS Nanoplasmonic Waveguides

4.2.1 Design of $Au/SiO_2/Si$ MIS Nanoplasmonic Waveguides

Prior to designing and fabricating Bragg reflector resonators based on the MIS hybrid nanoplasmonic waveguide configuration, the underlying MIS waveguides

must be first characterized. The properties of the MIS waveguides, propagation loss, coupling efficiency and effective index, will aid in the design of the MIS Bragg reflector resonators. Guided by the results in Chapter 3, gold and silicon dioxide were chosen for the metal and insulator portions of the Si-based MIS waveguides respectively. In addition, the 200 nm wide Au(50nm)/SiO_2(50nm)/Si(340m) MIS waveguides presented in [6] were purported to have an impressive L_p=40 μm.

The Au/SiO_2/Si MIS hybrid nanoplasmonic waveguides presented here were also fabricated on a SOI substrate containing a 340 nm device layer. The Au capping layer was set to 50 nm. Below this thickness the Au layer begins to lose its bulk properties and is no longer optically thick. On the other hand, a thickness above 50 nm creates unnecessary complications for the liftoff fabrication process. To ensure nanoscale mode confinement while maintaining a reasonable L_p, the width of the MIS waveguides was set to 200 nm. The final dimension of the MIS waveguides needs to be determined was the SiO_2 insulator layer thickness. For the design of the Bragg reflector resonators two properties are of importance: propagation length of the MIS waveguide and the change in refractive index, Δn, of the waveguide with and without the Au capping layer. The propagation length needs to be sufficiently longer than the resonator length in order to build up a strong resonance. With higher Δn with and without the Au capping layer, the Bragg reflectors comprising the resonator will have higher reflectivity and higher bandwidth [7]. Figure 4.1 depicts the results of 3-D FDTD simulations with Lumerical (see Appendix B for further details about FDTD simulations using

Lumerical) for the propagation length and Δn with and without the Au capping layer for 200 nm wide Au(50nm)/SiO_2/Si(340nm) MIS waveguides of various SiO_2 insulating layer thicknesses:

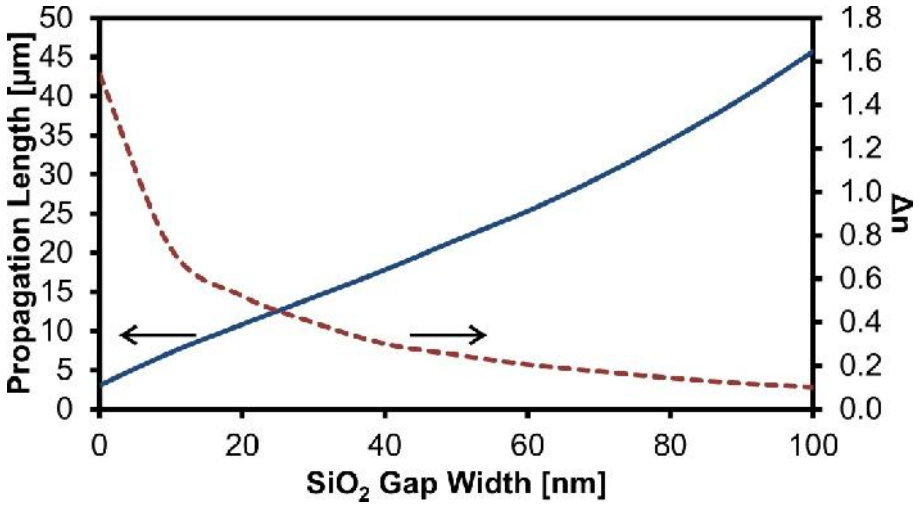

Figure 4.1: Effect of SiO_2 gap width on propagation length (blue solid line and left axis) and change in mode index with and without Au capping the waveguide (red dashed line and right axis) at 1.55 µm as calculated with Lumerical using refractive index data from [8,9] for 200 nm wide Au(50nm)/SiO_2/Si(340nm) MIS waveguides.

It is clear that the propagation length increases approximately monotonically with the increased insulating layer thickness, but at the same time Δn rapidly decreases. As previous optical Bragg reflector resonators have had device lengths around 10 µm [3], the propagation length should be kept above this value. A SiO_2 insulating layer thickness of 50 nm meets a viable middle ground with L_p=21.9 µm and Δn=0.25. A schematic representation of the resulting Au/SiO_2/Si hybrid MIS nanoplasmonic waveguide and its fundamental TM mode can be seen in Figure 4.2 (a) and (b) respectively.

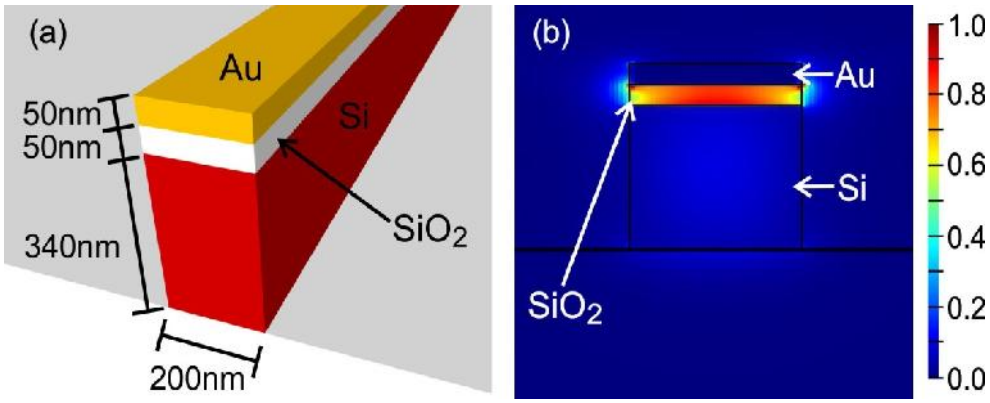

Figure 4.2: (a) Schematic representation of the Au/SiO_2/Si MIS plasmonic waveguide and (b) electric field intensity distribution of the fundamental TM mode with predicted propagation length of 21.9 µm at 1.55 µm as calculated with Lumerical using refractive index data from [8,9].

Similar to the MISIM nanoplasmonic waveguides detailed in Chapter 3, the optical signal was coupled to and from the MIS plasmonic waveguides through the use of photonic coupling waveguides. The 2 µm wide coupling SOI ridge waveguides taper over a length of 4 µm to a width of 200 nm at the plasmonic waveguides. The large width of the coupling waveguides compared to the 500 nm wide conventional SOI waveguides ensured ease of alignment with I/O optical lensed fibers. The Au capping layer began at a taper width of 500 nm as it would with the conventional SOI waveguides. This coupling scheme resulted in predicted coupling efficiencies as high as 78% for a 200 nm wide Au(50nm)/SiO_2(50nm)/Si(340nm) MIS hybrid plasmonic waveguide at λ=1.55 µm.

4.2.2 Fabrication of $Au/SiO_2/Si$ MIS Nanoplasmonic Waveguides

Fabrication of the MIS nanoplasmonic waveguides was conducted personally at the University of Alberta Nanofab. The Nanofab is a state of the art micro and nanofabrication facility containing a class 10 clean room, an extensive collection of fabrication equipment, and knowledgeable support staff. Much of the process development for the MIS nanoplasmonic waveguides was based off of the experience accrued during the fabrication of the MISIM nanoplasmonic waveguides and devices presented in Chapter 3. A process flow for the fabrication of the MIS nanoplasmonic waveguides is depicted in Figure 4.3.

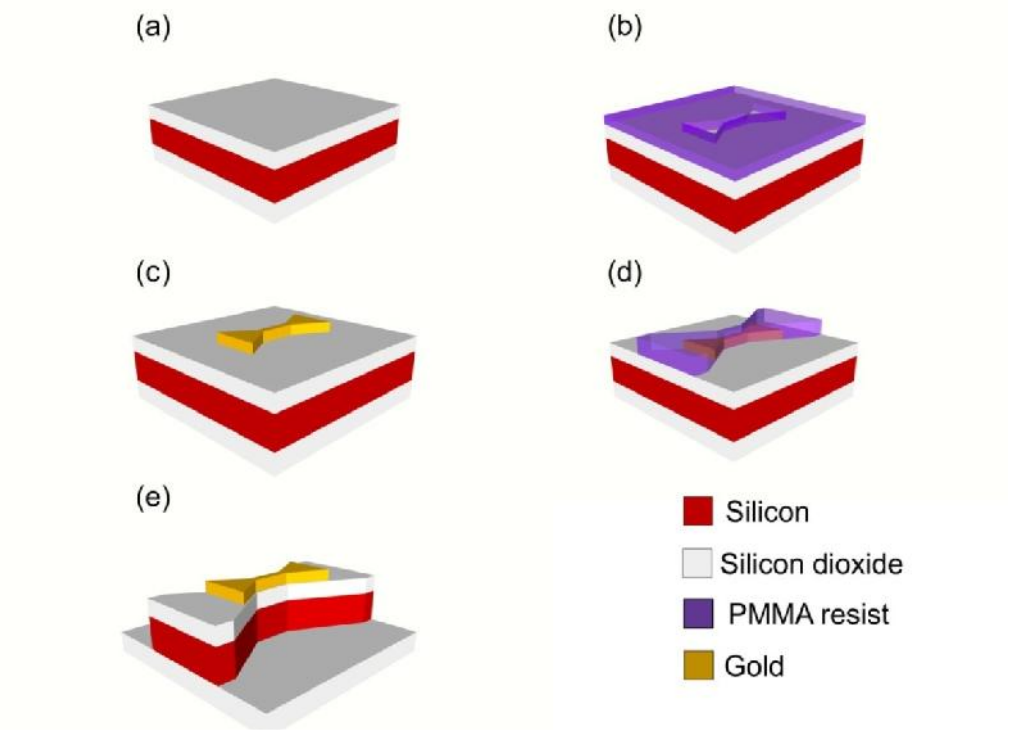

Figure 4.3: Step by step schematic of the Au/SiO_2/Si MIS waveguide fabrication process (dimensions not to scale). (a) PECVD deposition of SiO_2 onto the SOI chip. (b) First EBL step to pattern the metallic features. (c) Metal deposition and liftoff. (d) Second EBL step to define underlying photonic features. (f) SiO_2 and Si RIE to transfer pattern through the SiO_2 and Si to the buried oxide layer.

The MIS nanoplasmonic waveguides and resonators were fabricated on a commercially available 10 cm diameter SOI wafer consisting of a 340 nm Si device layer and 1 µm buried oxide layer diced into 1 cm by 1 cm chips through the use of a Dicing Saw. After removing any organic residue through the use of a Piranha process, a thin 50 nm layer of SiO_2 was deposited on the samples using 63 s of plasma enhanced chemical vapour deposition (PECVD) on a system from Trion. As in the MISIM nanoplasmonic device fabrication detailed in Chapter 2, a Filmetrics thickness mapping system was used to monitor the thickness of the

deposited thin films between subsequent fabrication runs. It was found that the thickness of the PECVD SiO_2 films varied from 45 nm to 50 nm.

Due to the nanoscale size of the metal features of the MIS nanoplasmonic devices, the metal patterning was conducted before defining the underlying SiO_2/Si features. A positive PMMA resist bilayer was first spun on the samples. The bottom layer was 70 nm of PMMA 495 A2 spun at 2000 RPM for 40 s and baked for 20 minutes at 180 ºC. Immediately afterwards, a second 90 nm resist layer of PMMA 950 A2 was spun at 4000 RPM for 40s and baked for 10 minutes at 180 ºC. Since the bottom layer of the resist bilayer is of a lower molecular weight, it develops faster than the top layer, causing an undercut which makes the liftoff of thin metal layers more feasible. The resist bilayer was then patterned in a Raith 150-2 EBL tool set at 10 kV accelerating voltage and 10 µm aperture with the dosage set to 187 $\mu C/cm^2$. The bilayer was developed for 45 s in a 1:3 MIBK:IPA mixture and rinsed with IPA. Metal deposition was performed in a sputter system in a 7 mTorr plasma at 300 W for the 5 nm Cr adhesion layer followed by 80 W for the 50 nm Au layer. Despite the findings in Chapter 2 that gold nanoplasmonic device performance is improved when an adhesion layer is not used, the nanoscale nature of the metallic features necessitated the use of a Cr adhesion layer. Liftoff was performed by subjecting the samples to gentle ultrasonic vibrations during immersion in acetone. An example of a sample at this stage is presented in Figure 4.4.

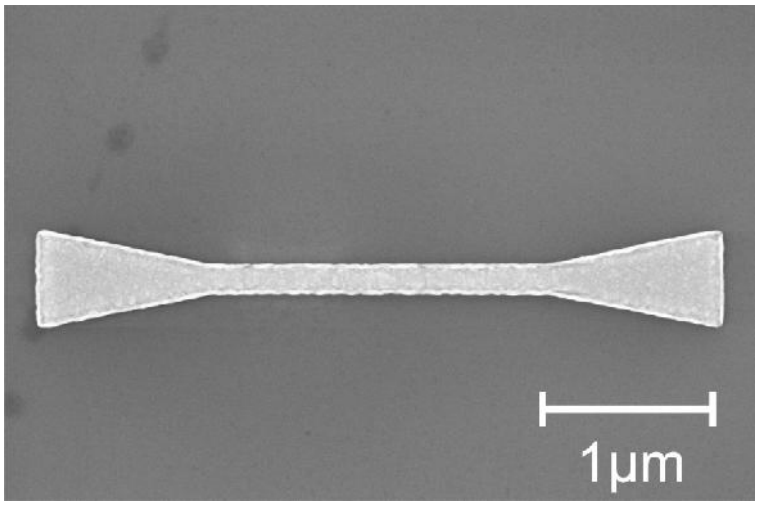

Figure 4.4: SEM image of MIS waveguide after Au deposition and liftoff.

In order to define the underlying SiO_2/Si features and photonic coupling waveguides, first 140 nm of PMMA 950 A2 was deposited by spinning at 1000 RPM for 40 s and baking for 15 minutes at 180 ºC. After bonding the sample to a dummy Si wafer using Crystalbond, the sample underwent anisotropic SiO_2 RIE in a STS system for 16 s to etch down to the Si device layer. The dummy wafer was then quickly transferred to the ICPRIE system from STS and the 340 nm Si device layer was etched through over 27 s. After etching, the sample was released from the dummy wafer by a bath in boiling water and the remaining resist mask was removed using acetone. An example of a sample at this stage is depicted in Figure 4.5. Finally, the samples were cleaved with a diamond scribe to expose the end facets of the coupling photonic waveguides.

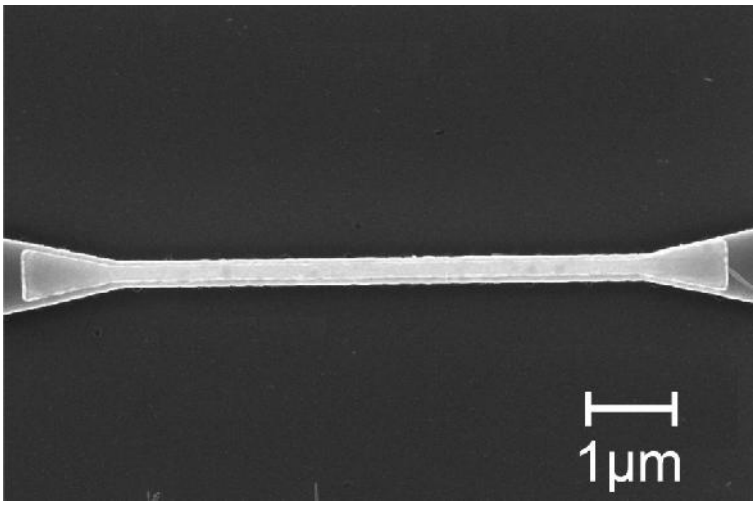

Figure 4.5: SEM image of Au/SiO_2/Si MIS waveguide after etching.

4.2.3 Experimental Results

The MIS hybrid nanoplasmonic waveguides were characterized with the experimental setup described in Chapter 2 located in the Ultrafast Optics and Nanophotonics Laboratory at the University of Alberta. A TM polarized CW optical signal from 1.51 μm to 1.58 μm was end-fire coupled from a lensed optical fiber to the cleaved end facet of the input photonic waveguide and extracted from the output photonic waveguide's cleaved end facet after the nanoplasmonic device with another lensed optical fiber. The output optical fiber was attached to a detector to monitor the power transmitted through the nanoplasmonic device.

Au/SiO_2/Si MIS waveguides of lengths of 0 μm (just the photonic-plasmonic couplers) to 20 μm in 2 μm increments were fabricated to experimentally determine L_p and the coupling efficiency. The transmitted powers at λ=1.55 μm through the waveguides of a characteristic sample are depicted in Figure 4.6 (a).

From an exponential fit to the experimental data, one can extract L_p=16.0 µm, equivalent to a propagation loss of -0.27 dB/µm. As with the MISIM waveguides, aberrant data points were removed from the fitting. Regardless, nearly identical results were obtained in all three sample sets tested. The experimental propagation length is within reasonable agreement with L_p=21.9 µm, propagation loss of -0.20 dB/µm predicted by the 3-D FDTD simulations. Furthermore, as depicted in Figure 4.6 (b), the propagation loss of the MIS waveguides does not vary much within the wavelength range 1.51-1.58 µm. The broadband nature of this class of nanoplasmonic waveguides grants it the capacity to be used as a broadband nanoplasmonic interconnects for wavelength multiplexing schemes and bodes well for their use in resonant devices such as the Bragg reflector resonators described later in this chapter.

The coupling efficiency between the I/O coupling waveguides and the MIS waveguides determines the effectiveness of integrating this class of waveguides into EPICs or even just photonic integrated circuits. The coupling efficiency, which includes the effect of the Si photonic taper design and any mode mismatch between the SOI and nanoplasmonic waveguides, at λ=1.55 µm can be acquired from the vertical intercept of the power transmission curve in Figure 4.6 (a) of 21.6 µW. By comparing this value to the transmitted power through a reference 2 µm × 340 nm SOI waveguide on the same sample of 61.2 µW, a coupling efficiency of 59.4% or -2.28 dB per interface is obtained at λ=1.55 µm. Figure 4.6 (c) depicts the coupling efficiency per interface taken from a broadband wavelength scan of just the couplers. It shows that the coupling efficiency per

interface is fairly consistent from λ=1.51-1.58 μm, though greatly affected by Fabery-Pérot resonances due to reflections from the interfaces. Unfortunately, the coupler efficiency per interface at λ=1.55 μm of 59.4% (-2.28 dB) is slightly less than the calculated value of 77.7% (-1.10 dB). The slight discrepancy between the predicted and the experimentally determined propagation length and coupling efficiency originates from three sources: the effect of the Cr adhesion layer, the alignment between EBL steps, and the metal edges that result from the lift-off process. The non-continuous and non-contiguous nature of thin metal films such as the 5 nm Cr adhesion layer introduce unavoidable losses not taken into account by the FDTD predictions which assume a continuous layer. In addition, the overlay alignment procedure for the second EBL step limits the alignment accuracy to tens of nanometers, requiring a slightly wider underlying SOI waveguide (~250nm). Any misalignment here reduces the overlap between the excitation mode from the Si photonic taper and the nanoplasmonic waveguide, thus reducing the overall coupling efficiency. Finally, as seen in Figure 4.4 and Figure 4.5, the lift-off process utilized leaves behind ‘rabbit ears’ along the edges of the metallic features. These ‘rabbit ears’ result from the use of a thin or insufficiently undercut lift-off resist layer and come from the lift-off process pulling the edges of the metal features up. Atomic force microscopy (AFM) measurements performed by Sam Maloney in the UONL determined heights up to 15 nm and widths ranging from 5-20 nm for the ‘rabbit ears’ in the MIS devices. The AFM measurements also confirmed a total Au/Cr thickness of 50nm, very close to the 55nm expected. In order to eliminate these ‘rabbit ears’ from future

devices, a lift-off process similar to the one in [10] should be adopted in order to remove this source of losses.

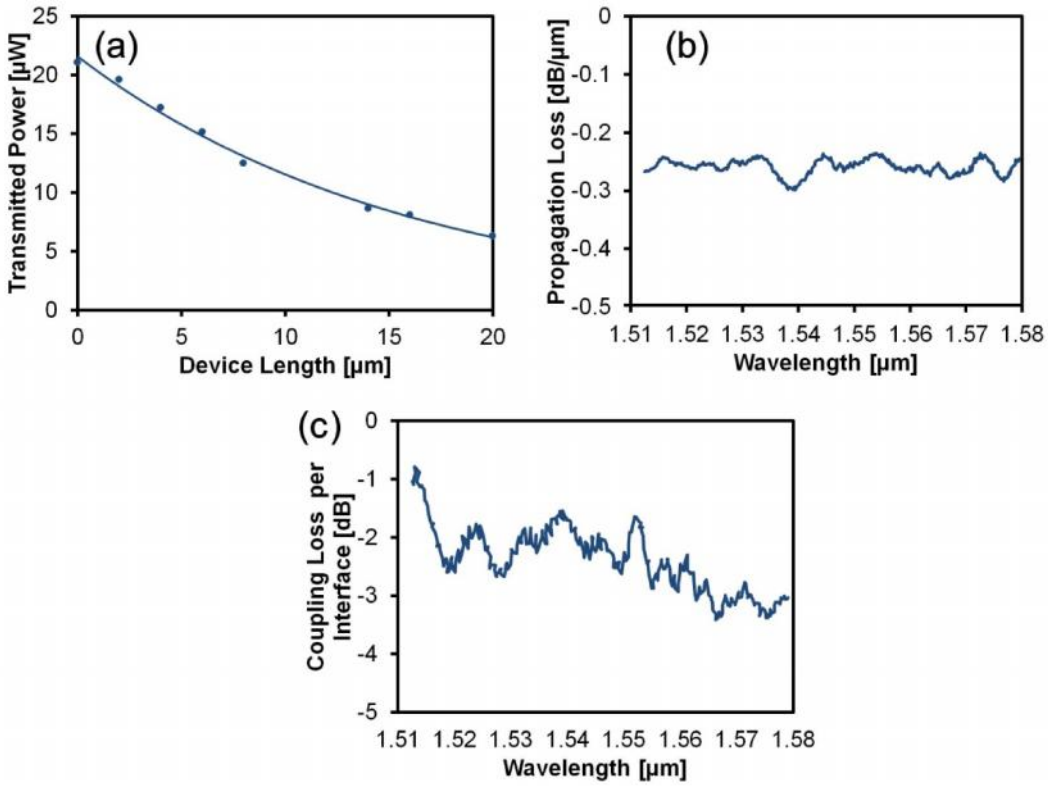

Figure 4.6: Experimental results for 200 nm Au(50nm)/SiO_2(50nm)/Si MIS waveguides. (a) Power transmitted through waveguides of lengths up to 20 µm with exponential fit showing L_p=16.0 µm. (b) Broadband propagation loss. (c) Broadband coupling loss per interface.

4.3 Bragg Reflector Resonators

4.3.1 Design of $Au/SiO_2/Si$ MIS Nanoplasmonic Bragg Reflector Resonators

With the development of the $Au/SiO_2/Si$ MIS nanoplasmonic waveguide platform, Bragg reflector resonators integrated onto the same platform could be designed. The resonators were formed by patterning the metal layer of the MIS waveguides such that rather than a continuous stripe of Au as was the case for the MIS waveguides, instead selective portions of the metal layer were removed to leave behind a series of metallic nanosegments. The result of the patterning is clarified in the schematic in Figure 4.7 (a). As illustrated by Figure 4.7 (b), each Bragg reflector resonator consists of a central cavity of length L between two Bragg reflector mirrors. The Bragg reflector mirrors are composed of 5 central metal nanosegments of length w_1 separated by gaps of length w_2, with tapers on each end of the reflectors with decreasing metal nanosegment lengths m_3, m_2, and m_1 separated by gaps of decreasing length a_3, a_2, and a_1. The role of the tapers was to adiabatically reduce the optical impedance mismatch between the Bragg reflectors and the MIS plasmonic waveguides and cavity [11]. By incorporating the experimental results for the coupling efficiency and propagation losses of the MIS nanoplasmonic waveguides into the FDTD simulations, the effective mode index for the MIS nanoplasmonic waveguides with the top Au layer, $n_{1,eff}$, and without the top Au layer, $n_{2,eff}$, were calculated to be 2.3 and 2.0

respectively. This enables the Bragg reflectors to be designed for λ_o=1.55 µm in order to satisfy the Bragg condition [12]:

$$w_1 n_{1,eff} + w_2 n_{2,eff} = a_o / 2, \tag{4.1}$$

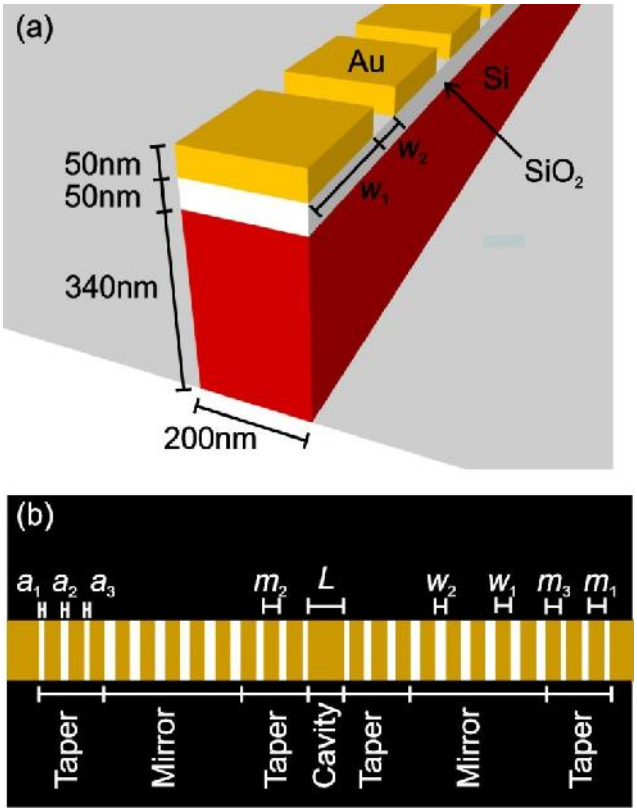

Figure 4.7: (a) Schematic representation of the Au/SiO_2/Si MIS Bragg reflector. (b) Top-down schematic representation of the Bragg reflector resonator depicting taper dimensions (a_1, a_2, a_3, m_1, m_2, and m_3), mirror dimensions (w_1 and w_2), and central cavity (L).

Four different devices satisfying Eq. 4.1 around λ_o=1.55 µm were designed, each with L=510 nm but a different ratio of w_1 to w_2 and adiabatic taper dimensions. The devices, hereafter denoted Devices 1, 2, 3 and 4, had increasing mirror Au nanosegment lengths w_1 (and correspondingly smaller gaps w_2) of 150

nm, 210 nm, 250 nm and 300 nm respectively. These Bragg reflector resonators have very compact device sizes of 1.63 μm^2, 1.61 μm^2, 1.58 μm^2 and 1.54 μm^2 for Devices 1-4, respectively. The full dimensions of each of the 200 nm wide Bragg reflector resonators can be seen in Table 4.1 below:

Table 4.1: Bragg reflector resonator cavity, mirror and taper dimensions

Device	L [nm]	w_1 [nm]	w_2 [nm]	a_1 [nm]	m_1 [nm]	a_2 [nm]	m_2 [nm]	a_3 [nm]	m_3 [nm]
1	510	150	220	130	130	160	140	170	145
2	510	210	150	100	180	120	190	125	200
3	510	250	100	65	228	80	233	85	233
4	510	300	45	30	260	35	270	40	280

Extensive FDTD simulations using real fabricated structures were used to determine the appropriate final dimensions for the Bragg reflector resonators. An example of one of the resonators, Device 3, after the liftoff fabrication process is portrayed in Figure 4.8 (a). The FDTD simulations were also used to predict the broadband spectral response of the fabricated resonators after incorporating the subtle variations in device geometry brought on by the fabrication process. These variations in device geometry include variations in individual metallic nanosegment size of up to 10 nm and the slight rounding of the corners of the nanosegments. The results of these simulations for Device 3 can be seen in Figure 4.8 (b) and (c) which depict the normalized intensity distribution at the Au/SiO_2 interface off (λ=1.51 μm) and on (λ=1.53 μm) resonance respectively.

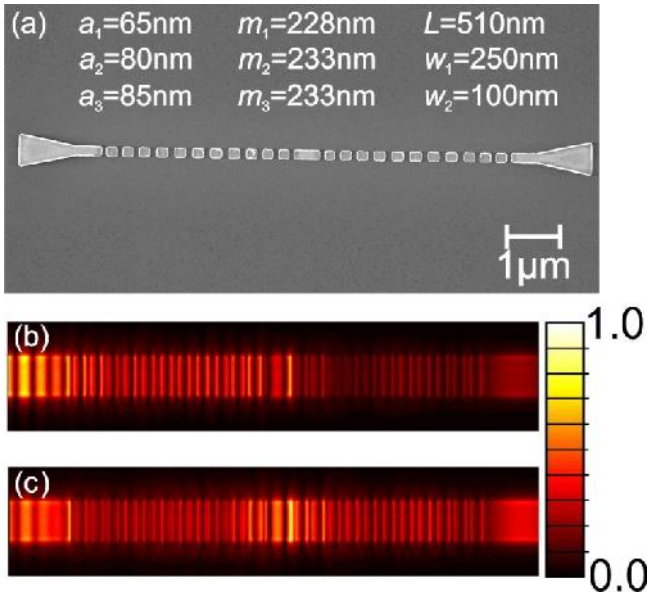

Figure 4.8: (a) SEM image of a representative resonator, Device 3, after liftoff. Normalized electric field intensity distributions of Device 3 at the Au/SiO_2 interface (b) 'off' (λ=1.51 μm) and (c) 'on' (λ=1.53 μm) resonance (dimensions not shown to scale to improve visibility).

4.3.2 Fabrication of Au/SiO_2/Si MIS Nanoplasmonic Bragg Reflector Resonators

The Au/SiO_2/Si MIS Bragg reflector resonators were fabricated using the same process developed for the Au/SiO_2/Si MIS waveguides described earlier in this chapter. The gaps were in the resonators' metal layer were formed by selectively not exposing the PMMA bilayer in those regions. Examples of the Bragg reflector resonators after lift-off and after the etching processes can be seen in Figure 4.9.

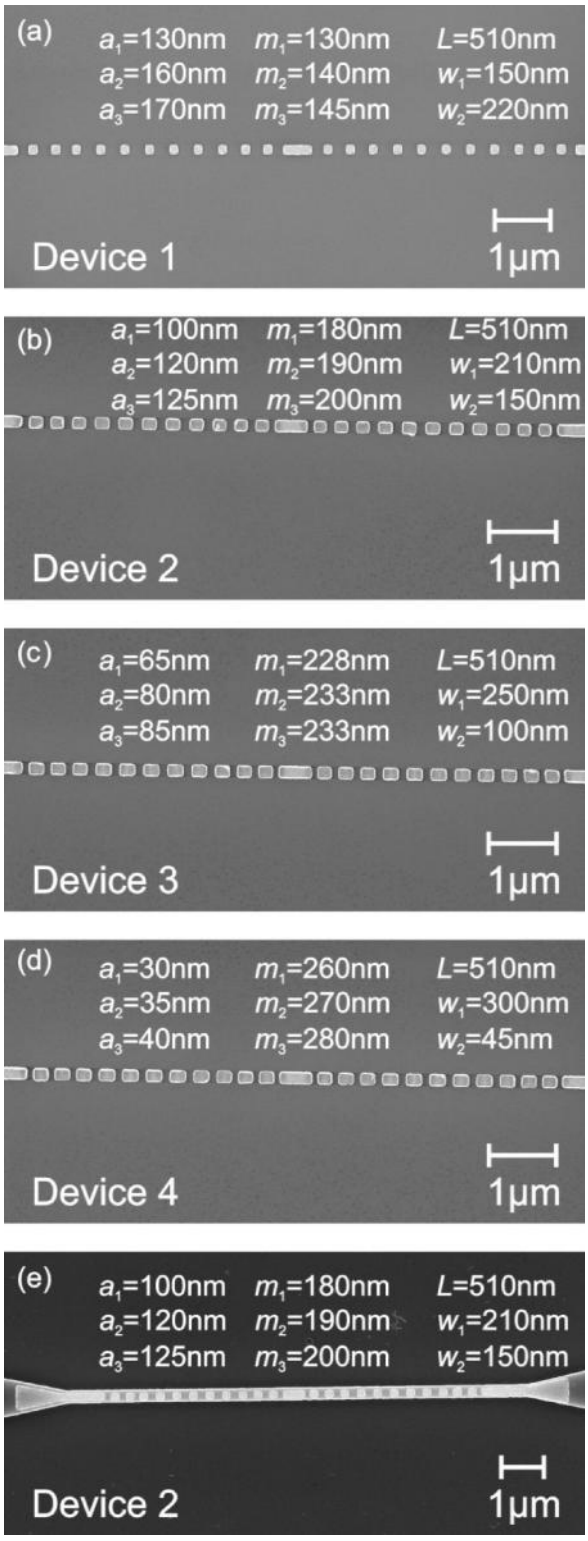

Figure 4.9: SEM images after lift-off the Bragg reflector resonators (a) Device 1, (b) Device 2, (c) Device 3, and (d) Device 4. (e) SEM image of Device 2 after etching through the device layer.

4.3.3 Experimental Results

Using the experimental setup in the UONL described in Appendix A, the broadband spectral response of the Bragg reflector resonators were determined from λ=1.51-1.58 μm. The experimental results are depicted in Figure 4.10 alongside the experimentally normalized predictions. Due to the lossy nature of plasmonic systems, the transmission characteristics of the resonators were formed of a series of overlapping resonances unlike the isolated resonances commonly found in photonic systems. As such, the Q factors of the central resonances were extracted using multi-peak Lorentzian fittings from the commercial software Origin [13], with the fittings of the central resonances depicted in Figure 4.10. Device 1 had a resonant peak at λ=1.54 μm and a measured Q factor of 32.6 compared to a predicted Q factor of 27.4. Increasing the mirror nanosegment length in Device 2 to 210 nm shifted the resonance to λ=1.53 μm and improved the Q factor to 49.4 compared to a predicted Q factor of 35.8. Continuing to increase the mirror nanosegment length to 250 nm in Device 3 again improved the Q factor, in this case to 56.7 compared to a predicted value of 45.5 without shifting the resonance peak from λ=1.53 μm. Finally, increasing the mirror nanosegment length to its maximum value of 300 nm in Device 4 obtained the highest Q factor of 64.4 compared to a predicted 76.1, while shifting the resonance peak to λ=1.545 μm. The enhancement of the Q factor found by increasing the metallic component of the mirrors and decreasing the gaps between nanosegments has an ultimate limitation in how small a nanoscale gap can be patterned using EBL and liftoff. The smallest nanoscale gap, a_1, on the Bragg

reflector taper thus determines the highest Q factor obtainable with this Bragg reflector resonator design. Beyond this, further enhancement of the Q factor of the resonators is dependent upon reducing the loss of the underlying $Au/SiO_2/Si$ MIS nanoplasmonic waveguides through optimization of the fabrication process as described in section 4.2.3. Reasonable agreement was found between the experimental results and the experimentally normalized FDTD simulation results for all four resonators. As the metal nanosegment length in the mirrors was increased, agreement between experimental and predicted results improved. The resulting figure of merits for the resonators of 20.0 μm^{-2} for Device 1, 30.6 μm^{-2} for Device 2, 35.9μm^{-2} for Device 3 and 42.9μm^{-2} for Device 4 are among the highest ever reported for demonstrated silicon plasmonic resonators.

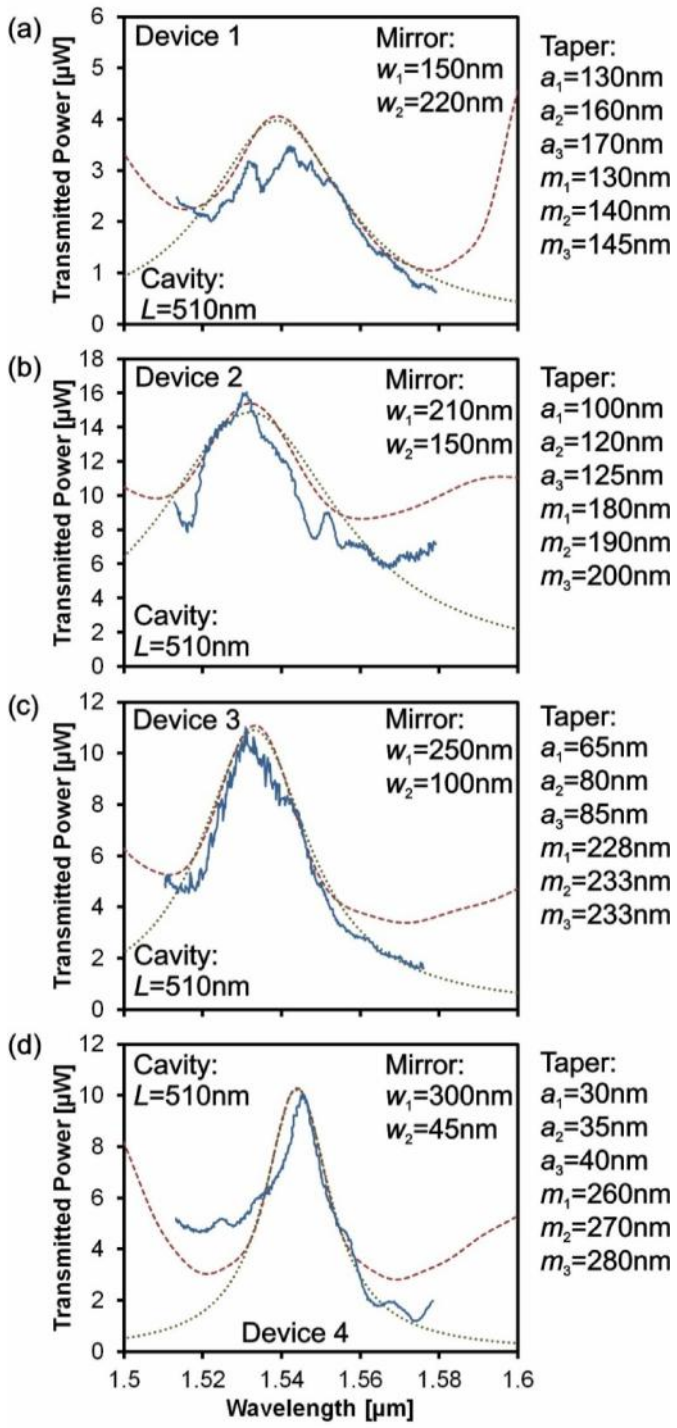

Figure 4.10: Experimental broadband transmission (blue solid line) for the Bragg reflector resonators as compared to experimentally normalized FDTD simulations (red dashed line) for (a) Device 1, (b) Device 2, (c) Device 3, and (d) Device 4. The central peaks of the FDTD simulations of the devices are fitted with a Lorentzian (green dotted line) using Origin in order to accurately calculate the Q factor.

4.4 Other Devices

4.4.1 Bragg Mirror

By changing the cavity length of the Bragg reflector resonators such that the cavity resonance no longer overlaps with the Bragg reflectors' stop-bands, the device becomes a Bragg mirror and essentially acts as a stop-band filter about λ_o. Device 5, depicted in Figure 4.11 (a), is identical to the Bragg reflector resonator Device 3 but with the central cavity length increased from 510 nm to 675 nm. The experimental transmission characteristics of Device 5 can be seen in Figure 4.11 (b) along with the predicted results. Below 1.56 μm there is good agreement between the experimental and predicted results. Unfortunately, the wavelength range of the experimental setup was not broad enough to encompass the entirety of the realized stop-band, making it impossible to assess its total width.

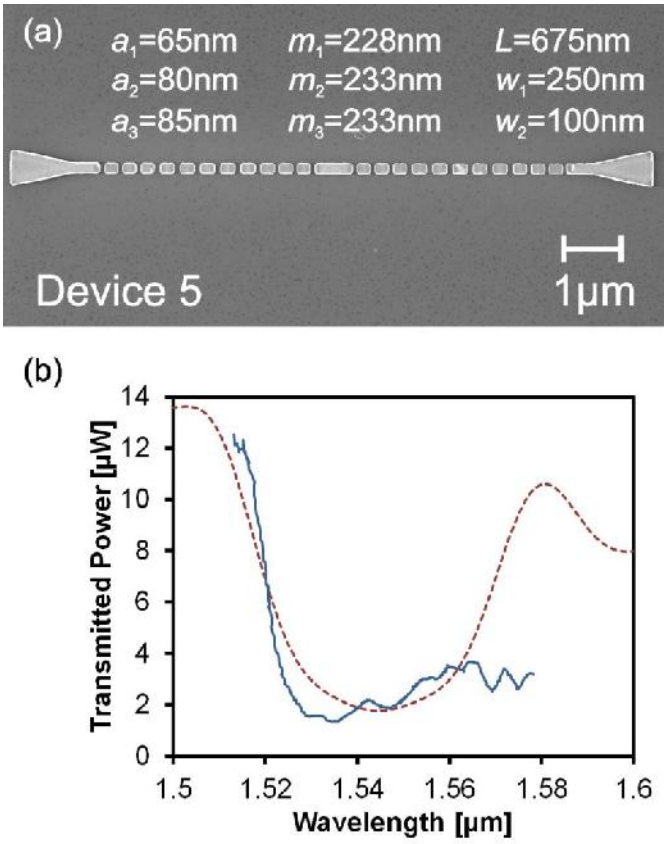

Figure 4.11: (a) SEM image after the lift-off process for Device 5. (b) Experimental broadband transmission (blue solid line) for the Bragg reflector resonators as compared to experimentally normalized FDTD simulations (red dashed line) for Device 5.

4.4.2 Waveguide Ring Resonators and Disk Resonators

While the Bragg reflector resonators were found to have impressive figure of merits and very compact device footprints, the realized Q factors were below what is possible with plasmonic waveguide ring resonators [4]. As such, the fabrication of Au/SiO_2/Si MIS nanoplasmonic waveguide ring resonators with radii from 500 nm to 3 μm in 500 nm increments was attempted. The waveguide ring resonators were coupled to 200 nm wide Au/SiO_2/Si MIS nanoplasmonic bus

waveguides by a 200 nm gap. However, the liftoff process was unsuccessful in releasing the centers of the waveguide ring resonators despite several variations on the process. An example of an unsuccessful lift off of a 1 µm radii waveguide ring resonator is depicted in Figure 4.12 (a).

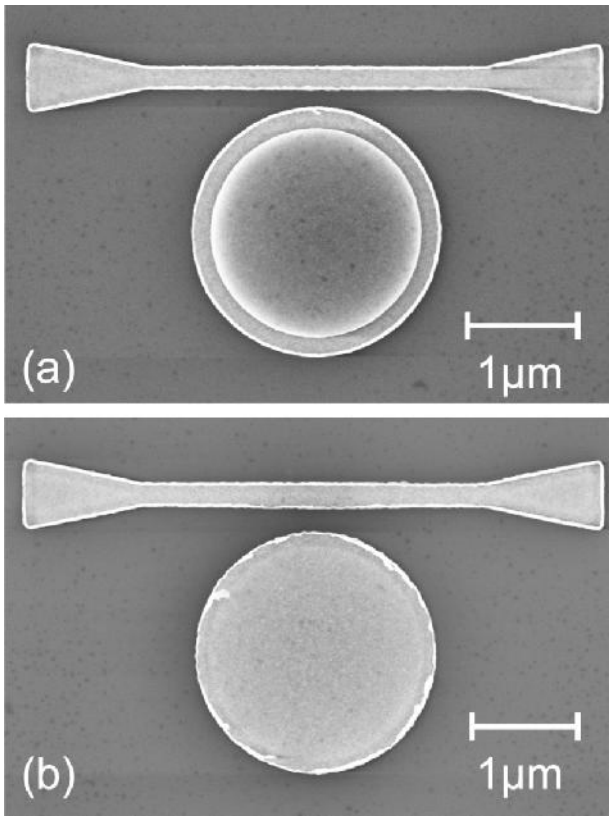

Figure 4.12: SEM image of $Au/SiO_2/Si$ MIS (a) waveguide ring resonator and (b) disk resonator with 1 µm radii after liftoff. Resonators are evanescently coupled to 200 nm wide $Au/SiO_2/Si$ MIS nanoplasmonic bus waveguides by a 200 nm gap. Liftoff of center of the waveguide ring resonators was unsuccessful.

With the failure of liftoff of the waveguide ring resonators, $Au/SiO_2/Si$ MIS nanoplasmonic disk resonators of the same dimensions were attempted. Figure 4.12 (b) illustrates the successful liftoff of a 1 µm radii disk resonator. FDTD

simulations of a 1 µm radii disk resonator showed a resonance at 1.52 µm with a Q factor of 377 (FM=94.2 μm^{-2}), higher than that found for the Bragg reflector resonators. Figure 4.13 (a) and (b) depict the normalized electric field intensity distribution for a 1 µm radii disk resonator 'on' (λ=1.52 µm) and 'off' (λ=1.55 µm) resonance, respectively. After experimentally characterizing the disk resonators, a resonance within the wavelength range of λ=1.51-1.58 µm was only found for a radii of 1 µm. The experimental results for the 1 µm radii disk resonator, alongside the predicted results, can be seen in Figure 4.13 (c). From the experimental results, a Q factor of 82.3 (FM=20.6 μm^{-2}) at λ=1.522 µm can be extracted. However, this is much lower than the Q factor of 377 predicted. This is due to the higher losses than predicted inside the disk. The 'rabbit ears' along the edge of the disk resonator, as seen in Figure 4.12 (b), increase the losses along the edge of the disk. Unfortunately, as seen in Figure 4.13 (a), at resonance the highest field intensity is found along the edge of the disk. Further optimization of the liftoff process to eliminate these 'rabbit ears' is required in order to improve the Q factor.

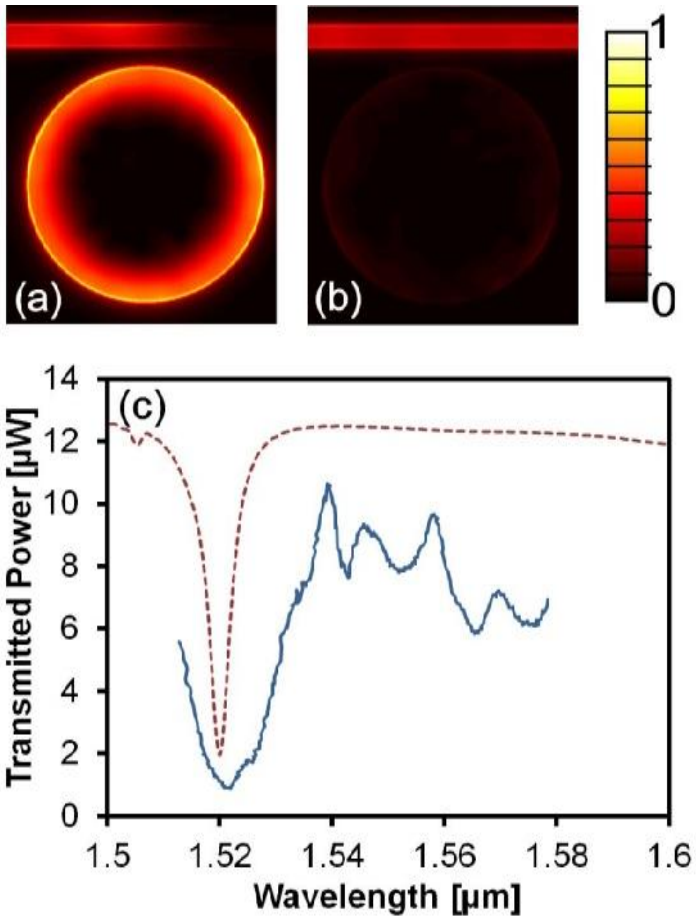

Figure 4.13: Normalized electric field intensity distributions of a 1 μm radius $Au/SiO_2/Si$ disk resonator evanescently coupled to a bus waveguide by a 200 nm gap at the Au/SiO_2 interface (a) 'on' (λ=1.52 μm) and (b) 'off' (λ=1.55 μm) resonance. (c) Experimental broadband transmission (blue solid line) for 1 μm radius MIS disk resonator evanescently coupled from the MIS bus waveguide by a 200 nm gap. Red dashed line shows experimentally normalized theoretical transmission as calculated with the FDTD method.

4.5 Conclusion

$Au/SiO_2/Si$ MIS nanoplasmonic waveguides and devices were designed, fabricated, and characterized on the CMOS compatible SOI platform. 200 nm wide $Au(50nm)/SiO_2(50nm)/Si(340nm)$ MIS waveguides were found to have a

propagation length of 16.0 µm, 73% of the predicted value of 21.9 µm, and a coupling efficiency of 59.4% to conventional SOI ridge waveguides. The experimentally realized MIS waveguides were used to develop Bragg reflector resonators, Bragg mirrors, and disk resonators on the same platform. With a compact device footprint of only 1.5 μm^2, the Bragg reflector resonator was demonstrated to have a Q factor as high as 64.4. The associated figure of merit of 42.9 μm^{-2} is to my knowledge the highest yet established for a silicon nanoplasmonic device.

Chapter 4 References

[1] W. Bogaerts, P. D. Heyn, T. V. Vaerengergh, K. D. Vos, S. K. Selvaraja, T. Claes, P. Dumon, P. Bienstman, D. V. Thourhout, and R. Baets, "Silicon microring resonators," Laser Photon. Rev. **6**, 47-73 (2012).

[2] Q. Xu, D. Fattal, and R. G. Beausoleil, "Silicon microring resonators with 1.5-μm radius," Opt. Express **16**, 4309-4315 (2008).

[3] M. Belotti, M. Galli, D. Gerace, L. C. Andreani, G. Guizzetti, A. R. Md Zain, N. P. Johnson, M. Sorel, and R. M. De La Rue, "All-optical switching in silicon-on-insulator photonic wire nano-cavities," Opt. Express **18**, 1450-1461 (2010).

[4] S. Zhu, G. Q. Lo, J. Xie, and D. L. Kwong, "Towards athermal plasmonic ring resonators based on Cu-TiO_2-Si hybrid plasmonic waveguide," IEEE Photonics Technol. Lett. **25**, 1161-1164 (2013).

[5] S. Zhu, G. Q. Lo, and D. L. Kwong, "Performance of ultracompact copper-capped silicon hybrid plasmonic waveguide-ring resonators at telecom wavelengths," Opt. Express **20**, 15232-15246 (2012).

[6] M. Wu, Z. Han, and V. Van, "Conductor-gap-silicon plasmonic waveguides and passive components at subwavelength scale," Opt. Express **18**, 11728-11736 (2010).

[7] S. Bhadra and A. Ghatak, *Guided Wave Optics and Photonic Devices* (CRC Press, Boca Raton, 2013).

[8] P. B. Johnson and R. W. Christy, “Optical constants of the noble metals,” Phys. Rev. B **6**, 4370-4379 (1972).

[9] E. D. Palik, *Handbook of Optical Constants of Solids* (Academic Press, San Diego, 1998).

[10] P. Maraghechi, K. Cadien, and A. Y. Elezzabi, “A novel nanofabrication Damascene lift-off technique,” IEEE Trans. Nanotechnol. **10**, 822-826 (2011).

[11] P. Lalanne and J. Hugonin, "Bloch-wave engineering for high-Q, small-V microcavities," IEEE J. Quantum Electron. **39**, 1430-1438 (2003).

[12] E. Hecht, *Optics* (Addison Wesley, San Francisco, 2002).

[13] Origin (OriginLab, Northampton, MA).

Chapter 5

Ultrafast InGaAs-Based Nanoplasmonic Amplifier[4]

5.1 Background

As previously discussed, traditional nanoplasmonic waveguides suffer from an intrinsic trade-off between minimizing propagation losses and maximizing modal confinement. Metal-insulator-metal (MIM) waveguides enable mode sizes down to tens of nanometers, but with the associated high losses on the order of 0.1 μm^{-1}. Hybridization of nanoplasmonic waveguides, through the inclusion of a thin low index spacer layer between a high index dielectric layer and a metal layer [1], can be used to increase the propagation length of MIM waveguides by transforming them into metal-insulator-semiconductor-insulator-metal (MISIM) waveguides. Such a configuration can extend the propagation length of a MIM waveguide from micrometers to tens of micrometers. However, accessing propagation lengths beyond tens of micrometers requires the inclusion of active compensation of ohmic losses through the incorporation of optical gain materials.

[4] *A version of this chapter has been published. M. P. Nielsen and A. Y. Elezzabi, J. Opt.* ***15****, 075202 (2013).*

Plasmonic systems in general require much higher gain coefficients for lossless propagation, the first step towards amplification and lasing, than their photonic counterparts. As such, the rare-earth doped glasses used for amplification in photonics, such as erbium doped glass at the telecommunication wavelengths, are not capable of sufficient gain. Heavily doped erbium glass, for instance, is limited to a maximum gain of 1 cm^{-1} at 1.535 μm [2]. This is due to a phenomenon called co-operative up-conversion, which at high doping concentrations limits amplifier performance, as pump power is lost to non-radiative interactions between the dopant ions. Dyes, which, like rare-earth dopants, function as optical dipoles can be included into a dielectric such as a polymer or glass and can provide gain from 100 cm^{-1} at lower concentrations to several thousand inverse centimeters. Rhodamine 6G (R6G), for example, provides at a moderate concentration of 5 mM or 3 x 10^{-8} cm^{-3} 100-500 cm^{-1} at 800 nm and 2000-3500 cm^{-1} at the full inversion concentration of 40 mM [3]. However, despite the high solubilities of dyes into dielectrics, concentration dependent effects limit the achievable gain, limiting practical concentrations far below the solubility limit [3]. These effects include limiting the attainable density of excited states through processes such as Föster energy transfer or reducing the quantum efficiency and lifetime of the dipoles through the formation of dimers or clusters. Dopant-based gain materials such as dyes, rare-earth ions and quantum dots, are restricted to optical pumping schemes, which require the optical pump to propagate in the same waveguide and suffer similar attenuation losses as the signal to be amplified. Increasing the pump energy to overcome this dilemma leads to further issues as higher pump

intensities can lead to increased nonlinear multiphoton processes. Possible damage to the metal layers can also result as microscopic thermal damage can occur even below the bulk ablation threshold of a metal [4], and nanoscale features are more susceptible than the bulk material.

Semiconductor gain media, such as bulk direct bandgap semiconductors and quantum wells, are capable of providing the optical gain required for loss compensation in MIM and MISIM waveguides. InGaAs-based systems are a stronger contender for incorporating gain at the telecommunication wavelengths as the bandgap of InGaAs ranges from 870 nm to 3440 nm depending of the ratio of indium to gallium. At 50% inversion bulk $In_{0.485}Ga_{0.585}As$ can provide gain of up to 2500 cm^{-1} at 1550 nm [5], whereas a single strained well of $In_{0.53}Ga_{0.47}As$ provides gain of approximately 2000 cm^{-1} at 1500 nm [4]. Of particular interest is bulk InGaAs which has several advantages for nanoplasmonic on-chip functionality, such as ease of fabrication and integration, direct electrical pumping, and low power consumption. Recently there has been considerable effort in fabricating functional room-temperature surface plasmon lasers [6-9], or SPASERs, incorporating InGaAs. However, the focus on lasers has left the integration of an amplifier into a nanoplasmonic interconnect unexplored. Not only does the incorporation of the amplifier need to result in an increased effective propagation length for the interconnect network, but any distortion effects on the signal pulses must be characterized for real world applications.

5.2 InGaAs-Based Nanoplasmonic Amplifier Design

Presented here is an electrically pumped metal-insulator-semiconductor-insulator-metal (MISIM) nanoplasmonic amplifier design based on $In_{0.485}Ga_{0.515}As$ as the bulk semiconductor gain medium for signal amplification at 1.55 μm. By removing the contacts used for electrical pumping, the amplifier design can easily be converted into a standard MISIM waveguide for interconnect applications. When integrated into such an interconnect network, the amplifier can maintain signal bit rates of up to 500 GHz without pulse distortion and provide loss compensation after over a hundred micrometers of signal propagation. The nanoplasmonic amplifier, with schematic depicted in Figure 5.1 (a), consists of an InGaAs/InP pillar grown on an InP substrate. Doped InGaAs/InP layers act as injection layers to the gain region, the $In_{0.485}Ga_{0.515}As$ core, and confine the mode to the gain region in the vertical direction through index mismatch between InGaAs and InP. Silver sidewalls provide the plasmonic character of the amplifier through sub-diffraction limit confinement in the horizontal direction. Electrical pumping of the $In_{0.485}Ga_{0.515}As$ gain region is conducted through ohmic Ti/Pd/Au contacts located on the top of the semiconductor pillar and on the substrate connected to the doped InGaAs/InP injection layers. Electrical isolation is achieved through conformal hafnium oxide, HfO_2, spacer layers between the semiconductor pillar and the metallic sidewalls. The HfO_2 spacer layers reduce the propagation losses of the amplifier by

transforming it into a hybrid plasmonic-photonic waveguide. Hybrid plasmonic-photonic waveguides take advantage of the phenomena that the inclusion of a thin low index insulating layer between the metal and a higher index layer highly concentrates the electric field in the thin low index material, reducing losses without significantly increasing the modal volume. In such a structure, the signal propagates mainly in the HfO_2 spacer layers while being amplified in the InGaAs core. By using a high index dielectric such as HfO_2 (n=1.9 at 1.55 µm) as opposed to a lower index dielectric like SiO_2 (n=1.45 at 1.55 µm), more of the mode is confined to the core. Here, modal confinement is defined as the fraction of the modal power confined to a section of the inactive amplifier, found by integrating the electric field intensity in that region, compared to the total modal power. To fabricate such as design, first the doped semiconductor pillar would be grown on an InP substrate using metalorganic chemical vapour deposition and then reactive ion etching to define the structure. Atomic layer deposition of the conformal HfO_2 sidewalls and selective removal of the insulator from the top of the pillar through etching or planarization to define the amplification regions followed by deposition of the ohmic contacts and the silver layer [7] would complete the structure.

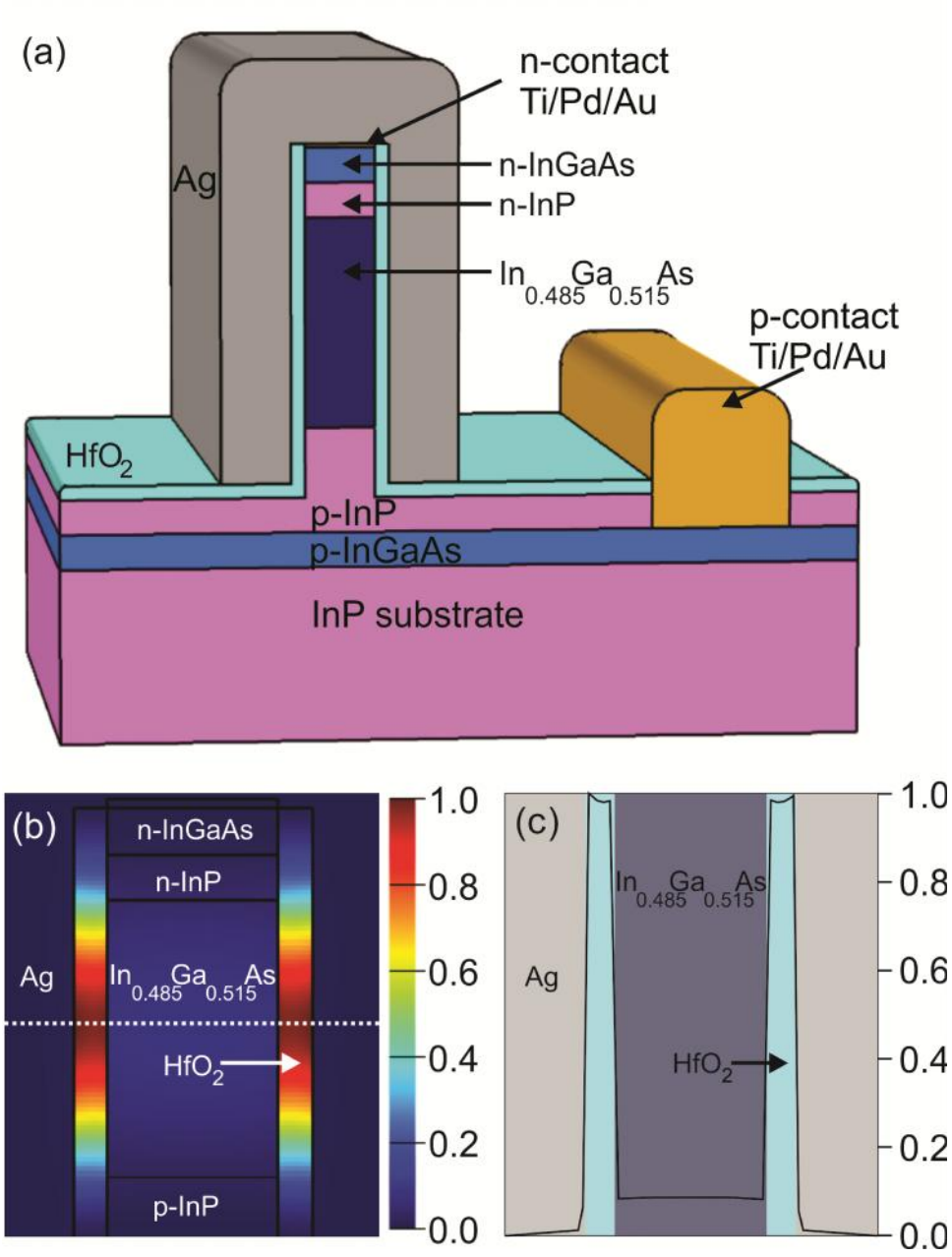

Figure 5.1: (a) Schematic of the nanoplasmonic amplifier. (b) 2-D and (c) 1-D cross sections of the intensity mode profiles of the fundamental mode of the amplifier at λ= 1.55 μm with $In_{0.485}Ga_{0.515}As$ core width *W*=100 nm, *H*=300 nm, and 20 nm HfO_2 spacer layers. The cross section is taken at the center of the core as depicted by the dashed line in (b).

To ensure electrical isolation of the gain region from the metallic sidewall, so that the pump current flows only from one ohmic contact to the other through the semiconductor pillar, the HfO_2 spacer layers were set to a thickness of 20 nm. While thinner spacer layers would force more of the mode into the InGaAs gain region, thus increasing the effective gain of the amplifier, they would increase the propagation losses and risk current leakage or electron tunneling. An additional advantage of the HfO_2 spacer layers, beyond deceasing the propagation losses and providing electrical isolation for the pumping scheme, is to decrease the sensitivity of the amplifier to fluctuations in the pump current. The waveguide core was set at a width of W=100 nm and a height of H=300 nm. For widths below 100 nm the losses become very high (>0.2 dB/μm), whereas above W=100 the mode at 1.55 μm in the waveguide core begins to lose its plasmonic character and nanoscale confinement. The vertical dimensions of the p-InGaAs/p-InP/$In_{0.485}Ga_{0.515}As$/n-InP/n-InGaAs pillar were selected to be 50nm/50nm/300nm/150nm/50nm, respectively, and were topped by a 5 nm Ti/Pd/Au n-contact, surrounded by 100 nm Ag, and separated by 500 nm from the Ti/Pd/Au p-contact. Figure 5.1 (b,c) depict the intensity distribution of the fundamental mode of this waveguide at 1.55 μm. With only 18% of the mode is confined to the InGaAs gain region the effective gain of the amplifier is reduced below is maximum value since effective gain is calculated through the overlap integral between modal distribution and the material gain, and the propagation length of the mode becomes 23.3 μm as calculated with the FDTD method in the unpumped amplifier.

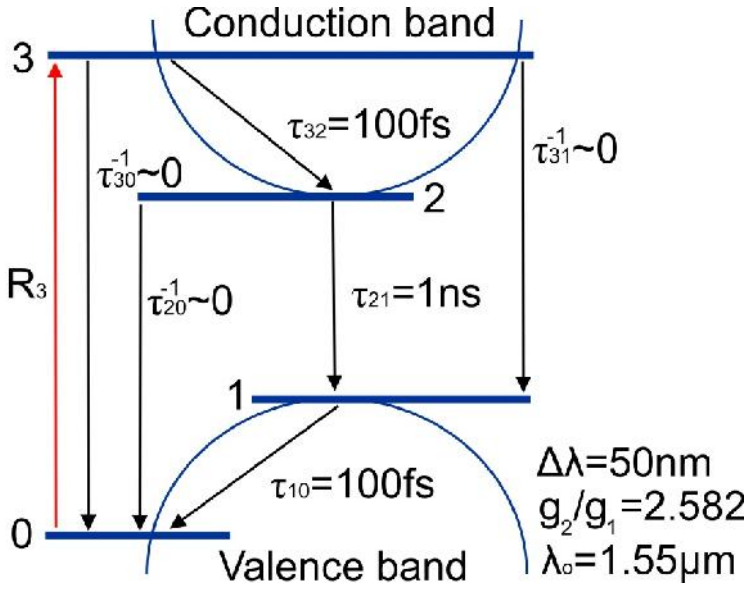

Figure 5.2: 4-level laser model for $In_{0.485}Ga_{0.515}As$ gain medium showing the laser level transition rates and the properties of the laser transition.

5.3 FDTD Formulation of InGaAs Gain Material

In order to examine the gain characteristics of the amplifier and the effect of ultrahigh bandwidth amplification on a pulse train under realistic conditions, self-consistent 3-D finite difference time domain (FDTD) simulations incorporating the full rate equations to describe the time-dependent gain dynamics of the $In_{0.485}Ga_{0.515}As$ material were conducted using the commercial software Lumerical FDTD Solutions and the material plugin *saturablegainnielsen* as described in Appendix B. The 1.55 μm signal is injected into the nanoplasmonic amplifier undergoing electrical pumping and the output is measured to determine

the transmission at various pump current densities. It has been shown in [10] that in semiconductor gain media the conduction and valence bands can be effectively modeled using a set of discrete energy levels, as is commonly done for gas or solid-state gain media. Here, a simplified approach is taken by using only four levels to reduce the computational time required for the simulations. While this does not provide the complete semiconductor laser gain dynamics, it is sufficient to accurately the capture the $In_{0.485}Ga_{0.515}As$ gain amplification characteristics, especially when both the signal intensity and pump current density are kept to moderate levels below saturation. The input peak intensity was set at 2.7×10^7 W/m^2 in the InGaAs core (4 μW peak total modal power or 1 μW mean modal power for a Gaussian pulse), which is an order of magnitude less than the saturation intensity of 6×10^8 W/m^2. To avoid spontaneous emission lasing and to allow for a constant spontaneous lifetime and gain bandwidth, the pump current density is kept below the lasing threshold for the amplifier with a maximum injection carrier density of N=6.86×10^{22} m^{-3}. This is below the density of ~10^{24} m^{-3} where Auger recombination and the decrease of effective carrier lifetimes from the high current density become important. The $In_{0.485}Ga_{0.515}As$ gain material mode, presented in Figure 5.2, is a 4-level laser system with the bottom of the conduction band and top of the valence band as the upper and lower laser levels, respectively. The bandgap, as determined by the material composition, is 0.8 eV. The pump level considered to be high in the conduction band and the undepletable ground state is taken to be low in the valence band. The population density rate equations (Eq. 5.1-5.4) and macroscopic polarization, $\vec{P}$, auxiliary

differential equation (Eq. 5.5) [11] are used to calculate the polarization from the gain medium:

$$\frac{dN_3}{dt} = R_3(t) - \frac{N_3(t)}{\tau_3}, \tag{5.1}$$

$$\frac{dN_2}{dt} = -\frac{N_2(t)}{\tau_2} + \frac{N_3(t)}{\tau_{32}} + \frac{1}{2\hbar\omega_o}\vec{E}(t)\cdot\frac{d\vec{P}(t)}{dt}, \tag{5.2}$$

$$\frac{dN_1}{dt} = -\frac{N_1(t)}{\tau_1} + \frac{N_3(t)}{\tau_{31}} + \frac{N_2(t)}{\tau_{21}} - \frac{1}{2\hbar\omega_o}\vec{E}(t)\cdot\frac{d\vec{P}(t)}{dt}, \tag{5.3}$$

$$\Delta N(t) = N_2(t) - \frac{g_2}{g_1}N_1(t), \tag{5.4}$$

$$\frac{d^2\vec{P}(t)}{dt^2} + \Delta\omega_o\frac{d\vec{P}(t)}{dt} + \omega_o^2\vec{P}(t) = -\frac{6\pi\varepsilon_o c^3}{\omega_o^2\tau_{21}}\Delta N(t)\times\vec{E}(t), \tag{5.5}$$

where $R_3 = J/(H\times q)$ is the pump rate, J is the current density, q is the elementary charge, $\vec{E}$ is the electric field, τ_{ij} is the lifetime of the transition from level k to level j, $\tau_j^{-1} = \sum\tau_{jk}^{-1}$ (where $\tau_{30}^{-1} = \tau_{31}^{-1} = \tau_{21}^{-1} = 0\,fs^{-1}$, $\tau_{32} = \tau_{32} = 100\,fs$, and $\tau_{21} = 1\ ns$), N_i is a population density of level j, g_j is the degeneracy of a level j, ω_o is the center frequency of the gain spectrum, and $\Delta\omega_o$ is the bandwidth of the gain spectrum. As the other interband transitions have even larger time constants than the lasing transition of 1 ns, which is considerably longer than the simulation time, they will have only a small effect on the simulation and thus have been neglected. The effect of this is that the model will slightly overestimate the effective gain than if these non-amplifying carrier recombination processes had been included. The discretized equations for the total electric field and polarization at each time step i of duration Δt can be seen in Eq. 5.6-5.10:

$$N_3^{i+1} = \frac{1}{\Delta t + 1/2\tau_3}[R_3 + N_3^i(\frac{1}{\Delta t} - \frac{1}{2\tau_3})], \tag{5.6}$$

$$N_2^{i+1} = \frac{1}{\Delta t + 1/2\tau_2}[N_2^i(\frac{1}{\Delta t} - \frac{1}{2\tau_2}) + \frac{1}{2\tau_{32}}(N_3^{i+1} + N_3^i) + \frac{(E^{i+1} + E^i)(P^{i+1} - P^i)}{4\pi h\nu_o \Delta t}], \tag{5.7}$$

$$N_1^{i+1} = \frac{1}{\Delta t + 1/2\tau_2}[N_1^i(\frac{1}{\Delta t} - \frac{1}{2\tau_1}) + \frac{1}{2\tau_{31}}(N_3^{i+1} + N_3^i) + \frac{1}{2\tau_{21}}(N_2^{i+1} + N_2^i) - \frac{(E^{i+1} + E^i)(P^{i+1} - P^i)}{4\pi h\nu_o \Delta t}], \tag{5.8}$$

$$\Delta N^{i+1} = N_2^{i+1} - \frac{g_2}{g_1} N_1^{i+1}, \tag{5.9}$$

$$P^{i+1} = \frac{2\Delta t^2}{2 + \Delta\nu_o \Delta t}[-\frac{6\pi\varepsilon_o c^3}{\nu_o^2 \tau_{21}} \Delta N^i E^i + (\frac{2}{\Delta t^2} - \nu_o^2)P^i + (\frac{\Delta\nu}{2\Delta t} - \frac{1}{\Delta t^2})P^{i-1}], \tag{5.10}$$

The polarization was then used to update the electromagnetic fields through Ampère's Law according to the FDTD Yee algorithm for Maxwell's equations at each time step. The complex refractive index values for InP, Ag, InGaAs, and HfO_2 across the simulated frequency range used can be found in [12-15].

5.4 Results

The plasmonic properties of a horizontal MISIM waveguide such as is presented here are chiefly governed by the waveguide width, *W*, rather than the height, *H*. As such, the nanoplasmonic amplifier performance at 1.55 μm was characterized for how the gain dynamics were varied with the waveguide's horizontal dimensions. The two critical dimensions for the operation of the

amplifier to be examined were the width of the semiconductor core, *W*, and the thickness of the HfO_2 spacer layers. Figure 5.3 (a) shows that, for moderate pump current densities, the optical signal gain coefficient is linear with the pump current density and exhibits steeper growth at larger core widths where more of the mode is confined to the gain medium. For example, with *W*=200 nm and 20 nm sidewalls, 33% of the mode resides in the $In_{0.485}Ga_{0.515}As$ core, but when *W* is decreased to 100 nm only 18% of the mode resides in the core. As the waveguide core is decreased from 200 nm to 50 nm, with a constant spacer layer thickness of 20 nm, the threshold pump current density required for lossless propagation increases from 0.4 kA/cm^2 to 2.3 kA/cm^2. Figure 5.3 (b) depicts the effect of varying the HfO_2 spacer layer thickness, wherein a similar trend can be observed. As the HfO_2 spacer layer increases, losses decrease, but the confinement of the mode to the core decreases as well. Increasing the spacer thickness from 10 nm to 20 nm causes the mode confinement in the $In_{0.485}Ga_{0.515}As$ core to drop from 27% to 18%. An additional advantage of the HfO_2 spacers, beyond decreasing the waveguide's propagation losses and providing electrical isolation for the pumping scheme, is to decrease the sensitivity of the amplifier to fluctuations in the pump current. As the nanoplasmonic amplifier gain coefficient is approximately linear with the pump current density before intensity saturation effects, the calculated curves in both Figure 5.3 (a) and Figure 5.3 (b) are kept below 4 kA/cm^2 to more accurately show the effect of varying *W* and the HfO_2 spacer thickness.

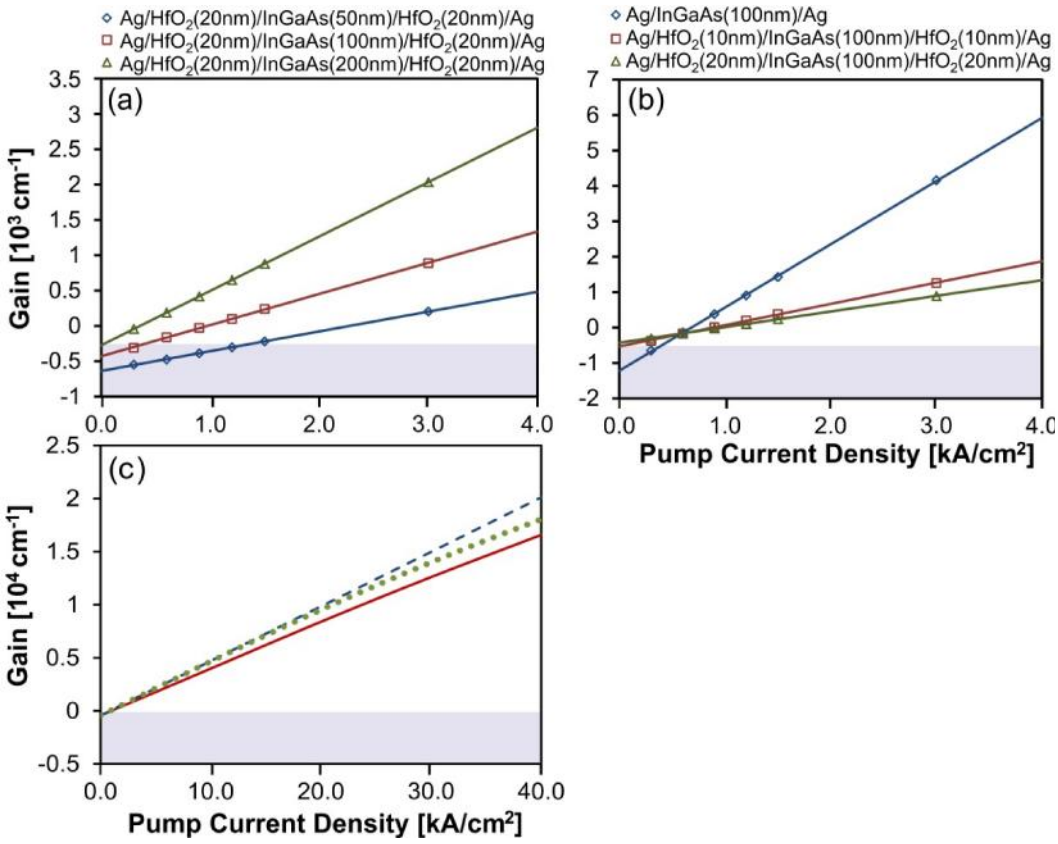

Figure 5.3: Effect of varying (a) W and (b) the HfO2 spacer thickness on the amplifier's gain at 1.55 µm at various pump current densities. (c) Comparison of the Ag/HfO_2(20nm)/$In_{0.485}Ga_{0.515}As$(100nm)/ HfO_2(20nm)/Ag amplifier gain at 1.55 µm as calculated with the presented FDTD model (red solid line) and a simple semiconductor optical amplifier model from [16] with (green dotted line) and without (blue dashed line) Auger recombination.

The presented FDTD rate equations model for the nanoplasmonic amplifier can be compared to a conventional semiconductor optical amplifier (SOA) model for the gain coefficient without intensity saturation effects [16] as depicted in Figure 5.3 (c):

$$g_m(\mu_o) = \frac{c^{2}\circledR^{3/2}}{\sqrt{2}\mu_o^2 n_o^{2}{}_{21}}\left[\frac{4m_e m_{hh}}{h(m_e+m_{hh})}\right]^{3/2}\cdot[f_c(E_c)-f_v(E_v)]\sqrt{\frac{E_c-E_v}{h}}, \qquad (5.11)$$

where m_e=0.043m_o is the electron effective mass, m_{hh}=0.46m_o is the heavy hole effective mass, m_o is the electronic rest mass, and n_o=3.63 is the refractive index of $In_{0.485}Ga_{0.515}As$ at ω_o. The energy at the bottom of the conduction band, E_c, and the energy at the top of the valence band, E_v, can be calculated assuming parabolic band shape by:

$$E_{c,v} = \frac{2®^2 k_{e,hh}^2}{m_{e,hh}}, \tag{5.12}$$

where $k_{e,hh}$=$m_{e,hh}$·$\mu_{e,hh}$·V/H is the carrier momentum with V as the pump current density dependent voltage across the active gain region, μ_e=1.149 $m^2V^{-1}s^{-1}$ as the electron mobility, and μ_{hh}=0.4 $m^2V^{-1}s^{-1}$ as the hole mobility. The occupation probabilities of an electron in either the conduction band, f_c, or valence band, f_v, as determined by Fermi-Dirac statistics are given by:

$$f_{c,v}(E) = \frac{1}{1+\exp(\frac{E - E_{fc,fv}}{kT})}, \tag{5.13}$$

where T=293K is the temperature of the device, k is the Boltzmann constant, and E_{fc} and E_{fv} are the carrier concentration dependent quasi-Fermi levels of the conduction and valence bands, respectively, as compared to the opposite band edge. The quasi-Fermi levels can be estimated with the Nilsson approximation [17]:

$$E_{fc,fv} = \pm(\ln\frac{N_{e,hh}}{N_{c,v}} + \frac{N_{e,hh}}{N_{c,v}}(64 + 0.05524\frac{N_{e,hh}}{N_{c,v}}(64 + \sqrt{\frac{N_{e,hh}}{N_{c,v}}}))^{-\frac{1}{4}})kT, \tag{5.14}$$

where $N_{e,hh}$ are the carrier concentrations and $n_{c,v}$ are constants given by:

$$n_{c,v} = 2(\frac{m_{e,hh}kT}{8®^3h^2})^{3/2}, \tag{5.15}$$

The effective gain coefficient of the amplifier can then be calculated by taking into account the mode overlap with the active gain region, *S*, and the mode propagation losses, $\alpha_{p,}$ using :

$$g_{m,eff}(\mu_o) = g_{m,eff}(\mu_o) \cdot S - \sim_p . \tag{5.16}$$

The comparative SOA model can be further expanded by introducing the carrier concentration dependent Auger recombination rate, $R_{Aug}=C_{Aug}N^3$ where $C_{aug}=2 \times 10^{-41}$ m^6/s is the Auger coefficient, which reduces the effective carrier concentration and gain coefficient at high pump current densities. At the pump current densities used in the FDTD simulations, the SOA model, as an oversimplified photonic model, actually overestimates the gain, even when Auger recombination is taken into account.

To examine the viability of the utilizing the nanoplasmonic amplifier to maintain the signal integrity of a 1.55 μm signal over nanoplasmonic chip lengths, the device was tested as part of an interconnect network under realistic conditions. A 3 μm long $Ag/HfO_2/In_{0.485}Ga_{0.515}As/HfO_2/Ag$ amplifier was coupled to a 147 μm interconnect formed out of the same MISIM waveguide and carrying a 500 GHz pulse train of 500 fs FWHM bits. To avoid pumping the interconnect, the top Ti/Pd/Au contact was replaced by a 20 nm HfO_2 film. This design also avoids undesirable cavity reflections from the amplifier interfaces. The amplifier was pumped at 36.6 kA/cm^2, requiring a total current of 0.1 mA. It should be noted that this current density is less than the 42.4 kA/cm^2 threshold current density for a room temperature nanoplasmonic laser or SPASER from [9], validating that the pump current density of the proposed device is within the operational range of a

real SPASER. Amplified and unamplified signal after 150 µm of propagation, alongside the initial signal, are presented in Figure 5.4 (a). The nanoplasmonic amplifier was capable of restoring the strength of the pulses after the 150 µm of propagation, whereas the unamplified pulses had decayed to 1% of their initial amplitude. The effect of pumping the amplifier is to modify the real and imaginary parts of the $In_{0.485}Ga_{0.515}As$ relative permittivity, manifesting as a propagation delay of ~140 fs and a dispersion leading to ~8% pulse broadening. For applications where nanoscale lengths are not required, the amplifier size can be scaled up in length without compromising performance, leading to a reduction in required pump current density and total injection current. Increasing the amplifier length to 30 µm and reducing the pump current density to 5.71 kA/cm^2 (or 141 µA injection current), offers comparable optical signal gain for 150 µm of signal propagation, with only a 90 fs propagation delay with respect to the unamplified pulse and ~3% pulse broadening. These results are depicted in Figure 5.4 (b). Despite the effectiveness of the nanoplasmonic amplifier, pulse widths below 500 fs suffer significant pulse broadening from the nonlinear distortion and begin to run into one another. For example, Figure 5.4 (c) depicts a 2 THz pulse train of 100 fs FWHM bits which suffers 48% pulse broadening and 50 fs propagation delay from the 3 µm nanoplasmonic amplifier pumped at 36.6 kA/cm^2.

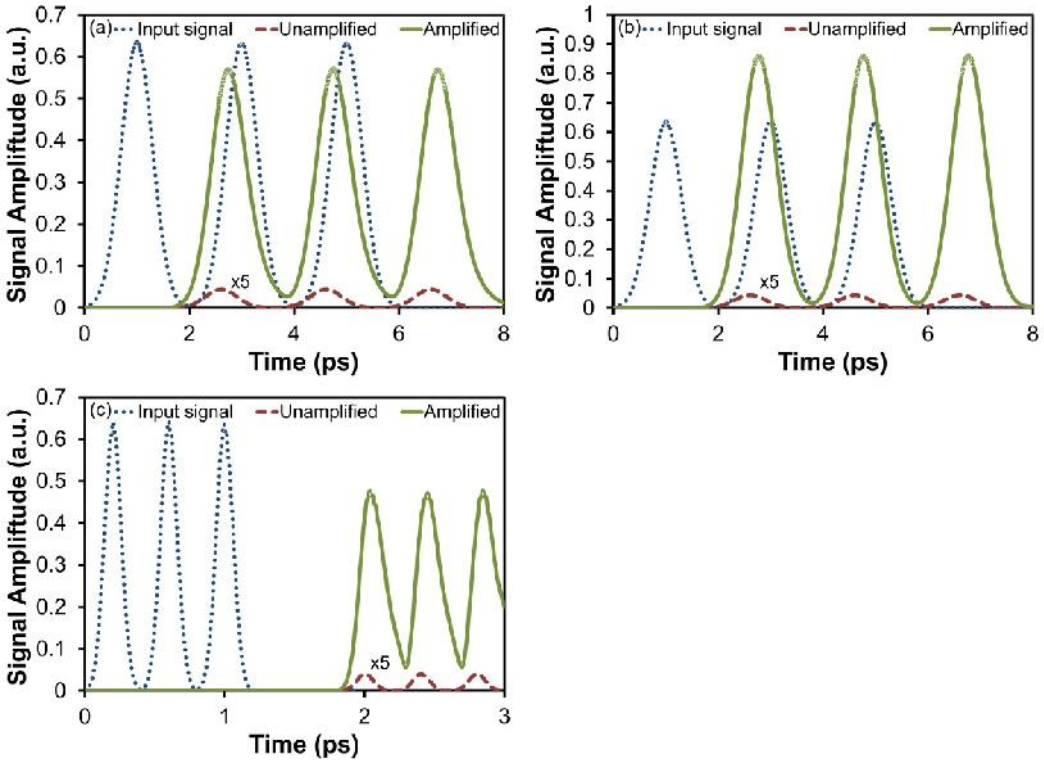

Figure 5.4: Propagation of a 500 GHz, 500 fs FWHM pulse train through a 150 µm interconnect network comparing amplified and unamplified signals (×5 scale) for two different amplifier lengths and pump current densities: (a) a 3 µm long amplifier pumped at 36.6 kA/cm^2 and (b) a 30 µm long amplifier pumped at 4.71 kA/cm^2. (c) Propagation of a 2 THz, 100 fs FWHM pulse train through a 150 µm interconnect network with a 3 µm long amplifier pumped at 36.6 kA/cm^2.

A major concern in CMOS electronics and other nanoscale systems is heat management. The high current densities and optical intensities in these systems, required due to the small scale of these systems, generate vast quantities of heat. Heat dissipation engineering, through device geometry, cooling fans, or liquid coolants such as liquid nitrogen and helium, must be used to maintain functional temperature levels. In order to study the heating in the proposed 3 µm nanoplasmonic amplifier, 3-D steady state finite element simulations using the

commercial software suite COMSOL Multiphysics were implemented. As in the FDTD simulations, the amplifier was studied while integrated into an interconnect network. Two heat sources, a 0.1 mA pump current corresponding to 36.6 kA/cm^2 pump current density between the contacts and a uniform boundary heat source proportional to the optical losses of a 4 μW signal along the metallic sidewalls, and two heat sinks, the semi-infinite InP substrate set to 293.15 K and the open boundary of air above the amplifier set to 293.15 K, were applied. The simulations employed literature values for the relative permittivity, density, electrical conductivity, heat capacity, and thermal conductivity of Ag [18], Au [18], InGaAs [19,20], InP [19,21], and HfO_2 [22,23], with the InP and InGaAs injector layers doping assumed to be 10^{18} cm^{-3}. The initial temperature of the system was assumed to be 293.15 K. Figure 5.5 depicts a steady-state temperature increase in the core of only 1.21 K. As such, the temperature dependence of the optical properties used in the FDTD simulations were safely ignored. Not only do these simulations show that the nanoplasmonic amplifier does not suffer from undue heating issues, but that 20 nm HfO_2 spacer layers provided sufficient electrical isolation with a negligible leakage current of only 1.5 nA/cm^2.

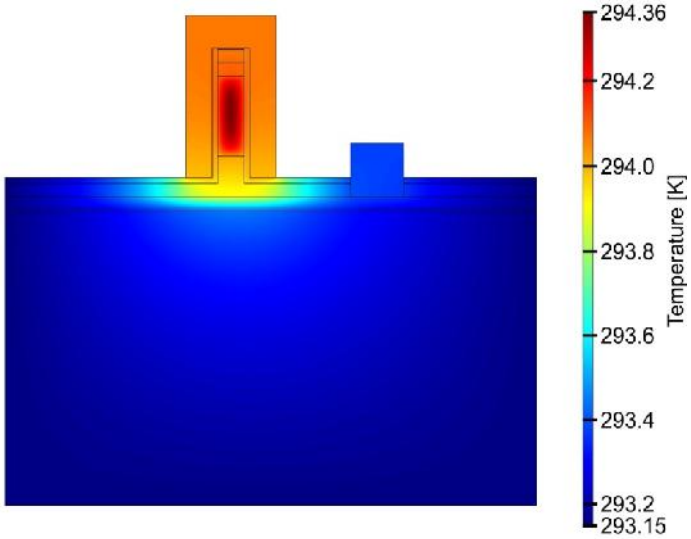

Figure 5.5: Steady-state temperature profile of the nanoplasmonic amplifier with $In_{0.485}Ga_{0.515}As$ core current density of 36.6 kA/cm^2, assuming an initial temperature of 293.15 K.

5.5 Conclusion

Nanoplasmonic systems require a method of compensating for their associated high ohmic losses if they are ever to replace conventional electronics as the future computing platform. Presented here was a simplified approach to modeling an $In_{0.485}Ga_{0.515}As$ based device capable of providing nanoplasmonic amplification at the telecommunication wavelength of 1.55 µm for 500 GHz 500 fs FWHM bit rate signals without significant signal distortion. The nanoplasmonic amplifier suffers from neither excessive heating nor current leakage. This device offers the possibility of incorporating effectively lossless nanoplasmonic interconnects into hybrid optical-electrical circuits.

Chapter 5 References

[1] I. Avrutsky, R. Soref, and W. Buchwald, “Sub-wavelength plasmonic modes in a conductor-gap-dielectric system with a nanoscale gap,” Opt. Express **18**, 348-362 (2010).

[2] Y. C. Yan, A. J. Faber, H. de Waal, P. G. Kik, and A. Polman, "Erbium-doped phosphate glass waveguides on silicon with 4.1 dB/cm gain at 1.535 μm," Appl. Phys. Lett. **71**, 2922-2924 (1997).

[3] I. De Leon and P. Berini, “Modeling surface plasmon-polariton gain in planar metallic structure,” Opt. Express **17**, 20191-20202 (2009).

[4] P. Berini and I. D. Leon, "Surface plasmon-polariton amplifiers and lasers," Nat. Photonics **6**, 16-24 (2012).

[5] X. Chen, B. Bhola, Y. Huang, and S. T. Ho, “Multi-level multi-thermal-electron FDTD simulation of plasmonic interaction with semiconducting gain media: applications to plasmonic amplifiers and nano-lasers,” Opt. Express **18**, 17220-17238 (2010).

[6] M. T. Hill, M. Marell, E. S. Leong, B. Smalbrugge, Y. Zhu, M. Sun, P. J. van Veldhoven, E. J. Geluk, F. Karouta, Y. S. Oei, R. Nöetzel, C. Z. Ning, and M. K. Smit, “Lasing in metal-insulator-metal sub-wavelength plasmonic waveguides,” Opt. Express **17**, 11107-11112 (2009).

[7] M. J. H. Marell, B. Smalbrugge, E. J. Geluk, P. J. van Veldhoven, B. Barcones, B. Koopmans, R. Nöetzel, M. K. Smit, and M. T. Hill,

"Plasmonic distributed feedback lasers at telecommunications wavelengths," Opt. Express **19**, 15109-15118 (2011).

[8] J. H. Lee, M. Khajavikhan, A. Simic, Q. Gu, O. Bondarenko, B. Slutsky, M. P. Nezhad, and Y. Fainman, "Electrically pumped sub-wavelength metallo-dielectric pedestal pillar lasers," Opt. Express **19**, 21524-21531 (2011).

[9] K. Ding, Z. C. Liu, L. J. Yin, M. T. Hill, M. J. H. Marell, P. J. van Veldhoven, R. Nöetzel, and C. Z. Ning, "Room-temperature continuous wave lasing in deep-subwavelength metallic cavities under electrical injection," Phys. Rev. B **85**, 041301 (2012).

[10] Y. Huang and S. T. Ho, "Computational model of solid-state, molecular, or atomic media for FDTD simulation based on a multi-level multi-electron system governed by Pauli exclusion and Fermi-Dirac thermalization with application to semiconductor photonics," Opt. Express **14**, 3569-3587 (2006).

[11] A. E. Siegman, *Lasers*, A. Kelly, ed. (University Science Books, Mill Valley, 1986).

[12] E. D. Palik, *Handbook of Optical Constants of Solids*, (Academic Press, San Diego, 1998).

[13] P. B. Johnson and R. W. Christy, "Optical Constants of the Noble Metals," Phys. Rev. B **6**, 4370-4379 (1972).

Chapter 6

Ultrafast All-Optical Modulation in a Plasmonic Nanoring Resonator[5]

6.1 Background

Silicon-based plasmonic modulators are the first step in the development of a CMOS compatible plasmonic analogue to the electronic transistor. Previous approaches to signal modulation in silicon plasmonics have included charge redistribution using an applied electric field [1,2] and photogeneration of free-carriers using above band gap pulses [3-6]. Unfortunately, the reliance on driving electronics to produce the applied electric field for charge redistribution limits the modulation bandwidth of a device to that of the electronic components, negating one of the primary advantages of optical circuitry over conventional electronics. On the other hand, the use of above band gap radiation as a modulation mechanism in silicon requires the on-chip integration of non-silicon based routing interconnects and devices to distribute and control the control pulses, vastly

[5] *A version of this chapter has been submitted for publication. M. P. Nielsen and A. Y. Elezzabi, Opt. Express, 190436, submitted May 10, 2013.*

increasing the complexity of any future chip-based technology. To overcome this constraint, one can turn to exploiting silicon's nonlinearities. Already well explored for use in silicon photonics [7], they are applicable for silicon plasmonic devices as well [8]. Two-photon absorption (TPA) allows for free-carrier photogeneration with a pump wavelength within the telecommunication band. The generated free carriers can then modulate a signal either through absorption (free carrier absorption or FCA) or by altering the refractive index (the plasma dispersion effect or PDE) before recombining. As such, the modulation bandwidth is limited not by the pump or signal pulses, but by the free-carrier recombination lifetime. Although the indirect bandgap nature of silicon normally limits the free carrier recombination lifetime to timescales upwards of nanoseconds, the introduction of carrier recombination centers through ion implantation of oxygen reduces the free-carrier recombination lifetime to as low as 600fs [9]. Since TPA is an intensity dependent process, the enhanced modal confinement available to nanoplasmonic devices increases the efficiency of free-carrier generation. By further concentrating a signal's intensity through a resonant device, not only can the modulator device footprint be reduced to the nanoscale but the required pump energy for modulation can be reduced as well.

6.2 MISIM Nanoplasmonic Ring Resonator Modulator Design

The viability of ultrafast all-optical modulation in a silicon-based plasmonic device using TPA as the nonlinear modulation mechanism is explored through $Ag/HfO_2/Si/HfO_2/Ag$ MISIM nanoring resonators. The nanoring resonators and associated bus waveguides take advantage of the nanoscale confinement and sharp bending radii offered by the MISIM configuration, while retaining a moderate propagation length through its hybrid nature and the use of the low loss plasmonic metal silver. Free-carriers photogenerated by degenerate TPA from a pump pulse modify the complex refractive index of the nanoring resonator through FCA and the PDE, modulating the resonant characteristics of the nanoring and the transmission of a probe pulse.

Three devices referred to as Device A, B and C, differing in nanoring radii and HfO_2 spacer layer thickness, are investigated. A schematic diagram and the broadband transmission characteristics from λ=1.3-1.6µm of Devices A, B and C are presented in Figure 6.1 (a,b), Figure 6.1 (c,d) and Figure 6.1 (e,f) respectively. The nanoring resonators and bus waveguides are formed of 100 nm wide by 340 nm tall oxygen ion implanted silicon waveguides with HfO_2 dielectric spacer layers and silver sidewalls on SiO_2. The thickness of the HfO_2 spacer layers is varied from 10 nm in Device A to 20 nm in Device B and C to the determine influence of the spacer layer on device performance. Similarly, the outer radii of the nanorings is varied form 540 nm in Device A and B to 1 µm in Device C to

discern the influence of the nanoring radii. A radii of 540 nm gives a compact device footprint of only 1.4 μm^2. Apertures 200 nm wide and 50 nm deep couple the nanorings to a MISIM nanoplasmonic bus waveguide. The modulation properties of the devices were characterized with 400 fs FWHM probe pulses, comparable to the lifetime of the nanorings' probe resonances, which are injected at the input port with a pulse energy of 6.4 fJ and centered at resonance at 1.53 µm, 1.58 µm and 1.55 µm for Devices A, B and C respectively as depicted in Figure 6.1 (b,d,f). The transmission characteristics are modulated with 400 fs FWHM pump pulses injected at the input port with various pulse energies ranging from 6.4 fJ to 64 pJ and centered at resonances at 1.35 µm, 1.37 µm and 1.44 µ for Devices A, B and C respectively as depicted in Figure 6.1 (b,d,f). The fundamental TE modes of the MISIM nanoplasmonic bus waveguides at 1.55 µm with 10 nm and 20 nm HfO_2 spacer layers can be seen in Figure 6.1 (g) with L_p=16.4 µm and Figure 6.1 (h) L_p=22.2 µm correspondingly.

Such devices would be fabricated by first lithographically defining a mask on an oxygen ion implanted SOI wafer, and then dry etching through the device layer to define the silicon elements. ALD of the conformal HfO_2 dielectric spacer layers would be followed by a second EBL step used to deposit silver around the structure through sputtering and lift-off processes. Finally, chemical mechanical polishing (CMP) would be used to planarize the structures. This is similar to the fabrication undertaken and described in Chapter 3.

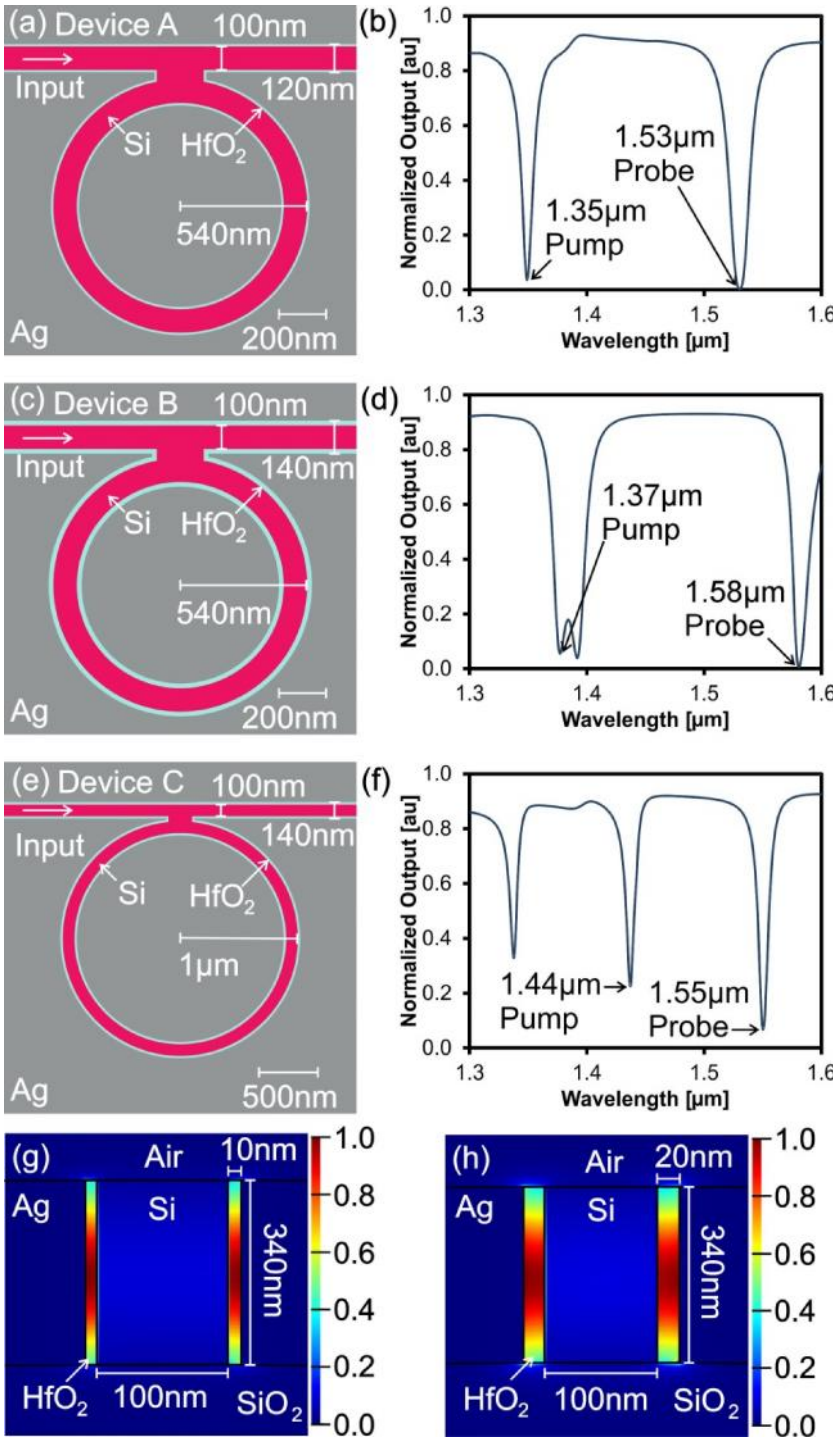

Figure 6.1: Schematic diagrams illustrating nanoring and bus waveguide dimensions and broadband transmission characteristics with pump and probe pulse resonances for (a,b) Device A, (c,d) Device B, and (e,f) Device C. Normalized electric field intensity distribution for fundamental TE mode for bus waveguides with (g) 10 nm and (h) 20 nm HfO_2 spacer layers.

6.3 FDTD Formulation of TPA and Free Carrier Effects in Silicon

The proposed nanoring resonators were characterized as all-optical modulators using self-consistent 3-D FDTD simulations incorporating the nonlinear TPA process, FCA and the PDE in silicon using the commercial software Lumerical FDTD Solutions and the material plugin *SiTPA* as described in Appendix B. In the Yee algorithm used by Lumerical, the electric displacement field *D* is calculated from Ampère's equation, and the electric field *E* is calculated from both *D* and the polarization *P* by:

$$D = \varepsilon_o E + P, \tag{6.1}$$

The complex refractive index values from [10], [11] and [12] were used to calculate the polarization for Ag, HfO_2 and SiO_2 respectively. The polarization for silicon was divided into linear and nonlinear components:

$$P_{Si} = P_{linear} + P_{TPA} + P_{FCA} + P_{PDE}, \tag{6.2}$$

where the linear component is calculated using the refractive index values from [12] and the nonlinear components are calculated using the method derived in [13] as described here. The other nonlinearities present in silicon, namely the Kerr and Raman effects, were neglected for this investigation as for the time, length and energy scales under consideration they are much weaker than TPA and the carrier effects [8].

The change in optical intensity I due to TPA is found by $dI/dL = -\ _{TPA}I^2$, where β_{TPA}=0.8 cm/GW [14] is the TPA coefficient and L is the interaction length. This leads to the nonlinear polarization due to TPA, $P_{TPA} = \varepsilon_o \chi_{TPA} E$, which can be calculated from:

$$\chi_{TPA} = i\frac{cn_{o\ TPA}}{\omega} I = -\frac{c^2\varepsilon_o n_{o\ TPA}^2}{i\omega}\left|E\right|^2, \tag{6.3}$$

which is discretized through the use of the substitution of $-i\omega$ by $\partial/\partial t$ and a Fourier transform into:

$$\chi_{TPA}^{i+1} = \chi_{TPA}^{i} - \frac{c^2\varepsilon_o n_{o\ TPA}^2 \Delta t}{2}\left|E^{i+1/2}\right|^2 \cong \chi_{TPA}^{i} - \frac{c^2\varepsilon_o n_{o\ TPA}^2 \Delta t}{4}\left[\left|E^{i+1}\right|^2 + \left|E^{i}\right|^2\right], \tag{6.4}$$

where χ_{TPA} is the nonlinear susceptibility due to TPA, c is the speed of light, n_o=3.48 is the refractive index of silicon at 1.55 μm, ε_o is the permittivity of free space, ω is the angular frequency, superscript i is the discretized step index, and Δt is the time step. To achieve self-consistency, the dependence of χ_{TPA}^{i+1} on E^{i+1} in Eq. 6.4 requires iteration. Here the electron concentration, N_e, and hole concentration, N_h, are assumed to be equal in magnitude and will be referred to as the free-carrier concentration N_f. The free carrier concentration generated by TPA is calculated through the rate equation:

$$\frac{dN_f}{dt} = \frac{1}{2\hbar\omega}\left(-\frac{dI}{dz}\right) - \frac{N_f}{\tau_r} = \frac{c^2\varepsilon_o^2 n_{o\ TPA}^2}{8\hbar\omega}\left|E\right|^4 - \frac{N_f}{\tau_r}, \tag{6.5}$$

which can be discretized into:

$$N_f^{i+1/2} = \frac{2\tau_r - \Delta t}{2\tau_r + \Delta t} N_f^{i-1/2} + \frac{\tau_r \Delta t}{2\tau_r + \Delta t}\frac{c^2\varepsilon_o^2 n_{o\ TPA}^2}{4\hbar\omega}\left|E^i\right|^4, \tag{6.6}$$

where τ_r=1 ps is the free-carrier recombination time in oxygen doped silicon [9].

The free carrier effects, FCA and the PDE, can now be implemented using the generated carriers. The change in I due to FCA is $dI/dL = -\pm_{FCA} N_f I$, which leads to a polarization due to FCA of:

$$P_{FCA} = i\pounds_0 \pounds_{iFCA} E = -\frac{c\pounds_o n_o \pm_{FCA} N_f}{i\mu} E, \tag{6.7}$$

where $\pm_{FCA} = 3.6\times10^{-21}[m^2](\text{a}[\ll m]/1.55)^2$ [15] is the free-carrier absorption cross-section. The polarization due to the PDE that arises from the free-carrier refractive index change is:

$$P_{PDE} = \pounds_o \pounds_{rPDE} E = \pounds_o 2n_o \Delta n_{plasma} E, \tag{6.8}$$

where $\Delta n_{plasma} = \left[-8.8\times10^{-22} N_e - 8.5\times10^{-18} N_h^{0.8}\right](\text{a}[\ll m]/1.55)^2$ [16].

Eq. 6.1 can now be rewritten for silicon as:

$$\tilde{D} = D - P_{linear} = \pounds_o E\left[2n_o \Delta n_{plasma} - \frac{cn_o \pm_{FCA} N_f}{i\mu} - \frac{c^2 \pounds_o n_o^2 \ _{TPA}}{2i\mu}|E|^2\right], \tag{6.9}$$

This can be discretized through of the substitution of $-i\omega$ by $\partial/\partial t$ and then performing a Fourier transform. Rearranging in order to solve for E^{n+1} yields:

$$E^{i+1} = \frac{g^-(E^{i+1})}{g^+(E^{i+1})} E^n + \frac{\tilde{D}^{i+1} - \tilde{D}^i}{\pounds_o g^+(E^{i+1})}, \tag{6.10}$$

where

$$g^+(E^{i+1}) = 2n_o \Delta n_{plasma}(E^{i+1}) + \frac{cn_o \pm_{FCA} N_f^{i+1/2} \Delta t}{2} + \frac{c^2 \pounds_o n_o^2 \ _{TPA} \Delta t\left[|E^{i+1}|^2 + |E^i|^2\right]}{8}, \tag{6.11}$$

and

$$g^{-}(E^{i+1}) = 2n_o \Delta n_{plasma}(E^{i+1}) - \frac{cn_o \pm_{FCA} N_f^{i+1/2} \Delta t}{2} - \frac{c^2 £_o n_o^2 \ _{TPA} \Delta t \left[\left| E^{i+1} \right|^2 + \left| E^{i} \right|^2 \right]}{8}.$$

(6.12)

Similar to Eq. 6.4, Eq. 6.10 must be solved with iteration. In the performed simulations, the maximum number of iterations was set to six to ensure accuracy without compromising simulation performance.

The material plugin was validated using a few simple tests of each of the nonlinear additions, the free-carrier generation, TPA, FCA and PDE, separately in a FDTD simulation of a SOI waveguide. After validating the rate equation (Eq. 6.6), a static free-carrier concentration was used to check the implementation of FCA and the PDE by first turning off TPA and then the other free carrier effect. The PDE was confirmed by comparing the speed of a pulse in the FDTD simulation with and without the PDE for a particular free-carrier concentration. The FDTD FCA was found to be equivalent to the equation $dI/dL = -\pm_{FCA} N_f I$ without the other effects. Similarly, the FDTD TPA was closely matched to $dI/dL = -\ _{TPA} I^2$ within a few iterations with the other effects turned off.

6.4 Results

The devices were characterized using a 400 fs FWHM pump pulse injected at the input port with energies up to 64 pJ and the device response was probed with a 400 fs FWHM 6.4 fJ probe pulse. Figure 6.2 (a) shows the electric field intensity

distribution of the probe pulse in Device A at the probe resonance at 1.53 µm, without the injection of the pump pulse. As the probe pulse is on resonance, a minimum of the probe pulse energy reaches the output port. When the pump pulse at 1.35 µm generates free carriers inside the nanoring, it causes a shift of the nanoring's resonant characteristics, thus moving the probe pulse 'off' resonance and away from the minimum transmission. The free-carrier concentration in the nanoring increases to its maximum within the first 400 fs after the pump pulse reaches the nanoring, and then decays with a 1 ps lifetime, causing the nanoring resonance to shift and revert back to its original state. Figure 6.2 (b) depicts the electric field intensity distribution of the probe pulse in Device A 400 fs after a 16.0 pJ pump pulse. Here, the free carriers generated in the nanoring by the pump pulse have shifted the probe pulse off resonance, greatly enhancing the transmission of the probe pulse.

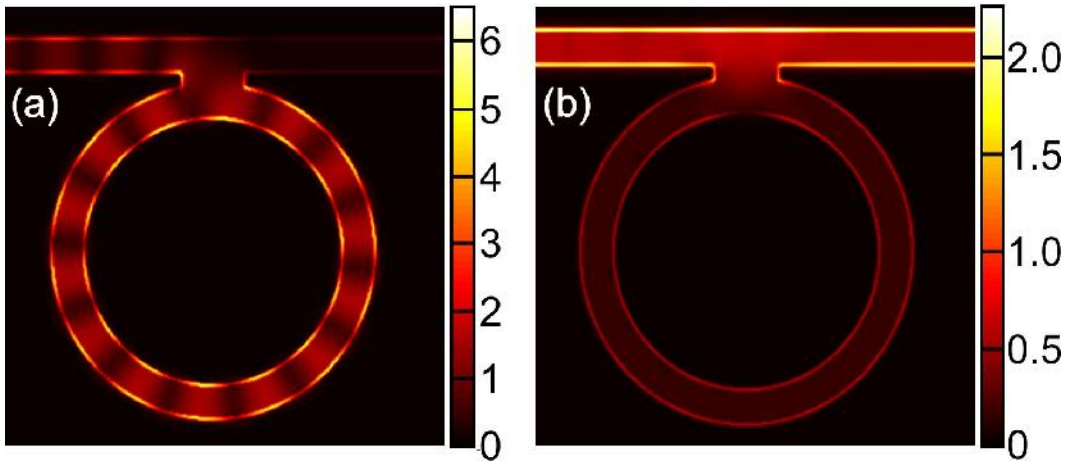

Figure 6.2: Electric field intensity plots for Device A with the 400 fs FWHM probe pulse centered at 1.53 µm (a) 'on' resonance and (b) 'off' resonance 400 fs after injection of a 16.0 pJ pump pulse at λ=1.35 µm.

The ultrafast responses of the devices under different pump energy excitations (5.8 pJ, 16.0 pJ and 31.3 pJ) is depicted in Figure 6.3. The maximum transmission is obtained with a 400 fs delay between the pump and probe pulses, as this is when the free-carrier concentration in the nanoring reaches its maximum value. The higher bandwidth of the resonances, and hence lower Q factors, associated with the smaller nanorings in Device A (pump at 1.35µm, probe at 1.53µm) and B (pump at 1.37µm, probe at 1.58µm) compared to Device C (pump at 1.44µm, probe at 1.55µm) result in more of the spectral contents of the probe pulses falling within their respective resonance's bandwidth. As shown in Figure 6.1 (f), Device C has a 51% narrower resonance than Device A. This leads to transmission minimums for Device A and B on the order of a few percent for the 'off' state, but a transmission minimum nearly an order of magnitude larger for Device C. For the pump energies used, the devices return to their original state within 3 ps, enabling modulation speeds of up to 333 GHz. By comparing the ultrafast responses of Devices A and B in Figure 6.3 (a) and Figure 6.3 (b), it is clear that the primary effect of the increased HfO_2 spacer layer thickness from 10 nm to 20 nm is to cause a reduction in the transmission maximum for the probe pulse at a given pump pulse energy.

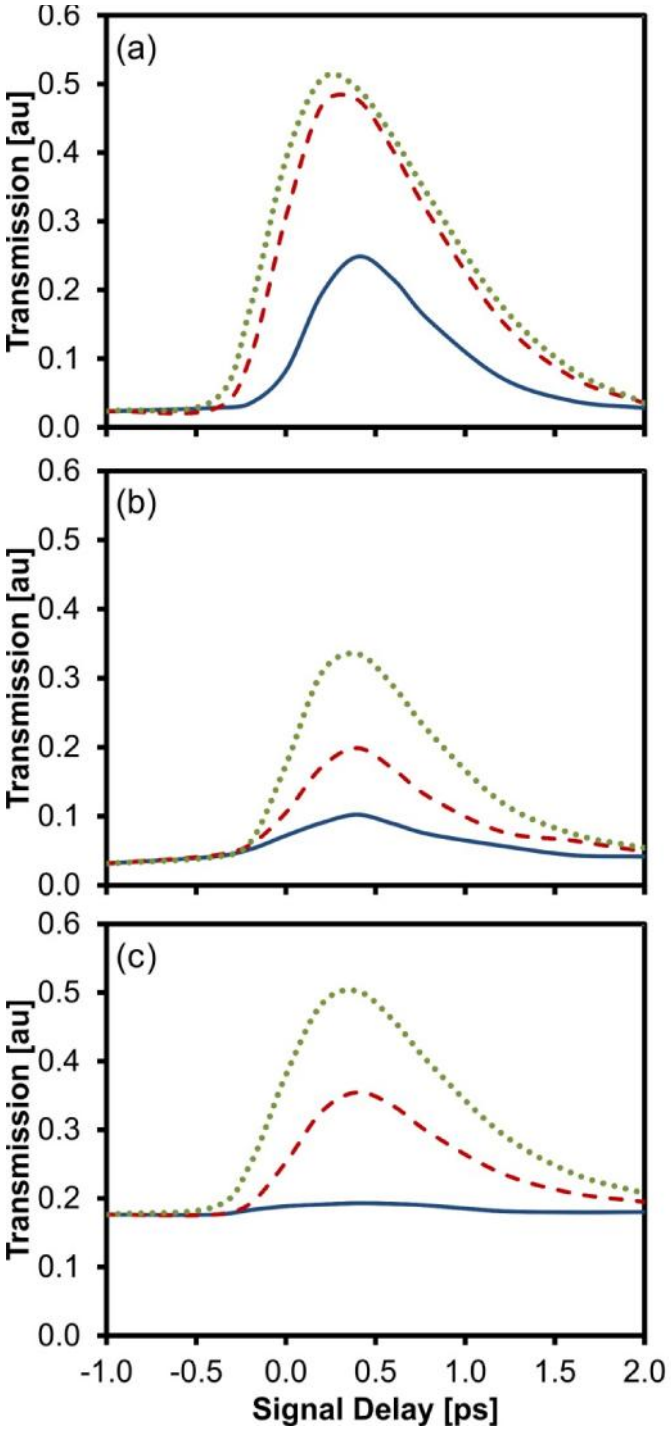

Figure 6.3: Normalized probe transmission as a function of the signal delay between pump and probe pulses for (a) Device A, (b) Device B, and (c) Device C at pump pulse energies of 5.8 pJ (blue solid line), 16.0 pJ (red dashed line) and 31.3 pJ (green dotted line).

Illustrated in Figure 6.4 are a number of different characteristics of the three devices at various pump pulse energies. Figure 6.4 (a) displays how the lower transmission minimum of Device A and B compared to Device C leads to a greater on-off modulation amplitude. In addition, since the thinner 10 nm HfO_2 spacer layer in Device A confines a greater percentage of the pump energy to the silicon core, Device A experiences a higher on-off modulation amplitude for a given pump pulse energy. For example, Device A experiences an on-off modulation amplitude of 13.1 dB compared to 8.8 dB for Device B for a 16.0 pJ pump pulse. As the pump pulse energy is increased above 31.3 pJ, the on-off modulation amplitude for Device A plateaus and decreases due to increased FCA and non-degenerate TPA between the pump and probe pulses. Figure 6.4 (b) shows that the rate of free-carrier concentration growth with pump pulse energy slows at higher energies as the pump begins to experience increased FCA from its leading edge. The resulting plateau behaviour for the maximum resonance shift of the nanorings at higher pump pulse energies is illustrated in Figure 6.4 (c). This plateau behaviour for the probe response is also brought on by the resonance shift experienced by the pump pulse. As the leading edge of the pump pulse shifts the pump resonance, the trailing edge does not couple to the ring, and the excess pump pulse energy is wasted. An important characteristic of any modulator is its switching time. Here the device's switching time is defined as the time over which the signal transmission reaches 3 dB over its 'off' state value. This characteristic is presented in Figure 6.4 (d), which shows that this value is very dependent on the ring geometry with the smaller rings experiencing longer

switching times due to their lower ‘off’ state transmission. Device A, for example, experiences an impressive 2.0 ps switching time at a pump pulse energy of only 16.0 pJ. Using an alternative definition of switching time, return to zero or RZ, the switching time increases only slightly to 2.5 ps.

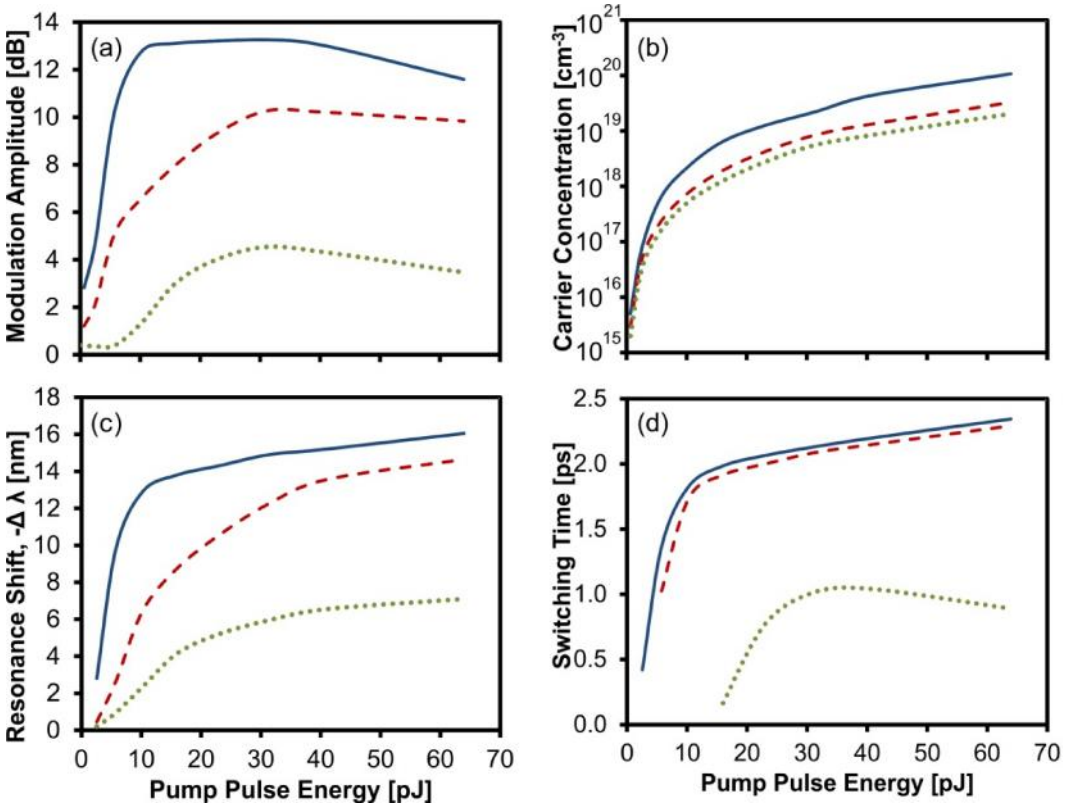

Figure 6.4: (a) Modulation amplitude, (b) maximum carrier concentration in the nanoring, (c) maximum resonance shift and (d) switching time as a function of pump pulse energy for the respective probe pulses of Device A (blue solid line), Device B (red dashed line) and Device C (green dotted line).

6.5 Conclusion

Ultrafast all-optical modulation in $Ag/HfO_2/Si/HfO_2/Ag$ MISIM nanoring resonators was investigated using self-consistent FDTD simulations incorporating TPA, FCA, and the PDE. Using a modest pump pulse energy of 16.0 pJ, a 13.1 dB modulation amplitude was obtained with a switching time of only 2 ps and a compact 1.4 μm^2 device footprint using Device A. Modulation amplitude is maximized for smaller nanorings due to the resulting broader device bandwidth. The energy required for modulation is minimized with thinner spacer layers. The required energy for modulation could be further reduced by utilizing shorter pump pulses provided pulses fit within the device bandwidth.

Chapter 6 References

[1] S. Zhu, G. Q. Lo, D. L. Kwong, “Phase modulation in horizontal metal-insulator-silicon-insulator-metal plasmonic waveguides,” Opt. Express **21**, 8320-8330 (2013).

[2] J. A. Dionne, K. Diest, L. A. Sweatlock, and H. A. Atwater, “PlasMOStor: a metal-oxide-Si field effect plasmonic modulator,” Nano Lett. **9**, 897–902 (2009).

[3] A. Y. Elezzabi, Z. Han, S. Sederberg, and V. Van, “Ultrafast all-optical modulation in silicon-based nanoplasmonic devices,” Opt. Express **17**, 11045–11056 (2009).

[4] J. N. Caspers, N. Rotenberg, and H. M. van Driel, “Ultrafast silicon-based active plasmonics at telecom wavelengths,” Opt. Express **18**, 19761–19769 (2010).

[5] S. Sederberg, D. Driedger, M. Nielsen, and A. Y. Elezzabi, “Ultrafast all-optical switching in a silicon-based plasmonic nanoring resonator,” Opt. Express **19**, 23494- 23503 (2011).

[6] K. F. MacDonald, Z. L. Sámson, M. I. Stockman, and N. I. Zheludev, “Ultrafast active plasmonics,” Nat. Photonics 3, 55–58 (2009).

[7] Q. Lin, O. J. Painter, and G. O. Agrawal, “Nonlinear optical phenomena in silicon waveguides: Modeling and applications,” Opt. Express **15**, 16604-16644 (2007).

[8] I. D. Rukhlenko, M. Premaratne, and G. P. Agrawal, "Nonlinear propagation in silicon-based plasmonic waveguides from the standpoint of applications," Opt. Express **19**, 206-217 (2011).

[9] F. E. Doany, D. Grischkowsky, and C. C. Chi, “Carrier lifetime versus ion-implantation dose in silicon on sapphire,” Appl. Phys. Lett. **50**, 460–462 (1987).

[10] P. B. Johnson and R. W. Christy, “Optical constants of the noble metals,” Phys. Rev. B **6**, 4370-4379 (1972).

[11] J. D. T. Kruschwitz and W. T. Pawlewicz, “Optical and durability properties of infrared transmitting thin films,” Appl. Opt. **36**, 2157-2159 (1997).

[12] E. D. Palik, *Handbook of Optical Constants of Solids,* (Academic Press, San Diego, 1998).

[13] N. Suzukim “FDTD analysis of two-photon absorption and free-carrier absorption in Si high-index-contrast waveguides,” J. Lightwave Technol. **25**, 2495-2501 (2007).

[14] M. Dinu, F. Quochi, and H. Garcia, “Third-order nonlinearities in silicon at telecom wavelengths,” Appl. Phys. Lett. **82**, 2954-2956 (2003).

[15] R. D. Kekatpure and M. I. Brongersma, “Near-infrared free-carrier absorption in silicon nanocrystals,” Opt. Lett. **34**, 3397-3399 (2009).

[16] R. A. Soref and B. R. Bennett, “Electrooptical effects in silicon,” IEEE J. Quantum Electron. **23**, 123-129 (1987).

Chapter 7

3-D Integration of Nanoplasmonic Circuits Utilizing Vertically Coupled Ring Resonators[6]

7.1 Background

A cornerstone of complementary metal-oxide-semiconductor (CMOS) electronics and a major difficulty in CMOS electronics fabrication, are the vias, vertical connections between device layers that allow for the overlaying of crossed electrical connections. A method of vertical 3-D integration will also be required for nanoplasmonic circuits if they are to play a major role in the next generation computing platform. Both an increase in synchronization and an overall reduction in circuit footprint are achieved through device layer stacking and 3-D integration. The high propagation losses in nanoplasmonic circuits due to ohmic absorption put an additional emphasis on the need for small device and

[6] *A version of this chapter has been published. M.Nielsen and A. Y. Elezzabi, Opt. Express **20**, 8592-8597 (2012).*

circuit footprints. However, vertical integration of nanoplasmonic circuits remains a relatively unexplored area of research. Numerous difficulties stand in the way of direct 3-D surface plasmon polariton signal routing including interference between waveguides [1], nonselective signal transfer, low coupling efficiencies [2], and signal polarization changes. Thus far, work on integrating plasmonic devices has primarily focused on planar integration utilizing laterally coupled nanoplasmonic waveguides [1]. One example of vertical integration of nanoplasmonic waveguides [2] examined the coupling between vertically stacked metal-insulator-metal (MIM) plasmonic waveguides. It was found that the coupling required micron scale distances on the same order of magnitude of the propagation length of the waveguides, limiting possible device size and maximum coupling efficiency. The simplicity of this coupling method also meant that it was not frequency-selective with respect to the propagating signal. Since every frequency component was coupled to the next device layer, the coupling scheme did not allow for the routing of specific wavelengths between device layers. Wavelength routing in this fashion is important for wavelength-division multiplexing (WDM) applications which form the backbone of many photonic systems.

This chapter explores the viability of a novel nanoplasmonic 3-D coupling platform capable of monolithic integration with current silicon-based CMOS technology. First, the frequency selective layer-to-layer coupling platform formed of vertically stacked plasmonic nanoring resonators is presented. The nanoring resonators and coupling waveguides are formed out of MIM waveguides to take

advantage of their high field confinement and low bending losses. The unique design of the 3-D interconnect platform enables it to overcome the constraints on minimum device size by having the signal transfer occur over multiple round trips within the resonator. The operation of coupling platform is examined through finite difference time domain (FDTD) simulations. Frequency selectivity via the device ports is obtained through the resonate nature of the stacked nanorings and can be tailored for specific frequencies by varying the radii of the rings. The advantage of this coupling scheme is that difference device layers could operate at different frequencies without crosstalk. An envisaged application would be a plasmonic analog to coarse WDM in conventional systems formed of stacked independent circuits for parallel processing.

7.2 Nanoplasmonic Coupling Platform Design

The presented 3-D nanoplasmonic coupling platform is formed primarily of vertically-stacked nanoring resonators. The vertical alignment of the identical nanorings enables strong electromagnetic coupling during resonance. Ag/Si/Ag MIM waveguides form the nanorings and their associated input/output waveguides. Silver's inherent low losses for plasmonic applications [3] made it an obvious choice for the metal component of the MIM waveguides. The silicon core enables efficient coupling between the device's MIM plasmonic I/O waveguides and conventional silicon nanophotonics waveguides and devices as well as nanoscale mode confinement. It also offers the potential for CMOS compatibility

with Si electronic components. The schematics of the five device variations under consideration are presented in Figure 7.1, with an illustrative 2-D representation of a two layer device from a perpendicular view to the signal input direction presented in Figure 7.1(a). The silicon core of the MIM waveguides have dimensions of $w_1 = h_1 = 100$ nm, with silver side wall of the same height and semi-infinite extent. The input/output waveguides enable evanescent signal coupling to and from the identically vertically stacked nanoring resonators through silver gaps of width $w_2 = 25$ nm. The entire device is submerged in SiO_2, thus acting as both the substrate and the cladding layers, with adjacent device layers separated by a cladding height of $h_2 = 100$ nm. In order to characterize the effect of varying the nanoring radius of device operation, the two-level device with parallel input and output waveguide, as depicted in Figure 7.1 (b), was examined for nanoring radii $r = 400$, 500, 560, and 600 nm. It should be noted that for $r = 560$ nm, the device has a compact planar device footprint of only 1.00 μm^2. As the orientation of the output waveguide versus the input waveguide is important, the device operation was characterized for the two level device with perpendicular input and output waveguides depicted in Figure 7.1 (c) for $r = 560$ nm. Three level devices with $r = 560$ nm were characterized with output waveguides opposite to the input waveguide as depicted in Figure 7.1 (d), above the input waveguide as depicted in Figure 7.1 (e), and both opposite and above the input waveguide as depicted in Figure 7.1 (f).

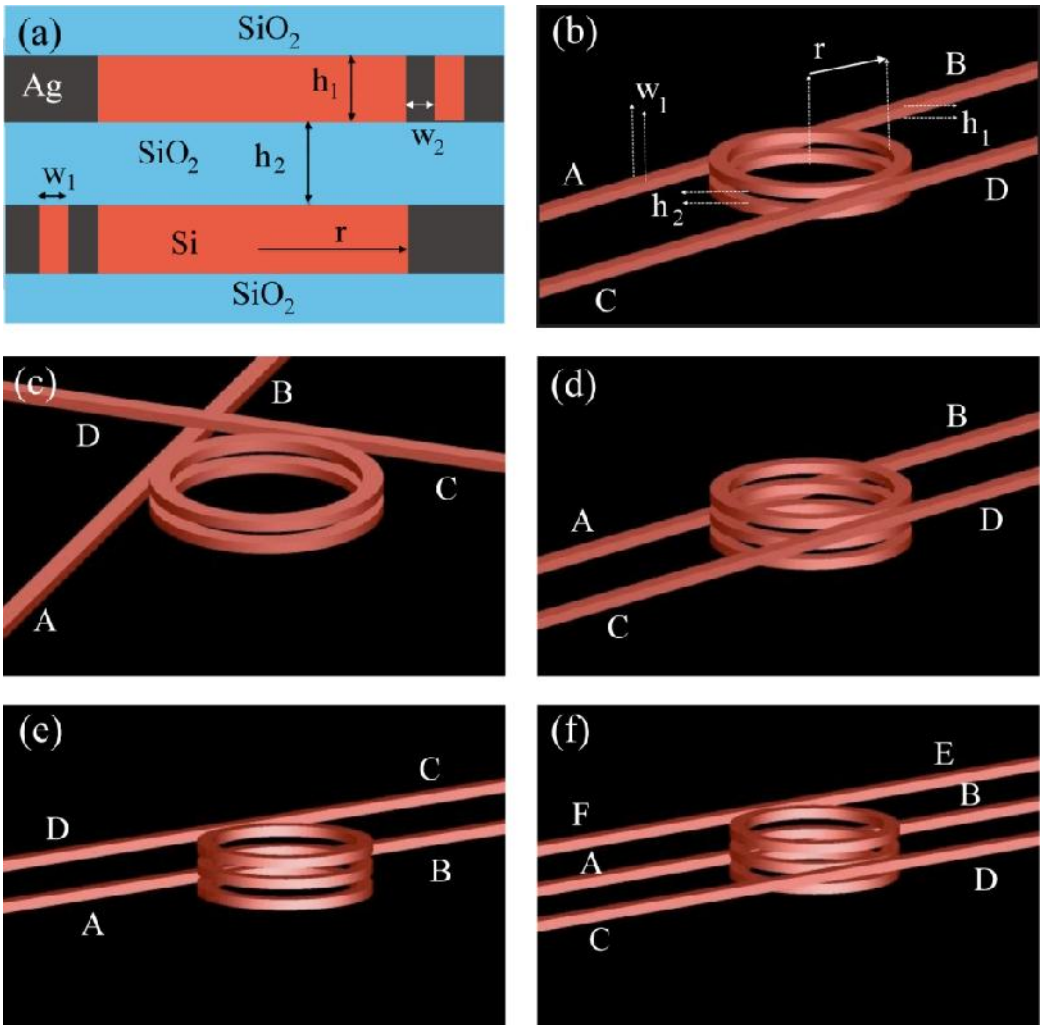

Figure 7.1: (a) Illustrative 2-D representation from perpendicular to the input signal injection direction of the vertically coupled nanoring resonators with parallel input and output waveguides and dimensions $w_1 = h_1 = h_2 = 100$ nm, $w_2 = 25$ nm, and nanorings radii r. Angled view absent the Ag and SiO_2 layers of (b) the device in Figure 7.1 (a), (c) two-level system with perpendicular input and output waveguides, and (d,e,f) three-level systems with various arrangements of the output waveguides. Other than output waveguide orientation, and number and radii of nanorings, all dimensions are constant throughout the devices. In all the above devices, the labeled ports are: input (A), throughput (B), drop (C,E), and add (D,F).

7.3 Device Operation

The operation of the devices depicted in Figure 7.1 were characterized using 3-D finite difference time domain (FDTD) simulations on the commercial software Lumerical FDTD Solutions using literature values for the frequency dependent complex refractive indices of silver [4], silicon [5], and silicon dioxide [5]. Further information on FDTD simulations using Lumerical FDTD Solutions can be found in Appendix B. A broadband pulse from 1.1 µm to 2.0 µm centered at 1.42 µm formed the input signal, with the corresponding mode shown in Figure 7.2 (a). This mode had a propagation loss of 0.55 dB/µm at the center wavelength of 1.42 µm, which corresponds to a propagation length of 7.82 µm. The mode is tightly confined to the Si core in the lateral direction by the silver sidewalls, and has a 1/e extent of only 30 nm into the SiO_2 cladding above and below the waveguide. The input signal was injected at the input port (port A in Figure 7.1) 1.00 µm from the center of the nanorings. The spectral characteristics, in the form of intensity versus wavelength, were measured 1.00 µm from the center of the nanorings at the throughput port (port B in Figure 7.1) and drop ports (ports C and E in Figure 7.1) for each device. The devices' spectral characteristics are presented in Figure 7.2 (b-f) and Figure 7.3.

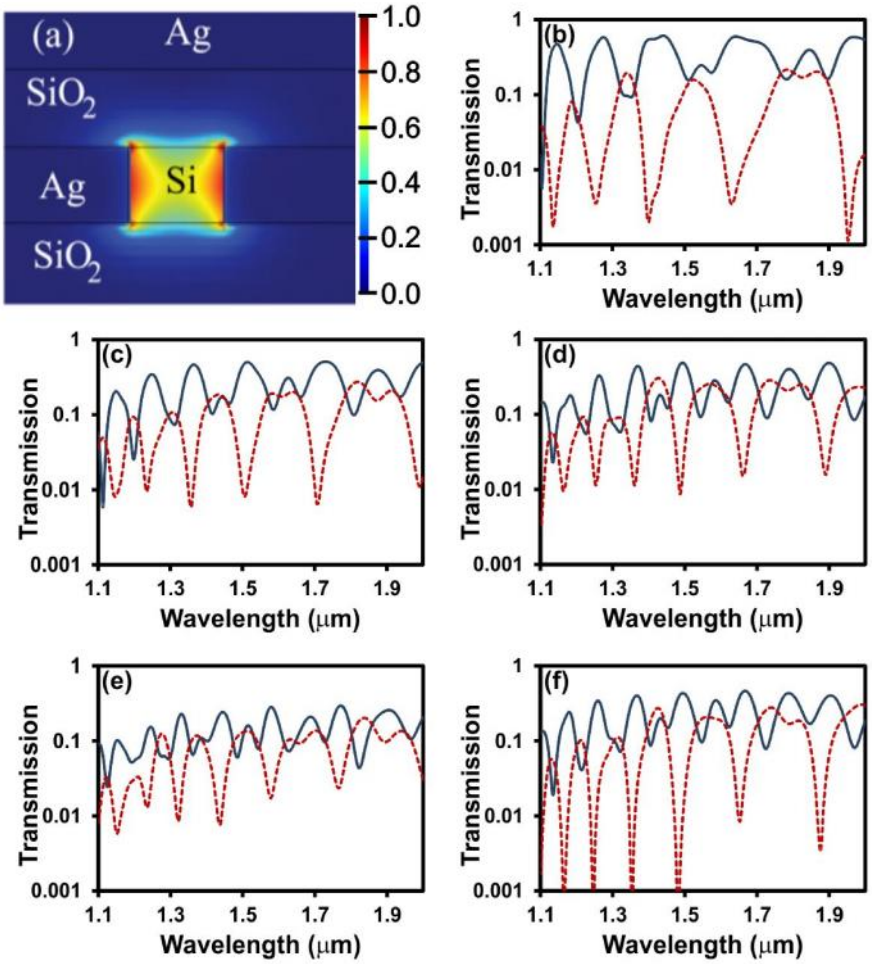

Figure 7.2: (a) Normalized electric field intensity profile for the fundamental TE mode of the Ag/Si/Ag MIM waveguide centered at a wavelength of 1.42 μm and measured at a distance of 1.00 μm from the center of the nanoring at port A. (b-f) Normalized transmission spectra at the throughput port B (blue solid line), and drop port C (red dashed line) for the two level device geometries depicted in Figure 7.1. (b) 400 nm, (c) 500 nm, (d) 560 nm, and (e) 600 nm nanorings radii, *r*, for the two level system with parallel input and output waveguides as depicted in Figure 7.1 (b). (f) Two-level system with perpendicular input and output waveguides and r = 560 nm as depicted in Figure 7.1 (c).

The effect of varying the radii of the vertically stacked nanorings on the devices' output intensity spectra was the first aspect of the devices' to be

characterized. Using the two-level system with parallel input and output waveguides as depicted in Figure 7.1 (b), the effect of varying the radii of the vertically stacked nanorings was investigated first to determine the optimum nanoring radius for the best interlayer coupling in the telecommunications band. Figure 7.2 (b-e) illustrates the output intensity spectra for this device as the radii varied from 400 nm to 600 nm. As expected for a resonant based device, the spectral peaks of the output intensity spectra at the throughput (B) and drop (C) ports shift with changing nanoring radii. While reducing the radii of the nanoring led to broader spectral peaks, the increased propagation losses from the longer radii led to smaller peak to trough spectral peaks. Both these competing factors have negative consequences for the devices' Q factors. The nanoring radius that corresponded to the highest output peak intensities and Q factors for both the throughput and drop ports was found to be r = 560 nm, with a Q factor of 30 for the throughput port at a wavelength of 1.5 μm and 20 at the drop port peak at a wavelength of 1.43 μm. The intensity at the drop port peak at 1.43 μm was 30% of that of the input intensity at that wavelength. After compensating for the propagation losses in the input and output waveguides, this corresponded to a coupling efficiency of 39%. The results at the nearest throughput port peak, at 1.5 μm, were comparable at 49% of the input intensity. True 3-D integration requires that the transmitted signal in the upper layer propagate in an arbitrary direction relative to that of the input signal. As such, the effect of changing the output waveguide orientation from parallel to perpendicular to the input waveguide, the device in Figure 7.1 (b) as opposed to the device in Figure 7.1 (c), was examined.

While the output waveguide could not be placed directly above the input waveguide without resulting in undesirable frequency independent coupling, a 560 nm radius 90° bend in the output waveguide after the 3-D nanoplasmonic coupling platform would provide access to all propagation directions at the cost of only 11% bending losses at the center wavelength of 1.42 μm. The change in output waveguide orientation, however, resulted in slightly lower output port peaks as depicted in the output intensity spectra in Figure 7.2 (f). The intensity at the drop port at 1.43 μm and at the throughput port at 1.5 μm was 27% and 42% of the input intensity, respectively, in this case. Despite the lower intensities, the Q factors at these peaks increased to 26 for 1.43 μm at the drop port and 35 for 1.5 μm at the throughput port.

Three level devices with r = 560 nm were studied in order to examine the effect of multilayer coupling on the signal transmission as the signal may be required to bypass a particular device layer. This method of signal transfer could also be used when the device layers are situated farther than 100 nm apart by placing additional vertically coupled nanorings between the device layers. The depicted device in Figure 7.1 (d) is identical to the device in Figure 7.1 (b) expect with the additional of a third device layer, and associated nanoring, between the input and output device layers. With addition of the third device layer, more coupling is required to transmit the signal, leading to the loading effect seen in the output intensity spectra in Figure 7.3 (a) where the spectral peaks above 1.6 μm shift to longer wavelengths and the maximum intensity of the output peaks decreases compared to the two level device. The intensity at the drop port at 1.43

μm and at the throughput port at 1.5 μm decreased to 17% and 44% of the input intensity, respectively, with Q factors of 20 at the drop port peak at 1.43 μm and 30 at the throughput port at 1.5 μm. Changing the location of the output waveguide from the opposite the input waveguide to above the input waveguide, Figure 7.1 (d) to Figure 7.1 (e), does not cause significant change in the throughput port spectra or the drop port spectra between 1.3 μm and 1.7 μm. It does, however, enable the output waveguide to access a different direction without resorting to bending the waveguide and the associated bending losses. The result of this change in output waveguide location is depicted in Figure 7.3 (b). A second output waveguide coupled to the nanoring in the middle device, as depicted in Figure 7.1 (f) and results shown in Figure 7.3 (c), causes ~50% attenuation in the output intensity spectra for drop port E without shifting the spectral peaks. Below 1.5 μm, the intensity peaks for drop ports C and E occur at the same wavelength for this device, thus allowing for the signal to be transmitted to multiple device layers simultaneously.

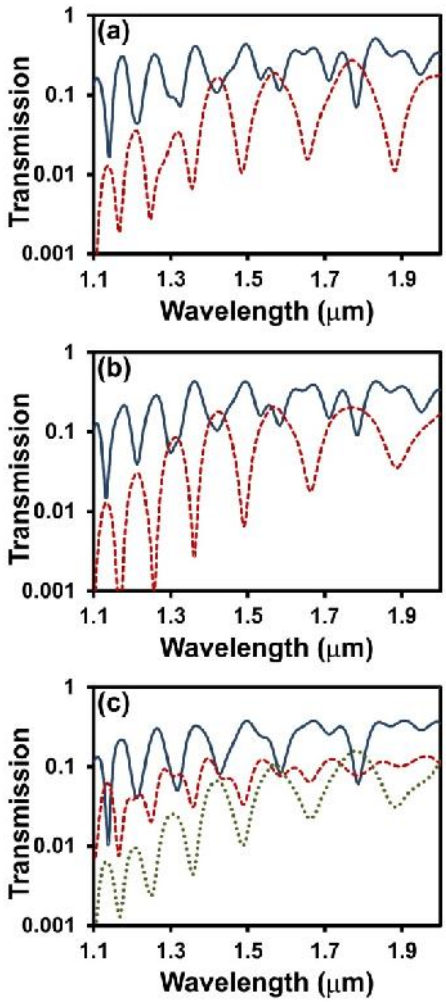

Figure 7.3: Transmission spectra at the throughput port B (blue solid line), and drop ports C (red dashed line) and E (green dotted line) for the three-level device geometries depicted in Figure 7.1. (a) Three-level system with 560 nm nanoring radii, *r*, as depicted in Figure 7.1 (d). (b) Three-level system with r = 560 nm as depicted in Figure 7.1 (e). (c) Three-level system with r = 560 nm as depicted in Figure 7.1 (f).

7.4 Conclusion

The presented silicon based nanoplasmonic 3-D coupling platform is shown to be capable of frequency selective signal transfer between device layers in the

telecommunication band. Vertically coupled nanoring resonators formed of Ag/Si/Ag provided inter-layer coupling efficiencies as high as 39% with Q factors as high as 35. The resonant characteristics of the devices, and thus frequency selectivity, were shown to be tunable through varying the nanoring radii.

Chapter 7 References

[1] G. Veronis and S. Fan, "Crosstalk between three-dimensional plasmonic slot waveguides," Opt. Express **16**, 2129-2140 (2008).

[2] G. B. Hoffman and R. M. Reano, "Vertical coupling between gap plasmon waveguides," Opt. Express **16**, 12677-12687 (2008).

[3] P. West, S. Ishii, G. Naik, N. Emani, V. Shalaev, and A. Boltasseva, "Searching for better plasmonic materials," Laser Photonics Rev. **4**, 795-808 (2010).

[4] P. B. Johnson and R. W. Christy, "Optical Constants of Noble Metals," Phys. Rev. B **6**, 4370-4379 (1972).

[5] E. D. Palik, *Handbook of Optical Constants of Solids*, (Academic Press, San Diego, 1998).

.

Chapter 8

Conclusion

8.1 Summary

The first step in creating integrated all-optical plasmonic nanocircuitry is the development of reliable nanoplasmonic waveguides for interconnect applications. Nanoplasmonic waveguides are also essential in the development of resonant devices for modulators on the same waveguiding platform. To this end, hybrid nanoplasmonic waveguides and waveguide ring resonators on the metal-insulator-semiconductor-insulator-metal (MISIM) platform were designed, fabricated, and characterized. The silicon based waveguides were fabricated using several different metal claddings, Ag, Au and Cu, and insulators, HfO_2 and SiO_2, in order to analyze the effect of different materials and fabrication processes on the waveguide properties. The waveguides were integrated with standard silicon-on-insulator photonic waveguides. An experimental setup was designed and built for the purpose of characterizing the nanoplasmonic waveguides and resonant devices. The experimental propagation length and coupling efficiency at 1.55 μm for each choice of metal cladding and insulator were compared to theoretical results derived from bulk material data. For future modeling applications, new

refractive index values were suggested for each of the metals. No significant resonances were discovered for MISIM waveguide ring resonators of radii up to 1 μm.

Another class of hybrid nanoplasmonic waveguides, metal-insulator-semiconductor (MIS) waveguides was studied in order to develop effective plasmonic resonant devices. Au/SiO_2/Si MIS nanoplasmonic waveguides were designed for a long propagation length, fabricated on a silicon-on-insulator platform, and characterized for both propagation length and coupling efficiency to standard silicon-on-insulator photonic waveguides. The experimental properties of these hybrid nanoplasmonic waveguides were used to design Bragg reflector resonators. The realized broadband transmission of several different designs were compared to theoretical predictions and presented alongside the results from a micro disk resonator. Quality factors upwards of 64.4 were found for the Bragg reflector resonators in a compact device footprint of 1.5 μm^2.

High propagation losses plague many of the most intriguing plasmonic device applications, including plasmonic interconnects for high integration density optical signal routing. A possible solution is the introduction of gain into plasmonic interconnect networks. This possibility was explored through integrating an electrically pumped MISIM nanoplasmonic $In_{0.485}Ga_{0.515}As$ amplifier design into an interconnect network and studying the effect on the optical signals carried by the network. Nonlinear 3-D FDTD simulations were used to model the amplifier using a rate equations model, which is validated through comparison to a conventional semiconductor optical amplifier model.

Fully integrated all-optical plasmonic circuitry requires a plasmonic analogue to the electronic transistor capable of ultrafast signal modulation on a silicon-on-insulator platform. To this end, all-optical modulation in plasmonic nanocircuitry was investigated through free carrier generation in a silicon-based MISIM nanoring resonator. The free carriers, generated through two photon absorption of a high intensity pump pulse, alter the resonant characteristics of the nanoring as seen by a probe pulse. Nonlinear 3-D FDTD simulations were used to study the modulation characteristics of three separate devices.

Signal routing in conventional electronics requires vertical connections between device layers to allow for the overlay of crossed electrical connections. Plasmonic circuitry will require an analogue to these vertical connections, known as vias in order to be competitive with conventional electronic circuitry. A method to achieving 3-D signal routing in plasmonic nanocircuitry is explored using vertically coupled MIM nanoring resonators to achieve frequency selective signal transfer between device layers. 3-D FDTD simulations are utilized to study the effect of the nanoring radii and bus waveguide orientation on the device characteristics.

8.2 Future Directions

With the success of the Au/SiO_2/Si hybrid nanoplasmonic waveguides and resonant devices described in Chapter 4, further work is necessary to explore this device platform for integrated SOI-based optical circuit applications. The full

range of passive devices, including bends, splitters, directional couplers, interferometers and rings resonators, must still be fabricated and characterized. In addition, the already characterized resonant devices, the Bragg reflector resonators and disk resonator, are ready to be developed into all-optical modulators. By fabricating the devices without the photonic I/O waveguides and cleaving the samples with MIS waveguide end facets using techniques developed in the Ultrafast Optics and Nanophotonics Laboratory by Shawn Sederbereg, an end fired 1550 nm ultrafast pulsed laser can be aligned to the end facets using free space optics. The high intensity pulses will modulate the resonant characteristics of the devices as seen by a CW signal via free carriers generated from two photon absorption in silicon. The free carrier recombination lifetime in the silicon can be reduced from the nanosecond scale to under a picosecond using already acquired oxygen ion doped SOI wafers in order to obtain ultrafast modulation speeds. The results of these experiments can be compared to FDTD simulations using the established silicon TPA plugin from Chapter 6 in order to improve upon the designs. This will lead to the possibility of developing a fully integrated all-optical plasmonic logic gate based on Au/SiO_2/Si MIS waveguides.

Appendices

Appendix A: Wavelength Scan Program

For characterizing the broadband operation of the devices studied in Chapters 3 and 4 of this thesis using the experimental setup described in Chapter 2 of this thesis, a Matlab program initially written by Shawn Sederberg of the UONL called *Laser_Scan.m* was utilized. The program allows one to select the start and stop wavelength of a wavelength scan in steps as fine as 0.01 nm. While the output of a device is connected to the Yokogawa AQ6370C OSA, the program steps the output of the Velocity^{TM} Tunable Diode Laser between the specified start and stop wavelengths in the determined steps and records the output from the OSA. Since the program normalizes the power at each wavelength to the laser output after using *Laser_Scan.m*, the measurements must be renormalized to the power measured using the infrared power detector at a central wavelength of the scan. In addition, the overlaying Fabry-Pérot resonances from the cleaved end facets would have to be averaged out of the final data set.

Laser_Scan.m

```
function varargout = Laser_Scan(varargin)
% LASER_SCAN M-file for Laser_Scan.fig
%      LASER_SCAN, by itself, creates a new LASER_SCAN or raises the
existing
%      singleton*.
```

```
%
%      H = LASER_SCAN returns the handle to a new LASER_SCAN or the
handle to
%      the existing singleton*.
%
%      LASER_SCAN('CALLBACK',hObject,eventData,handles,...) calls the local
%      function named CALLBACK in LASER_SCAN.M with the given input
arguments.
%
%      LASER_SCAN('Property','Value',...) creates a new LASER_SCAN or raises
the
%      existing singleton*.  Starting from the left, property value pairs are
%      applied to the GUI before Laser_Scan_OpeningFcn gets called.  An
%      unrecognized property name or invalid value makes property application
%      stop.  All inputs are passed to Laser_Scan_OpeningFcn via varargin.
%
%      *See GUI Options on GUIDE's Tools menu.  Choose "GUI allows only one
%      instance to run (singleton)".
%
% See also: GUIDE, GUIDATA, GUIHANDLES

% Edit the above text to modify the response to help Laser_Scan

% Last Modified by GUIDE v2.5 23-Jun-2011 13:36:18

% Begin initialization code - DO NOT EDIT
gui_Singleton = 1;
gui_State = struct('gui_Name',       mfilename, ...
                   'gui_Singleton',  gui_Singleton, ...
                   'gui_OpeningFcn', @Laser_Scan_OpeningFcn, ...
                   'gui_OutputFcn',  @Laser_Scan_OutputFcn, ...
                   'gui_LayoutFcn',  [] , ...
                   'gui_Callback',   []);
if nargin && ischar(varargin{1})
   gui_State.gui_Callback = str2func(varargin{1});
end

if nargout
   [varargout{1:nargout}] = gui_mainfcn(gui_State, varargin{:});
else
   gui_mainfcn(gui_State, varargin{:});
end
% End initialization code - DO NOT EDIT


% --- Executes just before Laser_Scan is made visible.
```

```
function Laser_Scan_OpeningFcn(hObject, eventdata, handles, varargin)
% This function has no output args, see OutputFcn.
% hObject    handle to figure
% eventdata  reserved - to be defined in a future version of MATLAB
% handles    structure with handles and user data (see GUIDATA)
% varargin   command line arguments to Laser_Scan (see VARARGIN)

% Choose default command line output for Laser_Scan
handles.output = hObject;

% Update handles structure
guidata(hObject, handles);

% UIWAIT makes Laser_Scan wait for user response (see UIRESUME)
% uiwait(handles.F);


% --- Outputs from this function are returned to the command line.
function varargout = Laser_Scan_OutputFcn(hObject, eventdata, handles)
% varargout  cell array for returning output args (see VARARGOUT);
% hObject    handle to figure
% eventdata  reserved - to be defined in a future version of MATLAB
% handles    structure with handles and user data (see GUIDATA)

% Get default command line output from handles structure
varargout{1} = handles.output;



function lambda_min_Callback(hObject, eventdata, handles)
% hObject    handle to lambda_min (see GCBO)
% eventdata  reserved - to be defined in a future version of MATLAB
% handles    structure with handles and user data (see GUIDATA)

% Hints: get(hObject,'String') returns contents of lambda_min as text
%        str2double(get(hObject,'String')) returns contents of lambda_min as a
double

input = str2num(get(hObject,'String'));

if(isempty(input))
   set(hObject,'String','1550.00');
end
guidata(hObject, handles);
```

```
% --- Executes during object creation, after setting all properties.
function lambda_min_CreateFcn(hObject, eventdata, handles)
% hObject    handle to lambda_min (see GCBO)
% eventdata  reserved - to be defined in a future version of MATLAB
% handles    empty - handles not created until after all CreateFcns called

% Hint: edit controls usually have a white background on Windows.
%       See ISPC and COMPUTER.
if ispc && isequal(get(hObject,'BackgroundColor'),
get(0,'defaultUicontrolBackgroundColor'))
   set(hObject,'BackgroundColor','white');
end



function lambda_step_Callback(hObject, eventdata, handles)
% hObject    handle to lambda_step (see GCBO)
% eventdata  reserved - to be defined in a future version of MATLAB
% handles    structure with handles and user data (see GUIDATA)

% Hints: get(hObject,'String') returns contents of lambda_step as text
%        str2double(get(hObject,'String')) returns contents of lambda_step as a
double

input = str2num(get(hObject,'String'));

if(isempty(input))
   set(hObject,'String','1.0');
end
guidata(hObject, handles);


% --- Executes during object creation, after setting all properties.
function lambda_step_CreateFcn(hObject, eventdata, handles)
% hObject    handle to lambda_step (see GCBO)
% eventdata  reserved - to be defined in a future version of MATLAB
% handles    empty - handles not created until after all CreateFcns called

% Hint: edit controls usually have a white background on Windows.
%       See ISPC and COMPUTER.
if ispc && isequal(get(hObject,'BackgroundColor'),
get(0,'defaultUicontrolBackgroundColor'))
   set(hObject,'BackgroundColor','white');
end
```

```
function lambda_max_Callback(hObject, eventdata, handles)
% hObject    handle to lambda_max (see GCBO)
% eventdata  reserved - to be defined in a future version of MATLAB
% handles    structure with handles and user data (see GUIDATA)

% Hints: get(hObject,'String') returns contents of lambda_max as text
%        str2double(get(hObject,'String')) returns contents of lambda_max as a
double

input = str2num(get(hObject,'String'));

if(isempty(input))
   set(hObject,'String','1560.00');
end
guidata(hObject, handles);


% --- Executes during object creation, after setting all properties.
function lambda_max_CreateFcn(hObject, eventdata, handles)
% hObject    handle to lambda_max (see GCBO)
% eventdata  reserved - to be defined in a future version of MATLAB
% handles    empty - handles not created until after all CreateFcns called

% Hint: edit controls usually have a white background on Windows.
%       See ISPC and COMPUTER.
if ispc && isequal(get(hObject,'BackgroundColor'),
get(0,'defaultUicontrolBackgroundColor'))
   set(hObject,'BackgroundColor','white');
end



function N_Callback(hObject, eventdata, handles)
% hObject    handle to N (see GCBO)
% eventdata  reserved - to be defined in a future version of MATLAB
% handles    structure with handles and user data (see GUIDATA)

% Hints: get(hObject,'String') returns contents of N as text
%        str2double(get(hObject,'String')) returns contents of N as a double

input = str2num(get(hObject,'String'));

if(isempty(input))
   set(hObject,'String','1');
end
```

```
guidata(hObject, handles);


% --- Executes during object creation, after setting all properties.
function N_CreateFcn(hObject, eventdata, handles)
% hObject    handle to N (see GCBO)
% eventdata  reserved - to be defined in a future version of MATLAB
% handles    empty - handles not created until after all CreateFcns called

% Hint: edit controls usually have a white background on Windows.
%       See ISPC and COMPUTER.
if ispc && isequal(get(hObject,'BackgroundColor'),
get(0,'defaultUicontrolBackgroundColor'))
   set(hObject,'BackgroundColor','white');
end

function Filename_Callback(hObject, eventdata, handles)
% hObject    handle to Filename (see GCBO)
% eventdata  reserved - to be defined in a future version of MATLAB
% handles    structure with handles and user data (see GUIDATA)

% Hints: get(hObject,'String') returns contents of Filename as text
%        str2double(get(hObject,'String')) returns contents of Filename as a double

input = get(hObject,'String');

if(isempty(input))
   set(hObject,'String','tst');
end
guidata(hObject, handles);


% --- Executes during object creation, after setting all properties.
function Filename_CreateFcn(hObject, eventdata, handles)
% hObject    handle to Filename (see GCBO)
% eventdata  reserved - to be defined in a future version of MATLAB
% handles    empty - handles not created until after all CreateFcns called

% Hint: edit controls usually have a white background on Windows.
%       See ISPC and COMPUTER.
if ispc && isequal(get(hObject,'BackgroundColor'),
get(0,'defaultUicontrolBackgroundColor'))
   set(hObject,'BackgroundColor','white');
end
```

```
% --- Executes on button press in execute_scan.
function execute_scan_Callback(hObject, eventdata, handles)
% hObject    handle to execute_scan (see GCBO)
% eventdata  reserved - to be defined in a future version of MATLAB
% handles    structure with handles and user data (see GUIDATA)

instrfind;
delete(ans);

lambda_min = get(handles.lambda_min,'String');
lambda_step = get(handles.lambda_step,'String');
lambda_max = get(handles.lambda_max,'String');
N = get(handles.N,'String');
Filename = get(handles.Filename,'String');

lambda = str2num(lambda_min):str2num(lambda_step):str2num(lambda_max);

laser=serial('COM3');
set(laser,'BaudRate',9600);
fopen(laser);
set(laser,'Terminator','CR')
set(laser,'Timeout',60)

fprintf(laser,'@*IDN?')
out = fscanf(laser);

osa=serial('COM4');
set(osa,'BaudRate',9600);
fopen(osa);
set(osa,'Terminator','CR/LF')
set(osa,'Timeout',60)

fprintf(osa,'*IDN?')
out = fscanf(osa);


[x,y] = size(lambda);
wavelength = str2num(lambda_max)*1e-9*ones(1,y);
amplitude = zeros(1,y);

command = [':SENSE:AVERAGE:COUNT ' str2num(N)];
fprintf(osa,command)

% for bb = 1:3
%     command = ['@WAVE' num2str(lambda(1))];
```

```
%     fprintf(laser,command)
%     fprintf(laser,'@WAVELENGTH?')
%     fprintf(laser,'@SENS:POW:FRON')
%
%     command = [':SENSE:WAVELENGTH:CENTER ' num2str(lambda(1)-.94)
'NM'];
%     fprintf(osa,command)
%     fprintf(osa,':SENSE:WAVELENGTH:SPAN 3.0NM')
%     fprintf(osa,':INITIATE')
%
%     fprintf(osa,':CALCULATE:MARKER:MAXIMUM')
%     fprintf(osa,':CALCULATE:MARKER:X? 0')
%
%     fprintf(osa,':CALCULATE:MARKER:MAXIMUM')
%     fprintf(osa,':CALCULATE:MARKER:Y? 0')
% end
%
for a = 1:y

    command = ['@WAVE' num2str(lambda(a))];
    fprintf(laser,command)
    out = fscanf(laser);
    fprintf(laser,'@WAVELENGTH?')
    out = fscanf(laser);
    fprintf(laser,'@SENS:POW:FRON')
    temp1 = fscanf(laser);

    command = [':SENSE:WAVELENGTH:CENTER ' num2str(lambda(a)-.94)
'NM'];
    fprintf(osa,command)
    fprintf(osa,':SENSE:WAVELENGTH:SPAN 3.0NM')
    fprintf(osa,':INITIATE')

    fprintf(osa,':CALCULATE:MARKER:MAXIMUM')
    fprintf(osa,':CALCULATE:MARKER:X? 0')
    temp = fscanf(osa);
    wavelength(a) = str2num(temp);

    fprintf(osa,':CALCULATE:MARKER:MAXIMUM')
    fprintf(osa,':CALCULATE:MARKER:Y? 0')
    temp = fscanf(osa);
    amplitude(a) = str2num(temp)/str2num(temp1);
    set(handles.lambda_current,'String',num2str(lambda(a)));
    guidata(hObject, handles);

    axes(handles.axes1)
```

```
    plot(wavelength,amplitude)
    drawnow()

end

savefile = [Filename '.mat'];
save(savefile,'wavelength','amplitude')


fclose(laser)
delete(laser)
clear laser;

fclose(osa)
delete(osa)
clear osa;
```

Appendix B: Material Plugins for Lumerical FDTD Solutions

The devices and waveguides described in this thesis were designed using the aid of the commercial software Lumerical FDTD Solutions after it was determined to run more than 10 times faster than self-written in-house 2-D finite difference time domain (FDTD) code. Lumerical FDTD Solutions solves Maxwell's curl equations in linear, isotropic and anisotropic, dispersive, and lossy materials in 2-D and 3-D Cartesian space according to the Yee discretization algorithm [1]. This involves solving update equations for the six components of the electromagnetic fields on a numerical grid with second-order accuracy. Further information on the FDTD method can be found in [2]. The frequency dependent complex refractive indices of materials are calculated using a multi-coefficient model to fit to the material parameters found in the literature. However, Lumerical FDTD Solutions does not come with built in non-linear materials. Instead, a plugin function was developed to enable users to add additional functionality to the software through a nonlinear polarization term. As one of the first users to explore the plugin option for Lumerical FDTD Solutions, I worked closely with Lumerical to develop the plugin software. As such, the plugin format underwent numerous generations to debug various issues. The plugin calculates the components of the electric field, *E*, based on a polarization from the user calculated in the plugin, linear material properties included in the

software, and the electric displacement field, *D*, calculated through Ampère's Law.

Following are the two nonlinear material plugins developed for the devices in Chapters 4 and 5, saturablegainnielsen and SiTPA, as written in C++. The first, saturablegainnielsen, describes a 4-level laser system with homogenous broadening, saturable gain, an undepleteable ground state, and electrically pumped, with $In_{0.485}Ga_{0.515}As$ as the gain medium. SiTPA incorporates the nonlinear phenomena of two photon absorption (TPA) and the free carrier effects of free carrier absorption and plasma dispersion in silicon.

1. *saturablegainnielsen*

immaterialplugin.h

```
#ifndef _IMATERIALPLUGIN_H
#define _IMATERIALPLUGIN_H

#include <string>
#include <vector>

#ifdef WIN32
#define DLLEXPORT __declspec(dllexport)
#else
#define DLLEXPORT
#endif

/*!
   \brief The interface class definition for a material plugin for FDTD Solutions

   This pure abstract class defines the methods that must be implemented to create a plugin material in FDTD Solutions. A class that inherits from this interface class and implements all the methods can be compiled into a dynamic library that can be loaded into FDTD Solutions to define new materials.
*/

class IMaterialPlugin
```

```
{
public:
   typedef std::vector< std::vector<double> > ParameterVector;
   virtual ~IMaterialPlugin(){};
   virtual std::string name() const = 0;
   virtual std::string uniqueId() const = 0;
   virtual std::vector<std::string> parameterNames() const = 0;
   virtual float calculateEx( float U, float V, float Ex, float* storage) = 0;
   virtual float calculateEy( float U, float V, float Ey, float* storage) = 0;
   virtual float calculateEz( float U, float V, float Ez, float* storage) = 0;
   virtual void initialize(const ParameterVector& parameters, double dt) = 0;
   virtual size_t storageSizeE() const = 0;

};

class IMagneticMaterialPlugin : public IMaterialPlugin
{
public:
   virtual float calculateHx( float U, float V, float Ex, float* storage) = 0;
   virtual float calculateHy( float U, float V, float Ey, float* storage) = 0;
   virtual float calculateHz( float U, float V, float Ez, float* storage) = 0;
   virtual size_t storageSizeH() const = 0;
};
#endif
```

saturablegainnielsen.h

```
#ifndef _SATURABLE_GAIN_NIELSEN_H
#define _SATURABLE_GAIN_NIELSEN_H

#include "imaterialplugin.h"
#include <vector>

class SaturableGainNielsenMaterialPlugin : public IMaterialPlugin
{
public:
   SaturableGainNielsenMaterialPlugin();
   virtual ~SaturableGainNielsenMaterialPlugin();

   std::string name() const {return "Saturable Gain (Nielsen)";};
   std::string uniqueId() const {return "{44E37201-1892-4312-9F5B-
7BE042143910}";};
   std::vector<std::string> parameterNames() const;
   float calculateEx( float U, float V, float Ex, float* storage);
   float calculateEy( float U, float V, float Ey, float* storage);
   float calculateEz( float U, float V, float Ez, float* storage);
```

```
   void initialize(const ParameterVector& parameters, double dt);
   size_t storageSizeE() const {return 11;};

   /* storage is, in this order:
      N1;
      N2;
      N2_n;
      dN;
      E_n;
      P;
      P_n;
      P_n1;
      firstUpdateDone;
      N3;
      N3_n;

   */

private:
   float calculateE( int axis, float U, float V, float E, float &N1, float &N2, float
&N2_n, float &dN, float &E_n, float &P, float &P_n, float &P_n1, float
&firstUpdateDone, float &N3, float &N3_n);
   //physical constants
         static float c;
         static float e0;
         static float h;
         static float pi;
         static float a10;
         static float a21;
         static float a32;
         static float a31;
         static float a30;
         static float del_lambda;
         static float lambda0;
         static float g;
         float dt;
         float er[3];
         double r3[3];
         float r1[3];
         float r2[3];
         float a20[3];
         float Ip[3];
         float w0;
         float del_w;
         float N2max[3];
```

```
        bool saveData;
        std::vector<float> data;
        std::vector<float> data1;
        std::vector<float> data2;
};

#endif
```

saturablegainnielsen.cpp

```
#include "saturablegainnielsen.h"
#include <cmath>
#include <fstream>
#include <iostream>
using namespace std;

/*!
   \class SaturableGainNielsenMaterialPlugin
   4 level gain system with homogeneously broadened gain starting at full inversion, but with saturation effects. Valid for lambda0>>del_lambda (narrow gain spectrum)
   Assumes undepletable ground state and electrical pumping. Everything is in standard SI units. Most variables have been put as constants for In0.485Ga0.515As gain medium.


*/

float SaturableGainNielsenMaterialPlugin::c = 2.99792458e8f; //speed of light
float SaturableGainNielsenMaterialPlugin::e0 = 8.854187817e-12f; //permittivity of vaccum
float SaturableGainNielsenMaterialPlugin::h = 6.62606957e-34f; //Plank's constant
float SaturableGainNielsenMaterialPlugin::pi  = 3.1415926535897931f; //pi
float SaturableGainNielsenMaterialPlugin::a10 = 1e13f; //lower laser level to ground state tranisition rate [s^-1]
float SaturableGainNielsenMaterialPlugin::a21 = 1e9f; //uper laser level to lower laser level tranisition rate [s^-1]
float SaturableGainNielsenMaterialPlugin::a32 = 1e13f; //pump laser level to upper state tranisition rate [s^-1]
float SaturableGainNielsenMaterialPlugin::a31 = 0f; //pump laser level to lower state tranisition rate [s^-1]
float SaturableGainNielsenMaterialPlugin::a30 = 0f; //pump laser level to ground state tranisition rate [s^-1]
```

```
float SaturableGainNielsenMaterialPlugin::del_lambda = 50e-9f; //gain medium
bandwidth [m]
float SaturableGainNielsenMaterialPlugin::lambda0 = 1.55e-6f; //center
wavelength of gain spectrum [m]
float SaturableGainNielsenMaterialPlugin::g = 2.582f; //degeneracy of upper laser
level to lower laser level ratio



std::vector<std::string> SaturableGainNielsenMaterialPlugin::parameterNames()
const
{
   std::vector<std::string> names(7);
   names[0] = "\xcf\x87 1";
   names[1] = "Source Peak Intensity [W/m^2]";
   names[2] = "Pump Level Pump Rate [m^-3 s^-1]";
   names[3] = "Lower Laser Level Pump Rate [m^-3 s^-1]";
   names[4] = "Upper to Ground State Recombination Rate [s^-1]";
   names[5] = "Save Data";
   names[6] = "Upper Laser Level Pump Rate [m^-3 s^-1]";


   return names;
}

void SaturableGainNielsenMaterialPlugin::initialize(const ParameterVector&
parameters, double dt_fdtd)
{
   dt = float(dt_fdtd);

   for(int i=0; i<3; i++){
      er[i] = 1.f+float(parameters[0][i]); //relative permittivity of gain medium
      Ip[i] = float(parameters[1][i]); //intensity of source
      r3[i] = double(parameters[2][i]);
      r1[i] = float(parameters[3][i]);
      a20[i] = float(parameters[4][i]);
      r2[i] = float(parameters[6][i]);


      w0 = 2*pi*c/lambda0;
      del_w = 2*pi*del_lambda*c/(lambda0*lambda0);
      N2max[i] = r3[i]*1.f/(a20[i]+a21)-g*(r1[i]+(a21/(a21+a20[i]))*r3[i])/a10;
//system starts at maximum inversion
```

```
		saveData = parameters[5][0] != 0.; //Used to output plugin
variables to examination
		data.reserve(100000); //preallocate memory, makes push_back
very efficient until you exceed the allocated memory
		data1.reserve(100000);
		data2.reserve(100000);
	}
}



float SaturableGainNielsenMaterialPlugin::calculateE( int i, float U, float V, float
E,
float &N1,   //storage[0]
float &N2,   //storage[1]
float &N2_n,  //storage[2]
float &dN,   //storage[3]
float &E_n,   //storage[4]
float &P,    //storage[5]
float &P_n,  //storage[6]
float &P_n1,  //storage[7]
float &firstUpdateDone, //storage[8]
float &N3,   //storage[9]
float &N3_n  //storage[10]
                                        )
{
   float dt2 = dt*dt;
   float w02 = w0*w0;

	N3_n=N3;
	N3 = 1.f/(1.f/dt+a32/2.f)*(r3[i]+N3*(1.f/dt-a32/2.f)); //population of pump
level

	N2_n=N2;
	N2 = 1.f/(1.f/dt+a21/2.f+a20[i]/2.f)*(r2[i]+N2*(1.f/dt-a21/2.f-
a20[i]/2.f)+(N3+N3_n)*a32/2.f+Ip[i]*(E+E_n)*(P-P_n)/(4.f*pi*h*w0*dt));
//population of upper laser level

	if (firstUpdateDone == 0.) //system starts at full inversion
		N2 = N2max[i];
		N3 = N2max[i];


	N1 = 1.f/(1.f/dt+a10/2.f)*(r1[i]+N1*(1.f/dt-a10/2.f)+(N2+N2_n)*a21/2.f-
Ip[i]*(E+E_n)*(P-P_n)/(4.f*pi*h*w0*dt)); //population of lower laser level
```

```
        dN = N2-g*N1; //population inversion

        if(saveData) data.push_back(dN);
        if(saveData) data1.push_back(N2);
        if(saveData) data2.push_back(N1);

        firstUpdateDone = 1.;

        P_n1 = P_n;
         P_n = P;

        P=2.f*dt2/(2.f+del_w*dt)*1e30*(P_n*(2.f/dt2-
w02)/1e30+P_n1*(del_w/2.f/dt-1/dt2)/1e30-
6.f/1e30*pi*e0*(pow(c,3))*a21/w02*dN/er[i]*E); //nonlinear polarization to
account for system gain

        E_n=E;

   return (V-P/e0)/(U+(er[i]-1)); //calcluates E from D=epsilon*E+P where
V=D/e0 and U=Lumerial's background perimittivity for the material (plugin
assumes this is set to 1)

}


float SaturableGainNielsenMaterialPlugin::calculateEx( float U, float V, float Ex,
float* storage )
{
   return calculateE(0, U, V, Ex,
storage[0],storage[1],storage[2],storage[3],storage[4],storage[5],storage[6],storag
e[7],storage[8],storage[9],storage[10]);
}

float SaturableGainNielsenMaterialPlugin::calculateEy( float U, float V, float Ey,
float* storage )
{
   return calculateE(1, U, V, Ey,
storage[0],storage[1],storage[2],storage[3],storage[4],storage[5],storage[6],storag
e[7],storage[8],storage[9],storage[10]);
}

float SaturableGainNielsenMaterialPlugin::calculateEz( float U, float V, float Ez,
float* storage )
{
```

```
   return calculateE(2, U, V, Ez,
storage[0],storage[1],storage[2],storage[3],storage[4],storage[5],storage[6],storag
e[7],storage[8],storage[9],storage[10]);
}

SaturableGainNielsenMaterialPlugin::SaturableGainNielsenMaterialPlugin() :
saveData(false), data()
{

}

SaturableGainNielsenMaterialPlugin::~SaturableGainNielsenMaterialPlugin() //
This section allows one to look at the laser level populations if save data is turned
on. Can also be used to examine other plugin variables.
{
   if(saveData){
      ofstream of;
      of.open("dN.txt");
      if(of.is_open()){
         for(vector<float>::iterator i = data.begin(); i!=data.end(); i++)
            of << *i << endl;
      }
      of.close();

                  ofstream of1;
      of1.open("N2.txt");
      if(of1.is_open()){
         for(vector<float>::iterator i = data1.begin(); i!=data1.end(); i++)
            of1 << *i << endl;
      }
      of1.close();

                  ofstream of2;
      of2.open("N1.txt");
      if(of2.is_open()){
         for(vector<float>::iterator i = data2.begin(); i!=data2.end(); i++)
            of2 << *i << endl;
      }
      of2.close();
   }
}

extern "C" DLLEXPORT IMaterialPlugin* createInstance()
{
   return new SaturableGainNielsenMaterialPlugin();
}
```

2. *SiTPA*

immaterialplugin.h

```
#ifndef _IMATERIALPLUGIN_H
#define _IMATERIALPLUGIN_H

#include <stddef.h>

/*!
   \brief The interface class definition for a material plugin for FDTD Solutions

   This pure abstract class defines the methods that must be implemented to create
a plugin material in FDTD Solutions. A class that inherits from this interface class
and implements all the methods can be compiled into a dynamic library that can
be loaded into FDTD Solutions to define new materials.
*/

class IMaterialPlugin
{
public:
   virtual ~IMaterialPlugin(){};
   virtual const char* name() const = 0;
   virtual const char* uniqueId() const = 0;
   virtual const char** parameterNames() const = 0;
   virtual float calculateEx( float U, float V, float Ex, float* storage) = 0;
   virtual float calculateEy( float U, float V, float Ey, float* storage) = 0;
   virtual float calculateEz( float U, float V, float Ez, float* storage) = 0;
   virtual void initialize(const double** parameters, double dt) = 0;
   virtual void initializeStorageEx(float* storage) = 0;
   virtual void initializeStorageEy(float* storage) = 0;
   virtual void initializeStorageEz(float* storage) = 0;
   virtual size_t storageSizeE() const = 0;
};

/*!
   \brief The interface class for a magnetic material plugin

   This extends the material plugin defined above with a few more methods that
need to be
   defined for a magnetic material
*/
class IMagneticMaterialPlugin : public IMaterialPlugin
{
public:
   virtual float calculateHx( float U, float V, float Ex, float* storage) = 0;
```

```
   virtual float calculateHy( float U, float V, float Ey, float* storage) = 0;
   virtual float calculateHz( float U, float V, float Ez, float* storage) = 0;
   virtual void initializeStorageHx(float* storage) = 0;
   virtual void initializeStorageHy(float* storage) = 0;
   virtual void initializeStorageHz(float* storage) = 0;
   virtual size_t storageSizeH() const = 0;
};

/*!
   \brief The interface for a factory class that creates and destroys material plugins
*/
class IMaterialPluginFactory{
public:
   virtual IMaterialPlugin* createInstance()=0;
   virtual void destroyInstance(IMaterialPlugin* i)=0;
   virtual IMagneticMaterialPlugin* toMagneticMaterialPlugin(IMaterialPlugin*
p)=0;
};

/*!
   \brief A templated implementation of the IMaterialPluginFactory class

   Plugin authors do not need to write a factory class, they can just use this class.
It is written
   as a template so that it can be compiled into the plugin easily. This is done in
the plugin code
   usign the MATERIAL_PLUGIN(T) macro.
*/
template<class T>
class MaterialPluginFactory : public IMaterialPluginFactory
{
   IMaterialPlugin* createInstance(){return new T();}
   void destroyInstance(IMaterialPlugin* i){delete i;}
   IMagneticMaterialPlugin* toMagneticMaterialPlugin(IMaterialPlugin*
p){return dynamic_cast<IMagneticMaterialPlugin*>(p);}
};

#ifdef WIN32
#define DLLEXPORT __declspec(dllexport)
#else
#define DLLEXPORT
#endif

//A macro to add the factory function to the plugin, instantiating the
MaterialPluginFactory in the process
```

```
//All plugins should include this macro once in a source file. The argument T is
the name of the user's plugin class
#define MATERIAL_PLUGIN(T) \
   extern "C" DLLEXPORT IMaterialPluginFactory* createFactoryV1(){ return
new MaterialPluginFactory<T>();} \
   extern "C" DLLEXPORT void destroyFactoryV1(IMaterialPluginFactory* f){
delete f;}

#endif
```

SiTPA.h

```
#ifndef _SITPA_H
#define _SITPA_H

#include "imaterialplugin.h"

class SiTPAPlugin : public IMaterialPlugin
{
public:
   SiTPAPlugin(){};
   virtual ~SiTPAPlugin(){};

   const char* name() const {return "SiTPA";};
   const char* uniqueId() const {return "{CFE9991C-6837-46a2-BBB4-
E9EABD833DFC}";};
   const char** parameterNames() const {return names;};
   float calculateEx( float U, float V, float Ex, float* storage);
   float calculateEy( float U, float V, float Ey, float* storage);
   float calculateEz( float U, float V, float Ez, float* storage);
   void initialize(const double** parameters, double dt);
   void initializeStorageEx(float* storage){};
   void initializeStorageEy(float* storage){};
   void initializeStorageEz(float* storage){};
   size_t storageSizeE() const {return 5;}; //# of additional storage fields

private:
   float calculate(int axis, float U, float V, float E, float* storage);
         void initializeStorageE(int axis, float* storage);

         static const double hbar;
   static const double eps0;
         static const double tau;
         static const double betaTPA;
         static const double n0;
         static const double exp;
```

```
        static const double c;
        static const double pi;
        static const double Nfi;

        double Ip[3];
        double N_initial[3];
        double lambda0[3];
        double Nf[3];
        double g1;
        double g2;
        double n_plasma;
        double n_plasma_n;
        double d_t;
        float n;
        float lambda_n[3];

   static const char* names[4];
};

#endif
```

SiTPA.cpp

```
#include "SiTPA.h"
#include <cmath>

/*!
   \class NSiTPAPlugin
        For studying TPA and free carrier effects in Si in the telecom wavelengths around 1.55um.
        Based on the FDTD formulism for TPA and free carrier effects from [1].
        Does not take into account linear absorption and dispersive refractive index (assumes you use Si as the base material in Lumerical), and does not currently have Kerr or Raman effects (since these
        occur on a different scale than TPA and free carrier effects). All units are standard SI.

        [1] N. Suzuki, "FD-TD Analysis of Two-Photon Absorption and Free Carrier Absorption in Si High-Index-Contrast Waveguides," Journal of Lightwave Technology 25, 2495 (2007).

*/

const double SiTPAPlugin::hbar = 1.05457148e-34; // [J/s]
const double SiTPAPlugin::exp = 0.8; //constant
const double SiTPAPlugin::eps0 = 8.854187817e-12; //vacuum permitivity [F/m]
```

```
const double SiTPAPlugin::c = 2.99792458e8; //speed of light [m/s]
const double SiTPAPlugin::tau = 1e-12; //free carrier recombination time in
oxygen doped silicon[s]
const double SiTPAPlugin::n0 = 3.48; //refractive index of Si at 1.55um
const double SiTPAPlugin::betaTPA = 0.9e-11; // [m/W]
const double SiTPAPlugin::pi = 3.1415926535897931;
const double SiTPAPlugin::Nfi = 1.01e16; //[m^-3] intrinsic free carrier density
of Si


const char* SiTPAPlugin::names[4] = {"Peak Intensity of Input Pulse [W/m^2]",
"Center Wavelength of Input Pulse [m]","Initial Free Carrier Concentration [m^-
3]", 0};


void SiTPAPlugin::initialize(const double** parameters, double dt)
{
        d_t=dt;
   for(int i=0; i<3; i++){
                Ip[i] = double(parameters[0][i]);
                lambda0[i] = float(parameters[1][i]);
                N_initial[i] = double(parameters[2][i]);
                lambda_n[i]=lambda0[i]/1.55e-6;
   }
}



float SiTPAPlugin::calculate(int i, float U, float V, float Et, float* storage)
{
        double Nf = storage[0];
        double n_plasma_n = storage[1];
        double Vn = storage[2];
        double Un = storage[3];
        double En = double(Et);
        double E = double(Et);
        float firstUpdateDone = storage[4];


        n=1.;

        Nf = (2.*tau-
d_t)/(2.*tau+d_t)*Nf+tau*d_t/(2.*tau+d_t)*lambda0[i]/2./pi/c/hbar*betaTPA*Ip[i
]*Ip[i]*abs(En*En*En*En); //free carrier concentration
        if (firstUpdateDone == 0.) //initial free carrier concentration
                Nf = N_initial[i];
```

```
        if (Nf<Nfi) //free carrier concentration cannot drop below intrinsic value
for silicon
                Nf=Nfi;

        firstUpdateDone = 1.;
        n_plasma=-8.8e-28*Nf-8.5e-
24*(pow(Nf,exp))*lambda_n[i]*lambda_n[i]; //change in refractive index due to
plasma dispersion


        //loop for iterating E field and effect of chi_TPA and chi_FCA. 6
iterations was determiend to be sufficient for convergence
        while (n<6){
                g1=2*n0*n_plasma+c*n0*(1.45e-
21*lambda_n[i]*lambda_n[i]*Nf)*d_t/2+c*c*eps0*n0*n0*betaTPA*d_t*(E*E+
En*En)*Ip[i]/8;
                g2=2*n0*n_plasma_n-c*n0*(1.45e-
21*lambda_n[i]*lambda_n[i]*Nf)*d_t/2-
c*c*eps0*n0*n0*betaTPA*d_t*(E*E+En*En)*Ip[i]/8;
                E=1/(g1+U)*(g2*En+(V-Vn)+Un*En);
                n=n+1;
        }


        //update storage
        storage[0] = Nf;
        storage[1] = n_plasma;
        storage[2] = V;
        storage[3] = U;
        storage[4] = float(firstUpdateDone);

   return E;

}



float SiTPAPlugin::calculateEx( float U, float V, float Ex, float* storage )
{
   return calculate(0, U, V, Ex, storage);
}

float SiTPAPlugin::calculateEy( float U, float V, float Ey, float* storage )
{
   return calculate(1, U, V, Ey, storage);
}
```

```
float SiTPAPlugin::calculateEz( float U, float V, float Ez, float* storage )
{
   return calculate(2, U, V, Ez, storage);
}


MATERIAL_PLUGIN(SiTPAPlugin);
```

Appendices References

[1] K. S. Yee, “Numerical Solution of Initial Boundary Value Problems Involving Maxwell’s Equations in Isotropic Media,” IEEE T. Atenn, Propag. **14**, 302-3077 (1966).

[2] A. Taflove and S. C. Hagness, *Computational Electrodynamics: The Finite-Difference Time-Domain Method,* 3rd ed. (Artech House, Norwood, 2005).